SCANNING HALL PROBE MICROSCOPY OF MAGNETIC VORTICES IN VERY UNDERDOPED YTTRIUM-BARIUM-COPPER-OXIDE

A DISSERTATION
SUBMITTED TO THE DEPARTMENT OF PHYSICS
AND THE COMMITTEE ON GRADUATE STUDIES
OF STANFORD UNIVERSITY
IN PARTIAL FULFILLMENT OF THE REQUIREMENTS
FOR THE DEGREE OF
DOCTOR OF PHILOSOPHY

Janice Wynn Guikema
March 2004

I certify that I have read this dissertation and that, in my opinion, it is fully adequate in scope and quality as a dissertation for the degree of Doctor of Philosophy.

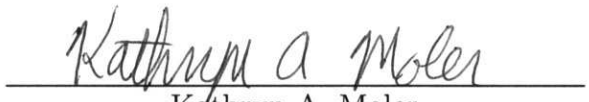

Kathryn A. Moler
(Principal Advisor)

I certify that I have read this dissertation and that, in my opinion, it is fully adequate in scope and quality as a dissertation for the degree of Doctor of Philosophy.

Malcolm R. Beasley

I certify that I have read this dissertation and that, in my opinion, it is fully adequate in scope and quality as a dissertation for the degree of Doctor of Philosophy.

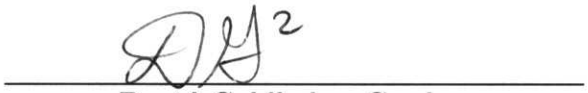

David Goldhaber-Gordon

Approved for the University Committee on Graduate Studies.

Abstract

Since their discovery by Bednorz and Müller (1986), high-temperature cuprate superconductors have been the subject of intense experimental research and theoretical work. Despite this large-scale effort, agreement on the mechanism of high-T_c has not been reached. Many theories make their strongest predictions for underdoped superconductors with very low superfluid density n_s/m^*. For this dissertation I implemented a scanning Hall probe microscope and used it to study magnetic vortices in newly available single crystals of very underdoped $YBa_2Cu_3O_{6+x}$ (Liang et al. 1998, 2002). These studies have disproved a promising theory of spin-charge separation, measured the apparent vortex size (an upper bound on the penetration depth λ_{ab}), and revealed an intriguing phenomenon of "split" vortices.

Scanning Hall probe microscopy is a non-invasive and direct method for magnetic field imaging. It is one of the few techniques capable of submicron spatial resolution coupled with sub-Φ_0 (flux quantum) sensitivity, and it operates over a wide temperature range. Chapter 2 introduces the variable temperature scanning microscope and discusses the scanning Hall probe set-up and scanner characterizations. Chapter 3 details my fabrication of submicron GaAs/AlGaAs Hall probes and discusses noise studies for a range of probe sizes, which suggest that sub-100 nm probes could be made without compromising flux sensitivity.

The subsequent chapters detail scanning Hall probe (and SQUID) microscopy studies of very underdoped $YBa_2Cu_3O_{6+x}$ crystals with $T_c \leq 15$ K. Chapter 4 describes two experimental tests for *visons*, essential excitations of a spin-charge separation theory proposed by Senthil and Fisher (2000, 2001b). We searched for predicted hc/e vortices (Wynn et al. 2001) and a vortex memory effect (Bonn et al. 2001) with

null results, placing upper bounds on the vison energy inconsistent with the theory. Chapter 5 discusses imaging of isolated vortices as a function of T_c. Vortex images were fit with theoretical magnetic field profiles in order to extract the apparent vortex size. The data for the lowest T_c's (5 and 6.5 K) show some inhomogeneity and suggest that λ_{ab} might be larger than predicted by the $T_c \propto n_s(0)/m^*$ relation first suggested by results of Uemura et al. (1989) for underdoped cuprates. Finally, Chapter 6 examines observations of apparent "partial vortices" in the crystals. My studies of these features indicate that they are likely split pancake vortex stacks. Qualitatively, these split stacks reveal information about pinning and anisotropy in the samples. Collectively these magnetic imaging studies deepen our knowledge of cuprate superconductivity, especially in the important regime of low superfluid density.

Acknowledgements

First and foremost I want to thank my advisor Kathryn (Kam) Moler. It has been an honor to be her first Ph.D. student. She has taught me, both consciously and unconsciously, how good experimental physics is done. I appreciate all her contributions of time, ideas, and funding to make my Ph.D. experience productive and stimulating. The joy and enthusiasm she has for her research was contagious and motivational for me, even during tough times in the Ph.D. pursuit. I am also thankful for the excellent example she has provided as a successful woman physicist and professor.

The members of the Moler group have contributed immensely to my personal and professional time at Stanford. The group has been a source of friendships as well as good advice and collaboration. I am especially grateful for the fun group of original Moler group members who stuck it out in grad school with me: Brian Gardner, Per Björnsson, and Eric Straver. I would like to acknowledge honorary group member Doug Bonn who was here on sabbatical a couple years ago. We worked together (along with Brian) on the spin-charge separation experiments, and I very much appreciated his enthusiasm, intensity, willingness to do frequent helium transfers, and amazing ability to cleave and manipulate $\sim$50 nm crystals. Other past and present group members that I have had the pleasure to work with or alongside of are grad students Hendrik Bluhm, Clifford Hicks, Yu-Ju Lin, Zhifeng Deng and Rafael Dinner; postdocs Mark Topinka and Jenny Hoffman; and the numerous summer and rotation students who have come through the lab.

In regards to the Hall probes, I thank David Kisker (formerly at IBM), and Hadas Shtrikman at Weizmann, for growing the GaAs/AlGaAs 2DEG wafers on which the probes were made. The Marcus group gave me advice on GaAs processes early on.

Yu-Ju shared with me some tips she picked up during her Hall probe fab, and Cliff spent a summer at Weizmann fabricating our 3rd generation Hall probes. David Goldhaber-Gordon and Mark shared some of their expert 2DEG knowledge with me. For the noise studies, Mark wrote a spectrum analyzer program and Per, Brian, and Rafael took some of the noise measurements. I would also like to acknowledge the Stanford Nanofabrication Facility and the student microfabrication lab in Ginzton, where I made the probes, and Tom Carver who did the metal evaporations.

The vortex studies discussed in this dissertation would not have been possible without the high-purity crystals of underdoped $YBa_2Cu_3O_{6+x}$ from the group of Doug Bonn and Walter Hardy at the University of British Columbia. I have appreciated their collaboration and the impressive crystal growing skills of Ruixing Liang who grew these crystals.

For the spin-charge separation tests, Doug and Brian made significant contributions to the experiments, with Doug leading the way on the vortex memory experiment. I also thank Matthew Fisher, Senthil Todadri, Subir Sachdev, Steve Kivelson, Patrick Lee, Bob Laughlin and Phil Anderson for inspirational discussions with us regarding these experiments.

In my later work of vortex fitting and studying partial vortices, I am particularly indebted to Hendrik. He wrote the initial code to numerically generate the model of the vortex magnetic field and set up the framework for fitting the model to Hall probe images. Hendrik also performed relevant Monte Carlo simulations of thermal motion of pancake vortices and worked out the equations describing the field profiles of split pancake vortex stacks.

In my attempted measurements of the penetration depth from vortex images, I thank the following people for helpful discussions with us: Steve Kivelson, John Kirtley, Eli Zeldov, Aharon Kapitulnik, and Doug Bonn. For the partial vortex work, I am especially grateful for conversations with Vladimir Kogan and also David Santiago as we strived to determine the cause of the apparent partial vortices.

For this dissertation I would like to thank my reading committee members: Kam, Mac Beasley, and David Goldhaber-Gordon for their time, interest, and helpful comments. I would also like to thank the other two members of my oral defense committee,

Shoucheng Zhang and Mark Brongersma, for their time and insightful questions.

I have appreciated the camaraderie and local expertise of the Goldhaber-Gordon and KGB groups in the basement of McCullough, as well as the Marcus group early on. I am grateful to our group's administrative assistant Judy Clark who kept us organized and was always ready to help.

I gratefully acknowledge the funding sources that made my Ph.D. work possible. I was funded by the U.S. Department of Defense NDSEG fellowship for my first 3 years and was honored to be a Gabilan Stanford Graduate Fellow for years 4 & 5. My work was also supported by the National Science Foundation and the U.S. Department of Energy.

My time at Stanford was made enjoyable in large part due to the many friends and groups that became a part of my life. I am grateful for time spent with roommates and friends, for my backpacking buddies and our memorable trips into the mountains, for Dick and Mary Anne Bube's hospitality as I finished up my degree, and for many other people and memories. My time at Stanford was also enriched by the graduate InterVarsity group, Menlo Park Presbyterian Church, Palo Alto Christian Reformed Church, and the Stanford Cycling Team.

Lastly, I would like to thank my family for all their love and encouragement. For my parents who raised me with a love of science and supported me in all my pursuits. For the presence of my brother Dave here at Stanford for two of my years here. And most of all for my loving, supportive, encouraging, and patient husband Seth whose faithful support during the final stages of this Ph.D. is so appreciated. Thank you.

Janice Wynn Guikema
Stanford University
March 2004

Contents

List of Tables

List of Figures

Chapter 1

Introduction

The work for this dissertation is two-fold. First, I have implemented a scanning Hall probe microscope (SHPM) for which I fabricated and characterized submicron scanning Hall probe sensors. The SHPM can image magnetic fields with milli-Gauss field sensitivity and spatial resolution as good as 1/2 micron. I have also used Superconducting QUantum Interference Device (SQUID) sensors as the scanning probe. For the second part of the dissertation, I used this microscope to study very underdoped cuprate superconductors by means of flux imaging.

The mechanism of high-temperature superconductivity remains elusive after 18 years of intense study. The temperature versus doping phase diagram of the high-T_c cuprates exhibits numerous phases, which are shown in Figure 1.1. Theories of cuprate superconductivity make some of their strongest predictions for the very underdoped region where the superfluid density is low, the sample is deep in the pseudogap in its "normal" state, and the doping level is close to the antiferromagnetic insulating phase. For this reason it is important to study very underdoped cuprates to help illuminate the mechanism of the superconductivity.

Our scanning magnetic microscopy studies of the very underdoped cuprate superconductor $YBa_2Cu_3O_{6+x}$ (YBCO), with $x \sim 6.35$, have refuted a promising theory of spin-charge separation (Wynn et al. 2001; Bonn et al. 2001), given information about vortex pinning forces (Gardner et al. 2002), enabled measurements of the in-plane penetration depth, and revealed surprising "partial vortices" in the lowest T_c samples. High quality very underdoped YBCO crystals were crucial to these studies

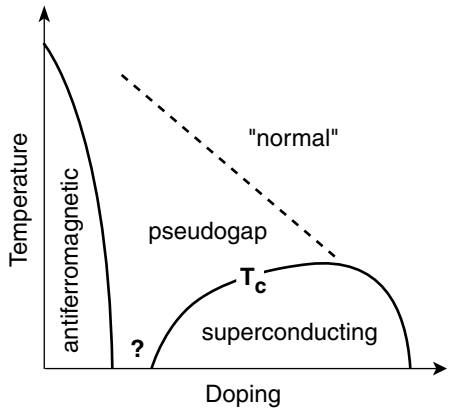

Figure 1.1: Schematic phase diagram for cuprate superconductors. The pseudogap phase is not superconducting, yet exhibits some characteristics of superconductivity. The question mark indicates a poorly understood region.

and are a result of recent improvements in crystal growth (Liang et al. 1998, 2002) by Ruixing Liang, Walter Hardy, and Doug Bonn at the University of British Columbia.

This chapter introduces the tools and concepts for scanning magnetic microscopy, gives an introduction to vortex imaging and the very underdoped YBCO studies, and finally overviews the preparation of the YBCO crystals.

1.1 Scanning magnetic microscopy

In this section I discuss and compare the three types of scanning magnetic sensors employed in the Moler Lab. Then I introduce basic concepts of the scanning microscopy and discuss the desire for good spatial resolution.

1.1.1 Mesoscopic magnetic sensors

Scanning magnetic microscopy permits studies of a wide range of magnetic materials and magnetic phenomena. Bending (1999) gives a thorough overview of magnetic imaging techniques for superconductors. In the Moler Lab we have focused on the

Table 1.1: Comparison of mesoscopic magnetic sensors in the Moler Lab.

sensor:	MFM	SQUID	Hall probe
measurement:	F or ∇F	Φ	B_z
sensitivity:	1 μN/m	few $\mu\text{G}/\sqrt{\text{Hz}}$	1–100 $\text{mG}/\sqrt{\text{Hz}}$
	(100 Hz BW)	$\leq 1\ \mu\Phi_0/\sqrt{\text{Hz}}$	16 $\mu\Phi_0/\sqrt{\text{Hz}}$ (>1 kHz)
			1 $\text{m}\Phi_0/\sqrt{\text{Hz}}$ (0.1 Hz)
spatial resolution:	30–50 nm†	4 μm	0.5 μm
resolution goal:	10 nm	0.5 μm	100 nm
field range:	broad	< 100 G	broad
temperature range:	broad	< 10 K	broad

†From the literature.

techniques of three sensors and applied them mainly to the study of superconductors: magnetic force microscopy (MFM), superconducting quantum interference device (SQUID) magnetometry and susceptometry, and Hall probe microscopy. These sensors are capable of submicron or micron spatial resolution and are highly sensitive magnetic field or flux detectors, easily measuring with sub-Φ_0 sensitivity, where Φ_0 is the superconducting flux quantum $hc/2e$. Unlike other techniques, imaging with these sensors does not require special sample preparation, making them applicable tools for studying many samples. Each type of sensor has unique advantages and disadvantages. Table 1.1 lists the main properties of our sensors, which will be discussed in turn below.

MFM measures the force or force gradient between a magnetic tip of magnetization $\mathbf{M}$ and the sample magnetic field $\mathbf{B}$, where $\mathbf{F} = \int_{\text{tip}} \nabla(\mathbf{M} \cdot \mathbf{B}) dV$. Thus it is not straightforward to directly obtain the magnetic field from an MFM image, since the field is convolved with $\mathbf{M}$, which is difficult to characterize. For the same reason, flux sensitivity of MFM is hard to quantify but is generally not as good as for SQUIDs and Hall probes. An advantage of MFM is the ability to achieve high spatial resolution. To my knowledge the best demonstrated MFM spatial resolution to date is 30–42 nm (Skidmore and Dahlberg 1997; Phillips et al. 2002; Champagne et al. 2003).

Another issue with MFM is that the magnetic tip exerts a force on the sample,

potentially disrupting the features of interest. Hug et al. (1994) were the first to observe individual vortices with an MFM and saw that the tip perturbed the vortices. While this tip force is generally a disadvantage, it could be used to study vortex pinning forces in superconductors. Eric Straver has built and is using a low temperature MFM in the Moler Lab. MFM can operate over broad temperature and field ranges.

SQUIDs are currently the most sensitive magnetic flux detectors. Scanning SQUIDs measure the magnetic flux through a small pick-up loop, $\Phi = \int_{\text{loop}} \mathbf{B} \cdot d\mathbf{a}$, with sensitivity down to $\sim$1 $\mu\Phi_0/\sqrt{\text{Hz}}$. Our SQUIDs are specially designed with an additional loop concentric with the pick-up loop which allows a local field to be applied to the sample. This allows the SQUID to also operate as a scanning susceptometer by measuring the response of a sample to a locally applied field (Gardner et al. 2001). Limitations of SQUIDs are in their spatial resolution, field range, and operating temperature. The linewidth of the superconducting wires is the limiting factor for the SQUID pick-up loop size, since the wire width cannot be smaller than the penetration depth of the superconducting material. Our smallest scanning SQUIDs were designed and fabricated by Martin Huber (CU-Denver) with 4 μm diameter pick-up loops. The SQUIDs used in this dissertation had 8 μm square pick-up loops and were made by the commercial foundry HYPRES.[1] SQUIDs operate at low fields and low temperatures (<9 K for Nb).

Scanning SQUIDs have been developed and implemented by a number of groups, for example Dale van Harlingen at Illinois, John Kirtley at IBM, John Clarke at UC Berkeley, Fred Wellstood at Maryland, and our group at Stanford. The summary article by Kirtley (2002) gives an overview of advances in and recent uses of mesoscopic scanning SQUIDs. The best flux sensitivity reported for scanning SQUIDs is slightly above 10^{-6} $\Phi_0/\sqrt{\text{Hz}}$ for Nb SQUIDs with 4–10 μm pick-up loops (Vu et al. 1993; Kirtley et al. 1995b; Gardner et al. 2001). High-T_c SQUIDs are also used in scanning, but their sensitivity is about an order of magnitude worse than for low-T_c SQUIDs with equivalent spatial resolution (Wellstood et al. 1997). The smallest SQUIDs reported to date were fabricated by Hasselbach et al. (2000) from Al and Nb with 1 μm pick-up loops. The sensitivity limit on these probes was not

[1] http://www.hypres.com/

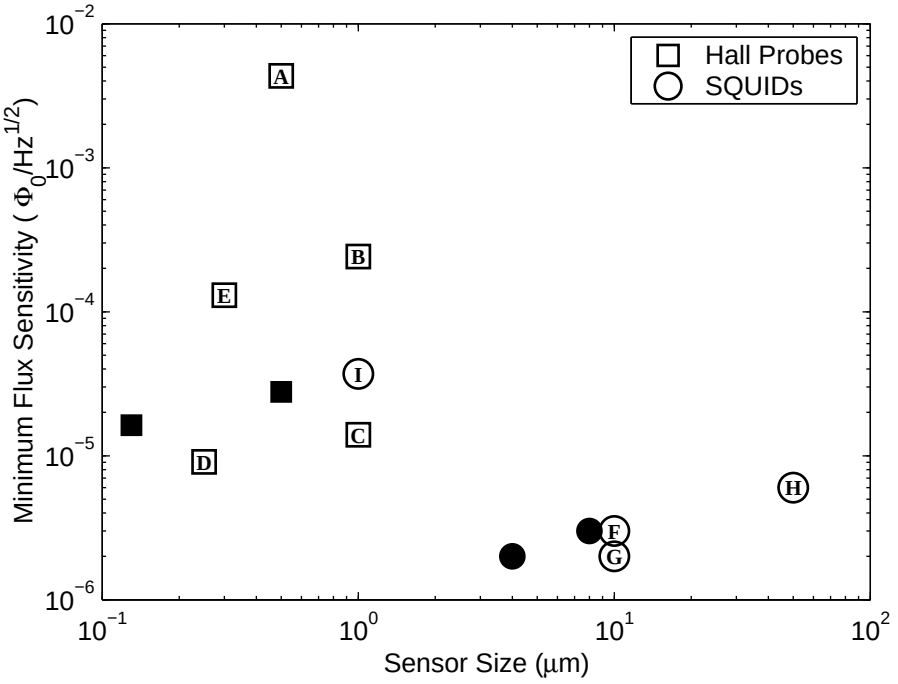

Figure 1.2: Flux sensitivity (white noise floor) versus lithographic sensor size for SQUIDs and Hall probes from the literature (open markers) and the Moler Lab (solid markers). Hall probes: (A) Chang et al. (1992), (B) Davidović et al. (1996), (C) Oral et al. (1996a) [77 K], (D) Oral et al. (1998) [77 K], and (E) Grigorenko et al. (2001) [77 K; GaAs/InAs/GaSb]. SQUIDs: (F) Vu et al. (1993), (G) Kirtley et al. (1995b), (H) Stawiasz et al. (1995), and (I) Hasselbach et al. (2000) [Al]. Unless otherwise noted: $T \leq 5$ K, Hall probes were GaAs/AlGaAs, and SQUIDs were Nb. For Hall probes (D) and (E), effective size was used since lithographic size was not specified.

as good, $3.7 \times 10^{-5}\ \Phi_0/\sqrt{\text{Hz}}$ for Al and higher for Nb, and they also had undesirable hysteresis. Figure 1.2 (circles) shows flux sensitivity versus pick-up loop size for a number of SQUIDs.

Hall probes have the advantage of being direct magnetic field sensors, because the measured Hall voltage is directly proportional to the perpendicular magnetic field averaged over the Hall cross. Figure 1.3 shows a Hall probe response to an applied magnetic field. Hall probes are non-invasive, having self-field of only $\sim$0.4 mG at typical operating currents and sample-probe distances, and they can be made much smaller than SQUIDs. I fabricated and used Hall probes with lithographic size 0.5 μm

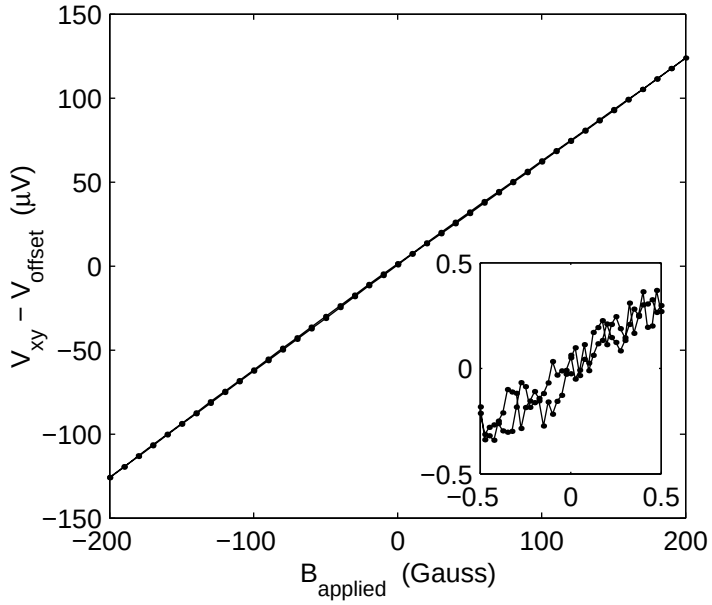

Figure 1.3: Hall probe response to applied field for a 0.5 μm probe. The slope gives the Hall coefficient $R_H = 0.114\ \Omega$/G. The measurement was made at $T = 4.8$ K and $I_{\rm bias} = 5.5\ \mu$A with $f = 1$ kHz using lock-in detection with $\tau = 0.1$ s. Inset: Smaller field sweep giving $B_{\rm noise} \approx 100$ mG.

for scanning, and Clifford Hicks later fabricated probes with lithographic size as small as 130 nm. These probes were made from GaAs/AlGaAs two-dimensional electron gas (2DEG) heterostructures (Section 3.3) which have shown themselves to be the lowest noise materials for low temperature Hall probes. Field sensitivity of our probes at 4 K ranges from 0.1–20 mG/$\sqrt{\rm Hz}$ for $f \geq 10^4$ Hz and from 0.005–1 G/$\sqrt{\rm Hz}$ for 0.1 Hz, for probe sizes of 10 μm down to 130 nm (generally better *field* sensitivity is achieved for larger probes). Our best demonstrated *flux* sensitivity was for the 130 nm probe with 16 $\mu\Phi_0/\sqrt{\rm Hz}$ for >1 kHz and 1 m$\Phi_0/\sqrt{\rm Hz}$ for 0.1 Hz. Hall probes, like MFM, operate over broad field and temperature ranges.

Chang et al. (1992) pioneered high sensitivity submicron SHPM with a Hall probe fabricated from GaAs/AlGaAs. Their probe had lithographic size 0.5 μm (effective geometric size $\sim$0.35 μm due to 2DEG depletion width) and a minimum field noise density of 0.36 G/$\sqrt{\rm Hz}$ at T=4 K. Simon Bending's group later fabricated GaAs/AlGaAs

probes with improved sensitivity: a 1 μm lithographic dimension probe ($\sim$0.85 μm effective size) with noise level 0.3 mG/$\sqrt{\text{Hz}}$ (Oral et al. 1996a) and a 0.25 μm effective size probe with 3 mG/$\sqrt{\text{Hz}}$ noise (Oral et al. 1998) at T=77 K. Other papers including Davidović et al. (1996) and Fukumura et al. (1999) have also reported GaAs/AlGaAs scanning Hall probes. Our 130 nm probe is smaller than any 2DEG probes reported in the literature. Figure 1.2 shows low temperature flux sensitivity versus size for Hall probes and SQUIDs. Hall probes for room temperature use made from Bi films have been reported as small as 120 nm (Chong et al. 2001; Sandhu et al. 2001a), but their much higher noise levels, 7.2 G/$\sqrt{\text{Hz}}$ at room temperature (Sandhu et al. 2001a), make them undesirable for low temperature imaging. GaAs/AlGaAs so far has proven to be the best material for low temperature Hall probes due to very low carrier density and high mobility. Low carrier density gives a high Hall coefficient, and high mobility means low lead resistance, thus minimizing Johnson noise. New materials are being explored for Hall probes such as InAs (Mark Topinka; Gusiatnikov et al. 2001) and InSb (Oral et al. 2002). InAs is a surface 2DEG, and therefore smaller spatial resolution can be more easily attained, but at the cost of decreased sensitivity because the carrier density is higher. InSb is a surface film which at room temperature has better noise characteristics than GaAs/AlGaAs (Oral et al. 2002).

For the scanning microscopy in this dissertation I primarily used Hall probe sensors because of their ease of interpretation, submicron spatial resolution, and unrestricted temperature range. A scanning SQUID was used for part of the spin-charge separation experiments when temperatures below $\sim$7 K were sufficient and absolute flux measurement was the primary desire. Both Hall probes and SQUIDs operate in our ^{4}He variable temperature (1.5–300 K) scanning microscope. This is an Oxford Instruments SXM with OptistatSXM flow cryostat. It has xyz coarse motion and also a specially designed "large area scanner" based on a design by Siegel et al. (1995) capable of 60×60 μm^2 scan areas at 4 K. Details of the microscope and scanning electronics are given in Chapter 2.

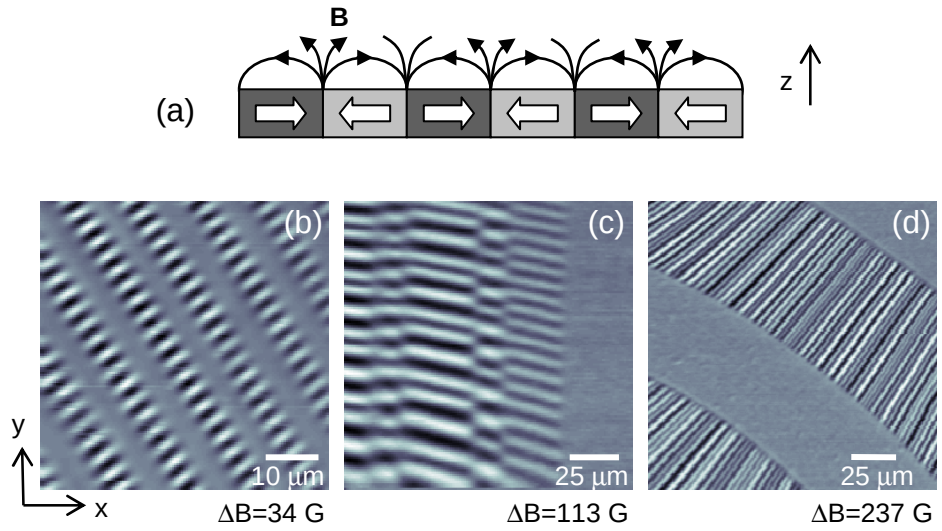

Figure 1.4: Images of magnetic bits taken with a 2 μm Hall probe. (a) Schematic of bit magnetization and resulting field lines. (b) Image of bits spaced 1.69 μm (sample courtesy of Shan Wang) at $T = 4$ K. (c) Image of an old hard disk at room temperature. (d) Image of a floppy disk at room temperature. Hysteresis in the scanner at room temperature caused the tracks to appear curved. (For each image "ΔB" gives the fullscale of the colormap.)

1.1.2 Magnetic imaging and spatial resolution

A magnetic image is obtained by scanning a sensor over the sample of interest and recording the sensor output for a grid of points in the xy-plane. Both Hall probes and SQUIDs are sensitive only to the B-field perpendicular to the sensor (and the sample, since the probe and sample surface are nearly parallel in the microscope). Figure 1.4 shows images of magnetic bits I took with a 2 μm scanning Hall probe. For bits with magnetization in the xy-plane of the sample, the probe detects the B_z at the bit ends, giving bright and dark regions.

Spatial resolution of a probe can be a determining factor in its usability for studying magnetic phenomena. Figure 1.5 shows images of canted antiferromagnetic domains in the manganese oxide $Pr_{0.7}Ca_{0.3}MnO_3$ (sample courtesy of Bernhard Keimer and Diego Casa) that I took with a 2 μm Hall probe. However, the magnetic features in the images appear similar in size to the 2 μm probe and thus it is likely that these images actually show averages of multiple domains over the finite sized Hall

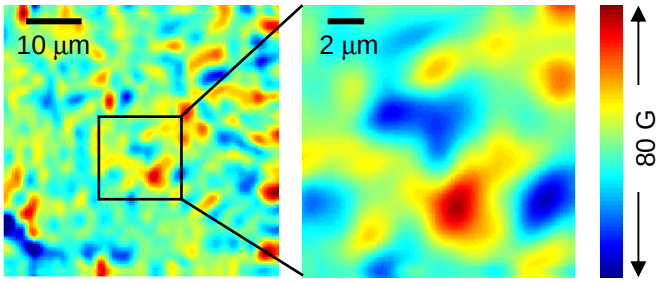

Figure 1.5: Images of canted antiferromagnetic domains in $Pr_{0.7}Ca_{0.3}MnO_3$ taken with a 2 μm Hall probe. The images are spatial resolution limited and the individual domains are not resolved. $T = 10$ K.

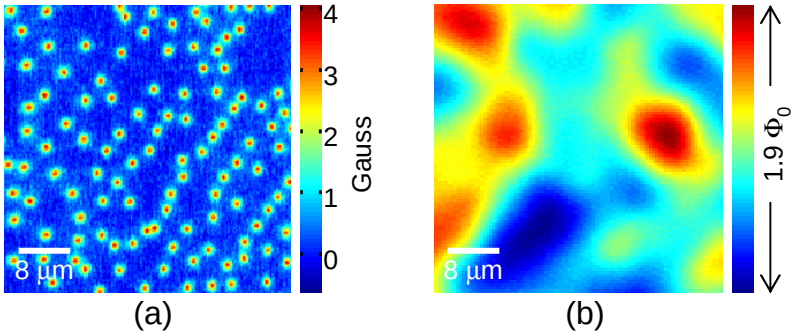

Figure 1.6: Hall probe and SQUID images of many vortices ($T = 4$ K). Both images are 45×45 μm^2. (a) 112 vortices imaged with a 0.5 μm Hall probe in near-optimally doped YBCO. (b) A spatially resolution limited image of approximately 45 vortices in YBCO taken with an 8 μm SQUID.

probe. Better spatial resolution would be required to study these domains. From these images the true size and magnetization of the domains cannot be determined.

Another way to see the importance of spatial resolution is to compare the images in Figure 1.6 of many vortices in a superconductor taken with a 0.5 μm Hall probe and an 8 μm SQUID. In the Hall probe image, the 112 individual vortices in the 45×45 μm^2 area are clearly resolved. The SQUID image of the same size area was taken for a sample field-cooled in $B_{\text{applied}} = 0.46$ G and should contain ~45 vortices. However, this image clearly shows spatial resolution limitations of the scanning SQUID for this vortex density. The SQUID can be a very useful tool for vortex imaging when the

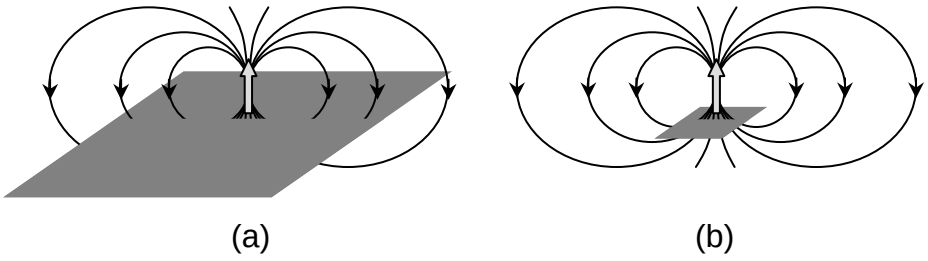

Figure 1.7: Effect of probe size for detection of a magnetic dipole. In (a) most of the flux lines get cancelled out. In (b) the smaller sensor captures more flux making it a more sensitive magnetic dipole detector. (The smaller size is only advantageous when the sample and probe are close together.)

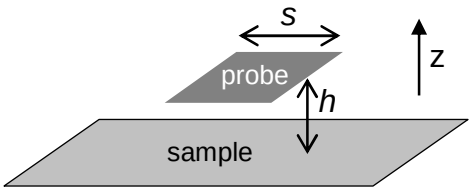

Figure 1.8: Sketch of scanning microscopy. The probe is scanned in the xy-plane at a constant height h above the sample. The xy spatial resolution scales roughly as $\sqrt{s^2 + h^2}$.

vortices are further apart or when total flux is the main interest.

Yet another benefit of smaller probes is in detecting a small magnetic dipole. If a large probe is centered on the dipole as in Figure 1.7(a), most of the flux lines will return within the probe area and escape detection. With a smaller probe, however, much more flux can be captured as shown in Figure 1.7(b). Thus smaller probes make better dipole detectors when the probe is placed close to the dipole. (For larger dipole-probe separations, there would be an optimal size for best sensitivity as a function of separation.)

There are two contributions to the absolute spatial resolution for Hall probes and SQUIDs: the size of the probe s and the height h of the probe above the sample. (See Figure 1.8). The xy spatial resolution scales roughly as $\sqrt{s^2 + h^2}$. Thus to obtain good spatial resolution, not only is it necessary to have a small sensor, but the sensor must also be close to the sample. For the scanning SQUIDs that I have used, $s = 8\ \mu$m

and $h \sim 1.5$ μm, so the probe size was the limiting factor in the spatial resolution. In contrast, for the smallest Hall probes I used for scanning, $s \approx h \approx 0.5$ μm. Future improvements in our Hall probe spatial resolution must reduce both s and h. Note that there is no reason to have a probe with $s \ll h$, since having the smaller s in that limit does not improve the spatial resolution, but would decrease the sensitivity.

A fundamental limit on the Hall probe size and height above the sample is the depth of the 2DEG below the surface of the heterostructure. The depletion width of 2DEG scales roughly with depth, limiting the minimum size of the probe to roughly twice the depth. As for height, a sample cannot be closer to the 2DEG Hall probe than the depth of the 2DEG. My 0.5 μm probes were fabricated on 140 nm deep 2DEG (grown by David Kisker, IBM) and Cliff made his probes on 40 nm 2DEG (grown by Hadas Shtrikman, Weizmann). In the literature, probes have typically been made on ∼100 nm deep 2DEG (Chang et al. 1992; Sandhu et al. 2001b). 2DEG as shallow as 20 nm has successfully been grown (Goldhaber-Gordon et al. 1998), and it could be possible to make Hall probes from a material with a surface 2DEG (e.g. InAs). Thin film metals would obviously not have these depth concerns, but their noise properties do not rival that of 2DEG due to their much higher carrier densities.

The 2DEG depth is the ultimate lower limit on the height of the scanning Hall probe, but alignment also is a factor, and in practice is much larger. The probe is fabricated very close to a tip which touches the sample, with the angle between the sample and probe chip as shallow as ∼1°. Thus the distance from the active area of the Hall probe to the tip, as well as the alignment angle, contribute to the height of the probe. Chang et al. (1992) reported one of the smallest tip-probe distances of 4 μm, giving their probe a minimum total height ∼0.2 μm. The tip-probe distance cannot be arbitrarily small because the Hall probe must have four current/voltage leads coming in at right angles.

In Chapter 3 of this dissertation, I give more details about Hall probes and discuss my fabrication process for the second generation of Hall probes with smallest size 0.5 μm (lithographic). The first generation probes were 2 μm. I also discuss noise studies of one of my 0.5 μm probes and of third generation probes ranging in size from 0.13 μm to 10 μm. The noise studies show that while field sensitivity worsens

as Hall probe size is decreased, flux sensitivity improves. This holds promise that sub-100 nm probes can be fabricated without compromising flux sensitivity.

1.2 Vortex imaging

In this section I will give a brief review of vortices in superconductors, motivation for why we should image them, and finally an introduction to the vortex imaging experiments on very underdoped $YBa_2Cu_3O_{6+x}$ described in Chapters 4–6.

1.2.1 The basics

My main use of the scanning Hall probe (and SQUID) microscope has been to image magnetic vortices in superconductors, primarily in very underdoped YBCO. Hallmarks of superconductivity are zero DC resistance and the expulsion of magnetic field (the Meissner Effect). In type II superconductors, instead of full field expulsion, for a range of fields it is energetically favorable for the magnetic flux to enter the superconductor in bundles, which can also be thought of as vortices of supercurrent around a normal core. This occurs in type II superconductors because λ is larger than ξ, which makes the energy of a superconducting-normal interface negative, and so the superconductor lowers its energy by allowing normal regions (the flux bundles). The penetration depth, λ, is the length scale of magnetic field penetration into a superconductor, while the coherence length, ξ, is the length scale over which the superconducting order parameter can change. The phase of the superconducting order parameter must be single valued and this leads to fluxoid quantization: $\Phi + (m^*c/e^*) \oint \mathbf{v}_s \cdot d\mathbf{s} = n\Phi_0$ (see Tinkham 1996, p. 127), where $\Phi_0 = hc/e^*$ and $e^* = 2e$ for Cooper pairs. For an isolated vortex in a sample large compared to the penetration depth, there is a line integral where $\mathbf{v}_s = 0$, so the vortex flux Φ is quantized. The superfluid energy of a vortex scales as flux squared, and as mentioned above the interface energy of the normal core is negative, so to minimize the free energy the flux is split up into as many vortices as possible each carrying the minimum allowed flux of Φ_0.

The penetration depth and coherence length are key length scales in a superconductor. In terms of vortices, ξ is the size of the vortex core and λ is the extent of the vortex magnetic field. The coherence length is small in the YBCO and cannot be measured with our scanning magnetic probes. On the other hand, the penetration depth affects the field profile of the vortex which is imaged by the scanning probe. (The coherence length also affects the field profile by cutting off the singularity at the vortex center.) λ is related to the superfluid density, n_s/m^*, by the relation $4\pi\lambda^2/c^2 = m^*/n_s e^2$. The penetration depth, if measured experimentally, can give direct information about the superconducting state. For high temperature superconductors whose mechanism has yet to be understood, measurements of the superfluid density are of great theoretical importance.

The field of a vortex inside a superconductor is spread out on the length scale λ. Near the surface of the superconductor the flux spreads out further starting at a depth of approximately λ. The exact field profile inside and outside the superconductor can be solved from London theory. Above the superconductor at distances large compared to λ, the vortex profile resembles that of a magnetic monopole located a distance λ beneath the surface (Pearl 1966). The scanning magnetic microscope images the vortex field profile just above the superconductor surface. Cuprates are anisotropic superconductors and the relevant penetration depth for vortices perpendicular to the planes (c-axis vortices) is the in-plane penetration depth λ_{ab} (Chang et al. 1992; Kogan et al. 1993). See Figure 1.9 for a cartoon of a vortex and Figure 1.10 for Hall probe images of vortices in a near-optimally doped YBCO crystal. Other experiments have measured $\lambda_{ab} \sim 0.16$ μm for $T \to 0$ in optimally doped YBCO (Basov et al. 1995), so these images are resolution-limited.

Scanning Hall probe microscopy of individual vortices and the determination of λ from the images was first demonstrated by Chang et al. (1992) for a superconducting thin film. Oral et al. (1996b) and Davidović et al. (1996) also achieved scanning Hall probe microscopy of single vortices several years later.

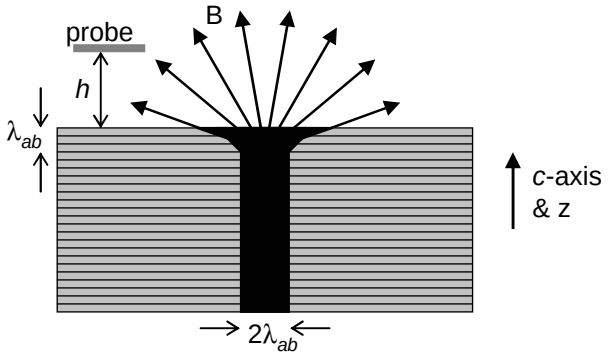

Figure 1.9: Cartoon of a vortex in a layered superconductor as viewed in cross-section from the side. λ_{ab} is the in-plane penetration depth. (The layer spacing is *not* to scale. It is really $\ll \lambda$ in the cuprates.) The probe takes images of the vortex magnetic field by scanning just above the superconductor surface.

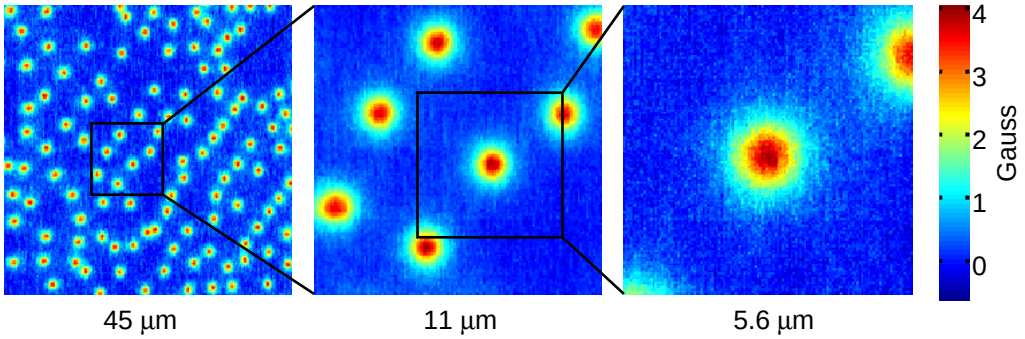

Figure 1.10: Images of vortices in near-optimally doped YBCO ($T_c \sim 90$ K) taken with a 0.5 μm Hall probe at $T = 4$ K.

1.2.2 Experiments in very underdoped YBCO

Single vortex imaging is a powerful tool for studying (type II) superconductivity. This is especially true for unconventional superconductors like the cuprates whose mechanism of superconductivity is yet to be understood. Scanning magnetic microscopy enables measurements of many vortex properties: their total flux, locations, magnetic field profiles (the amount of spreading is determined by λ), homogeneity or inhomogeneity, pinning strength (with MFM and see Gardner et al. (2002)), motion, and potential exotic behavior.

In this dissertation I discuss three groups of experiments on $YBa_2Cu_3O_{6+x}$ done with vortex imaging with a Hall probe and also a SQUID. The first experiment tested for the presence of an additional excitation required by a theory of cuprate superconductivity involving spin-charge separation. In another experiment I imaged individual vortex profiles and from fits attempted to measure the in-plane penetration depth as a function of transition temperature (T_c), though there are caveats to this measurement. Finally, I observed surprising flux features that appeared to be smaller than a flux quantum. Below I introduce each of these experiments in greater detail.

Chapter 4 of this dissertation details our experiments on very underdoped YBCO crystals to test predictions of a spin-charge separation scenario put forth by Senthil and Fisher (2000, 2001a,b). In spin-charge separation superconductivity, the electron (or hole) would fractionalize into a charge-zero spin-$\frac{1}{2}$ fermion and a spin-0 charge-e boson. Spin-charge separation has only been observed in 1D systems, but has been proposed for the quasi-2D cuprate superconductors (Anderson 1987; Kivelson et al. 1987; Nagaosa and Lee 1992). The charge-e bosons would condense directly into a superconducting state without needing to form Cooper pairs as in conventional superconductivity. Spin-charge separation is an appealing theoretical framework for high-T_c because it is simple and also explains some features of the pseudogap observed with angle-resolved photoemission spectroscopy (Senthil and Fisher 1999). Senthil and Fisher's theory predicted an excitation called a *vison* which mediates the binding of the spin and charge, and the vison would have to accompany any $hc/2e$ vortices. Their theory predicted the presence of hc/e vortices ($2\Phi_0$) for low superfluid density and also predicted a vortex memory effect for an underdoped superconducting ring.

Using scanning SQUIDs and Hall probes, we searched for these double vortices and the memory effect in very underdoped YBCO, but did not find either. These experiments (Wynn et al. 2001; Bonn et al. 2001) set a strict upper bound on the energy of the vison incompatible with the theory, thus ruling out as the mechanism of cuprate superconductivity all scenarios of spin-charge separation which require visons.

My next experiment was motivated by vortex images from the spin-charge separation experiments which suggested that the extent of the vortex field was at least 1 μm in very underdoped YBCO. If the vortices are described by London theory, the in-plane penetration depth λ_{ab} is the vortex extent. This inferred $\lambda_{ab} \approx 1$ μm would be larger than predicted by the Uemura relation $T_c \propto n_s(0)/m^*$ for underdoped cuprates. Uemura et al. (1989, 1991) performed muon spin resonance measurements of the penetration depth on many high-T_c samples and other unconventional superconductors. They found a universal linear relationship between the transition temperature and the zero-temperature superfluid density for the underdoped samples. Emery and Kivelson (1995a) explained this linear behavior as thermal phase fluctuations destroying the superconductivity in underdoped samples. For overdoped samples however, pair breaking dominates (as in BCS theory) and T_c is suppressed much below the phase-ordering temperature. This linear relation has been widely accepted as a phenomenological rule, but it has not been tested in extremely underdoped cuprates (with $T_c \lesssim 0.1\,T_{c,\max}$). Due to the theoretical importance of the Uemura relation, it is desirable to test very underdoped samples. Using a submicron scanning Hall probe I imaged many vortices in $YBa_2Cu_3O_{6+x}$ with T_c ranging from 5–15 K, then I fit these images to theoretical vortex field profiles in an attempt to measure λ_{ab}. This work is described in Chapter 5. However, as discussed in Chapter 5, pinning of the 2D pancake vortices which compose the vortex could broaden the apparent spreading of the vortex field, so strictly my results should only be interpreted as an upper bound on λ_{ab}. If pinning is not an issue, the results give larger penetration depths (smaller superfluid density) at the lowest T_c's than predicted by the Uemura relation. If this is the case, theory would need to be modified.

Lastly, some images from the most underdoped YBCO samples revealed distinct flux that appeared to be smaller than Φ_0 vortices. These "partial vortices" typically

appeared in groups and were more mobile than full vortices. I studied these partial vortices and determined that a likely explanation is partial lateral displacements of a full vortex. This can only occur in layered superconductors with large anisotropy where the Josephson coupling between the layers is negligible. In such cases a 3D c-axis vortex can be thought of as a stack of 2D pancake vortices, one in each layer (Clem 1991). Magnetic interactions and any Josephson coupling favor vertical alignment of the pancakes, but with a sufficient pinning landscape a straight stack could have a "split" or "kink" in which a section of the stack is displaced laterally (Benkraouda and Clem 1996; Grigorenko et al. 2002). From above, the field from the partial stacks resembles isolated sub-Φ_0 flux bundles (i.e. partial vortices). My data show split displacements as large as tens-of-microns. My observations of these partial vortices and the model of a split pancake vortex stack are discussed in detail in Chapter 6. This work reveals new vortex behavior which is dominant in the lowest doped YBCO, showing that the material is indeed very anisotropic. The split vortex behavior would be undesirable in technological applications because vortices would be less susceptible to pinning, which would suppress the critical current.

1.3 Very underdoped $YBa_2Cu_3O_{6+x}$ crystals

The vortex imaging experiments described in Chapters 4–6 of this dissertation would not have been possible without the high-purity very underdoped $YBa_2Cu_3O_{6+x}$ single crystals grown by Ruixing Liang in the group of Doug Bonn and Walter Hardy at the University of British Columbia.

Three of the most studied cuprates are $Bi_2Sr_2CaCu_2O_{8+x}$ (BSCCO), $La_{2-x}Sr_xCuO_4$ (LSCO),[2] and $YBa_2Cu_3O_{6+x}$ (YBCO). The value of x in each case tunes the hole doping in the two-dimensional CuO_2 planes where superconductivity occurs. Doping increases with x. Optimal doping (that which gives the maximum T_c) occurs at $x \approx 0.16$ and $T_c \approx 92$ K for BSCCO, $x = 0.16$ and $T_c = 39$ K for

[2]A similar compound to $La_{2-x}Sr_xCuO_4$ is $La_{2-x}Ba_xCuO_4$ which was the first high temperature superconductor discovered (Bednorz and Müller 1986). The Sr and Ba play similar roles, though the Sr compound gives somewhat higher T_c.

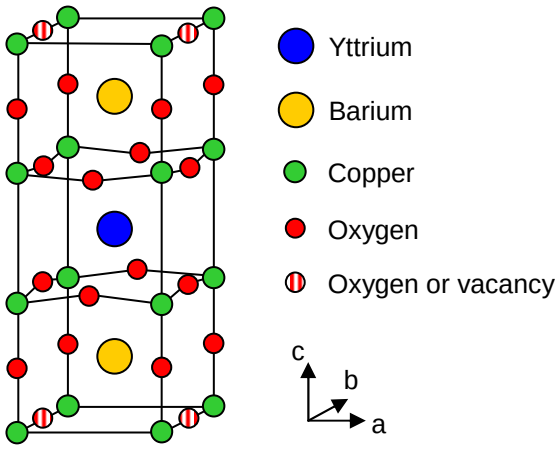

Figure 1.11: $YBa_2Cu_3O_{6+x}$ unit cell. The CuO_2 layers above and below the Y atoms are where the superconductivity occurs. The striped red circles are oxygen sites in the CuO chains. All O sites are full when $x = 1$. The unit cell dimensions are $a = 3.8$ Å, $b = 3.9$ Å, and $c = 11.7$ Å.

LSCO, and $x = 0.91$ and $T_c = 94$ K for YBCO (Liang et al. 1998). The doping of BSCCO increases by adding intercalated oxygen. For LSCO the doping is increased by substituting divalent Sr atoms for trivalent La atoms, while for YBCO the doping is increased by adding oxygen to the CuO chains (Figure 1.11).

It has proven difficult to make high quality very underdoped cuprate superconductors. That is, making highly pure crystalline samples of very low doping that have sharp transition temperatures that are much below the optimally doped T_c. Studies of such samples are crucial to a full understanding of cuprate superconductivity. Underdoped BSCCO is made by annealing after growth to remove oxygen, but neither very low nor sharp underdoped transitions have been obtained. For example, an underdoped BSCCO film grown for an experiment by Kirtley et al. (2003) had a 10–90% resistive transition from 46–79 K (a width $\Delta T_c > 30$ K). Also, when pure BSCCO is made very underdoped it is not structurally stable and tends to flake apart. Very underdoped LSCO is also somewhat difficult to make homogeneous because the Sr atoms that control the doping are not very mobile. In contrast, in YBCO the doping is controlled by higher mobility oxygen atoms in the CuO chains (Figure 1.11), and so a high degree of homogeneity is possible to attain, even at low doping. Liang et al.

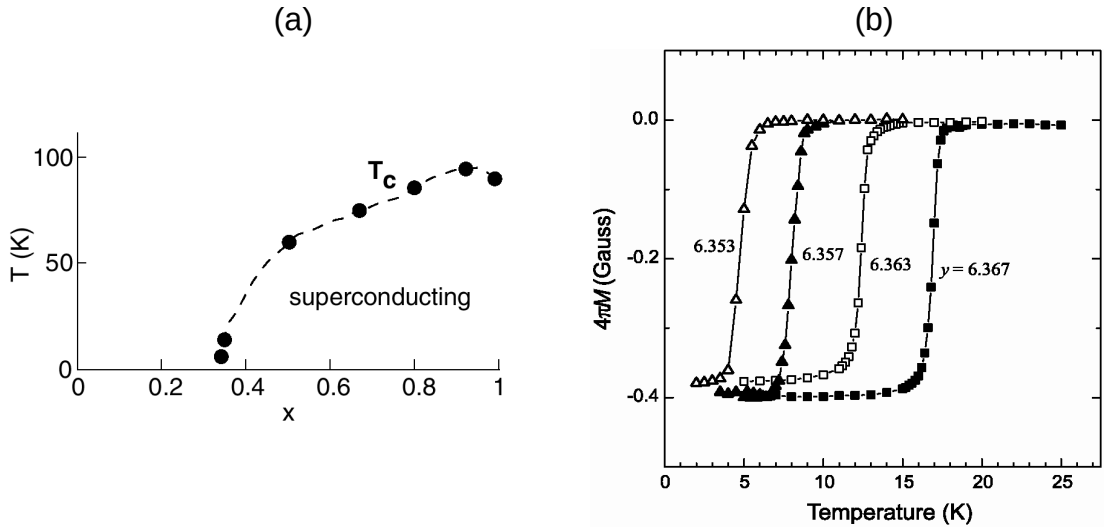

Figure 1.12: T_c values and susceptibility transitions of $YBa_2Cu_3O_{6+x}$ single crystals from UBC. (a) Phase diagram for UBC's single crystals. (b) Susceptibility for the very underdoped samples of $YBa_2Cu_3O_y$ showing sharp transition widths of 1.0–1.6 K measured in a 1 G field (Liang et al. 2002).

(2002) have succeeded in making very underdoped superconducting $YBa_2Cu_3O_{6+x}$ crystals with x as low as 0.345 and T_c's between 4 and 20 K. Figure 1.12(a) shows T_c as a function of oxygen content for the UBC crystals. These crystals have been made with very sharp transition widths <2 K (Figure 1.12(b)).

As described by Liang et al. (1998), growth of highly pure YBCO crystals with near-perfect crystallinity was made possible by homemade $BaZrO_3$ crucibles. The crystals are grown by a self flux method of a Y_2O_3–BaO–CuO melt contained in a crucible. Previously they used commercial YSZ (Y_2O_3 stabilized ZrO_2) crucibles, but reactions with and impurities in those crucibles interfered with crystal growth and limited purity to 99.9%. With the development of the inert $BaZrO_3$ crucibles, YBCO single crystals of high purity (99.995%) and a high degree of crystalline perfection have been grown.

After growth by the self-flux method in the $BaZrO_3$ crucibles, the low oxygen content is set by annealing the crystals together with YBCO ceramic pellets in pure oxygen flow at 900–930°C for a week in a tube furnace. The temperature stability

is 0.5°C and the temperature setting tunes the exact oxygen content between 6.340 and 6.370. After this anneal, oxygen inhomogeneities are removed during a 1–2 week 570°C anneal of the crystals while sealed in a small tube with YBCO ceramic of the same oxygen content. Afterwards the tube is quenched in ice water. (Liang et al. 2002). The crystals are initially twinned and can be several millimeters in the ab-plane with typical thickness 10–100 μm in the c-axis direction.

Initially after quenching, the crystals are not superconducting, but annealing at room temperature allows the chain oxygen atoms to order, increasing the in-plane doping and the T_c until saturation is reached at T_c = 4–20 K depending on the oxygen content. During this low temperature anneal, the chain oxygen atoms form chain fragments in the Ortho-II phase whose increasing lengths provide the carrier doping in the CuO_2 planes. The Ortho-II phase has alternating filled and empty chains and is stable for oxygen content 6.30–6.60. X-ray diffraction studies verified that these very underdoped crystals had only Ortho-II ordering and the ordering correlation lengths were measured to be 1.14(5), 3.6(3), and 1.05(7) nm along the a, b, and c axes respectively in $YBa_2Cu_3O_{6.362}$ crystals. (Liang et al. 2002).

The CuO_2 plane doping and thus T_c dependence on room temperature annealing makes it possible to study a single crystal at many T_c values. For the experiments in Chapters 5 & 6, I studied one such crystal of $YBa_2Cu_3O_{6.375}$ for eight T_c values from 5 to 15 K. Figure 1.13 shows the dependence of T_c on anneal time. The superconducting transitions were measured with the Hall probe in situ in the scanning microscope. The vertical error bars indicate the measured full width of the superconducting transition, limited by the resolution of the measurement technique to ∼10% of the susceptibility. The transition width is nearly 3 K for the lowest $T_c \approx 5$ K, but is sharper than 1.5 K for all the subsequent T_c's. A narrow transition width suggests high homogeneity, and the vortex imaging discussed in Chapter 5 gives further information on the degree of local homogeneity.

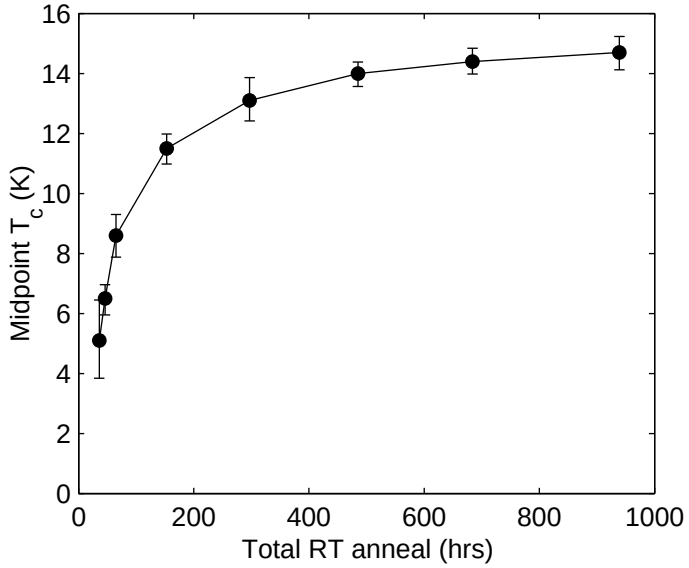

Figure 1.13: T_c versus anneal time for a $YBa_2Cu_3O_{6.375}$ crystal. After growth and high temperature annealing, the T_c of a very underdoped YBCO crystal increases with chain oxygen ordering at room temperature. The transitions were measured by magnetic susceptibility with a Hall probe in an applied quasi-DC (8 mHz) field of 0.20–0.25 G. Vertical bars indicate the resolution-limited full width of the transitions.

Chapter 2

The scanning probe microscope

All the scanning microscopy discussed in this dissertation was done in an Oxford Instruments SXM scanning probe microscope,[1] with extra improvements for scanning Hall probe and scanning SQUID microscopy. This chapter introduces the cryostat and the microscope head, followed by the specially designed large area scanner and characterizations thereof. Finally, the probe and sample set-up and scanning electronics are discussed.

2.1 Variable-temperature flow cryostat

The scanning microscope is housed in a small variable temperature ^{4}He flow cryostat, the Oxford Instruments OptistatSXM, shown in Figure 2.1. The cryostat consists of two concentric vacuum insulated chambers. The microscope head is at the end of a rod which is inserted in the inner chamber, while the outer chamber holds up to 4 L of liquid helium. The sample space is connected to the He bath by a capillary tube at the base of the outer chamber and the opening is controlled by a needle valve. Sample cooling is achieved by pumping through a port connected to the sample space and drawing cold He gas from the liquid bath through the needle valve and past the sample.

Temperature control is achieved with the needle valve and a resistive heater at

[1] Oxford has since sold their scanning probe microscope division to Omicron NanoTechnology.

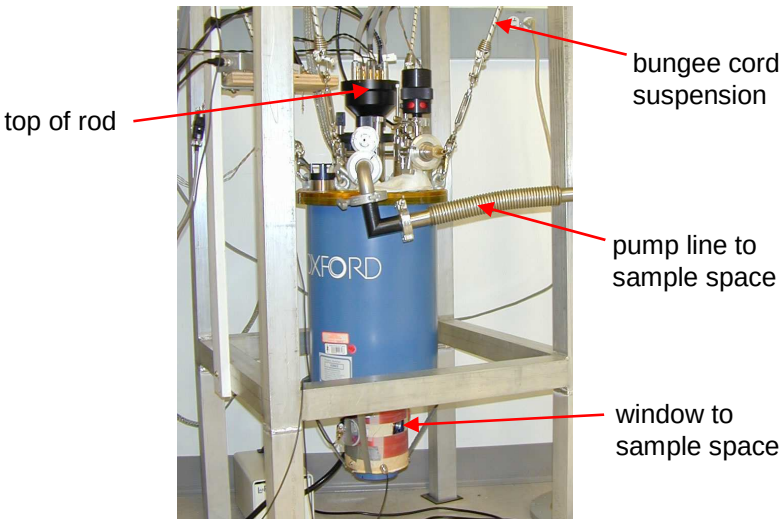

Figure 2.1: The SXM variable temperature ^{4}He flow cryostat.

the base of the sample chamber. The heater is controlled by an Oxford Instruments ITC-503 temperature controller. The ITC reads temperature from two thermometers: a RhFe resistor located at the bottom of the sample chamber, and a Cernox resistor located on the microscope head approximately 1.5 cm to the side of the sample. The ITC feeds back on the RhFe thermometer by adjusting the heater output to maintain a set temperature. The needle valve is not controlled by the ITC and must be set manually to achieve sufficient He flow.

There are two pumps that can be used to cool the sample space. One is a small oil-free diaphragm pump which I typically used in cooling from room temperature down to near the desired operating temperature. The second pump is a larger Leybold SOGEVAC rotary vane pump which can sustain a high pressure flow and enables cooling to a base temperature of 1.7 K. Temperature stability is more easily achieved with the larger pump, so I pumped with the SOGEVAC when taking data even when not near base temperature. The SOGEVAC is housed in an adjacent pump room and is connected to the cryostat through flexible hoses in a T design to minimize forces and vibrations on the cryostat. (I used the diaphragm pump for cooling mainly because it ran quieter.)

The cryostat can either be mounted on an optical table or suspended. Suspending it from an aluminum frame with bungee cords was sufficient to get the needed vibration isolation for Hall probe or SQUID imaging. The suspension scheme also allows easy insertion into or removal from triple layer mu-metal magnetic shielding. The residual magnetic field inside the shielding is at most a few tens of mG, as determined by observations of vortex density in superconducting samples cooled in zero applied field. This residual field may be due to something magnetic inside the shielding.

The sample chamber extends 7″ below the base of the liquid helium chamber and has 5 ports for optical access to the sample space. There are two windows of Spectrosil B quartz for side views 180° apart. The other 3 ports (two side ports at 90° from the windows and one on the bottom) have opaque blanks. The optical access has mainly been a convenience rather than a necessity for my measurements. When the cryostat was not inside the magnetic shielding, I could adjust the sample-probe separation by sight during cooling. Troubleshooting is also easier with optical access in cases where the sample-probe alignment is off or if a bump on the sample is interfering with scanning. The windows also enable visual estimates of the angle between the probe chip and the sample, which is one contribution to the sample-probe height. However, for reasons that are unclear, this has not always given accurate height measurements.

Another advantage of the windows is the ability to expose the Hall probe to light in situ. The Hall probe becomes noisier if the probe is electrically shocked or pressed too far into the sample, but fully recovers with thermal cycling. Exposing the probe to optical photons sometimes seemed to improve the noise, presumably by photo-inducing the release of trapped carriers. During data taking with the Hall probe, the windows were typically covered. A disadvantage of the windows is that they slowly leak from the room into the outer vacuum chamber (OVC) which insulates the He bath. Cleaning the windows and regreasing the O-rings did not stop the leaks. Therefore it has been important to pump out the OVC with a turbo pump for a day before each cooldown. This especially affected the hold time of liquid nitrogen during precooling. Poor vacuum in the OVC had less effect on the He bath hold time, presumably because of cryopumping.

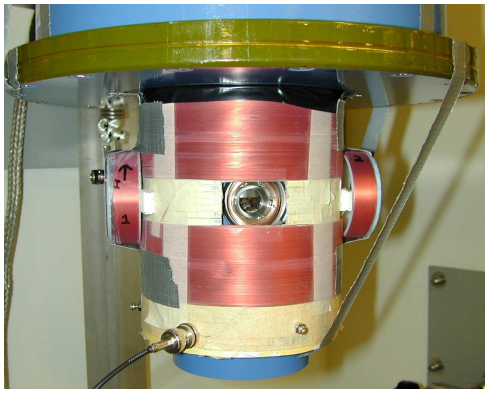

Figure 2.2: Home-wound electromagnets mounted outside the SXM cryostat provide 62 G/A vertically and 4.7 G/A horizontally.

The cryostat is not equipped with a built-in magnet. For my vortex studies only fields of at most a few Gauss were needed. I wound two electromagnets of copper wire and mounted them outside the cryostat centered on the sample. See Figure 2.2. The first provides 62 G/A along the z-axis (vertical and perpendicular to the sample and probe). It has resistance 122 Ω and inductance <0.2 H. Just recently I added another electromagnet to provide a small horizontal field for the partial vortex studies described in Chapter 6. This magnet consists of two 6 cm diameter coils mounted 90° to the windows which together provide 4.7 G/A and have total resistance 25 Ω.

2.2 SXM head

The microscope head consists of two separate piezoelectric scanners. They face each other as shown in Figure 2.3 and either one can be used for scanning. The top scanner is a conventional tube scanner, provides xyz coarse motion, and is standard on the SXM. The bottom scanner is an S-bender design (Siegel et al. 1995) with a larger scan range and is discussed in Section 2.3.

A tube scanner is typically used in scanning tunnelling microscopy (STM) because of its rigidity, simplicity, and compact size. The SXM piezo tube is 2″ long and 0.5″

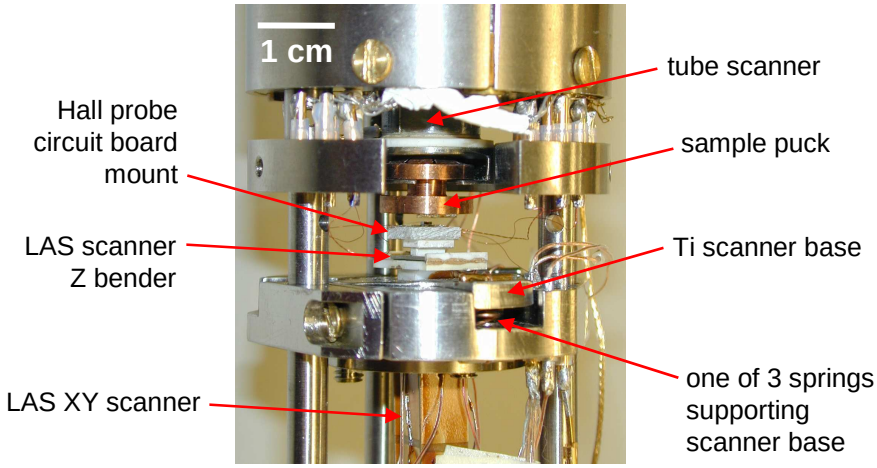

Figure 2.3: The two separate scanners of the microscope head. On top is a tube scanner, used only for coarse motion. It holds a puck on which the sample is mounted. At bottom is a larger area scanner which scans the probe across the sample.

in diameter with a 0.02″ wall. The outer electrode is sectioned into four equal quadrants: +X, +Y, −X, and −Y, which are driven by separate high voltage amplifiers of maximum output ±225 V. In addition, a fifth voltage not exceeding 75 V can be applied simultaneously to the continuous (not segmented) inner electrode to achieve motion in the z direction. The maximum xy scan range with the tube scanner is 19.5 μm at 4 K (as calibrated by Oxford). Larger scan ranges are often desirable in scanning magnetic microscopy, and so I used the large area scanner for all my imaging. The tube scanner was only used for coarse motion.

The coarse motion is inertial stick-slip. A phosphor-bronze puck with a beryllium-copper spring is held in slight compression in a slot at the base of the piezo tube as seen in Figure 2.3. The sample (or probe) is mounted on this puck. For xy coarse motion, an asymmetric voltage waveform is applied to the X or Y quadrants of the piezo tube. The waveform is such that the tube slowly moves in the desired coarse motion direction bringing the puck along with it, then the tube is quickly moved back leaving the puck behind. The slot holding the puck allows xy coarse motion of approximately 3 mm. The spring must be adequately adjusted in order for the coarse motion to work properly, otherwise the puck will not move or will tend to rotate.

At one point the stick-slip xy motion began to fail in first one and then two of the four directions ($\pm$X & $\pm$Y). Inspection of the piezo tube revealed that the electrodes were flaking off the piezo quadrants. The electrodes had been coated with insulating Kapton® varnish and it seems that repeated thermal cycling cracked the varnish, which then flaked off with the electrode attached. Rapid thermal changes >5 K/min are bad for the piezos, however warming and cooling of the SXM was typically no faster than 3 K/min. I replaced the tube scanner with a new assembly from Oxford which intentionally had varnish only in essential locations, and I did not have further problems with the xy coarse motion.

For the z coarse motion, the entire tube scanner rides up and down on three hollow quartz cylinders each connected to a piezo stack. The asymmetric voltage waveform is applied to these piezo stacks to achieve inertial stick-slip motion of the whole scan tube assembly on which the sample (or probe) is mounted. The full z range is nearly 1 cm, however at low temperature I found that the z coarse motion worked reliably only for a restricted range. For this reason it was necessary to approach the sample to the probe first at around 90 K before cooling to lower temperatures to ensure that the probe was within range.

Near the sample puck are sockets to make electrical connections to the sample and probe. These sockets are attached to 4 shielded twisted pairs (8 wires total) and 2 coaxes that extend to the top of the rod. These connections, as well as the piezo voltage connections and the leads to the Cernox thermometer, exit the sample chamber through vacuum tight connectors on top of the rod. I also wired the rod for 6 additional sample/probe connections. These wires are in unshielded twisted pairs to the top of the rod where they exit through the thermometer connector and utilize extra wires in the temperature control cable. The wires are not well shielded or in twisted pairs outside of the sample space, but are adequate for some applications when additional connections are needed.

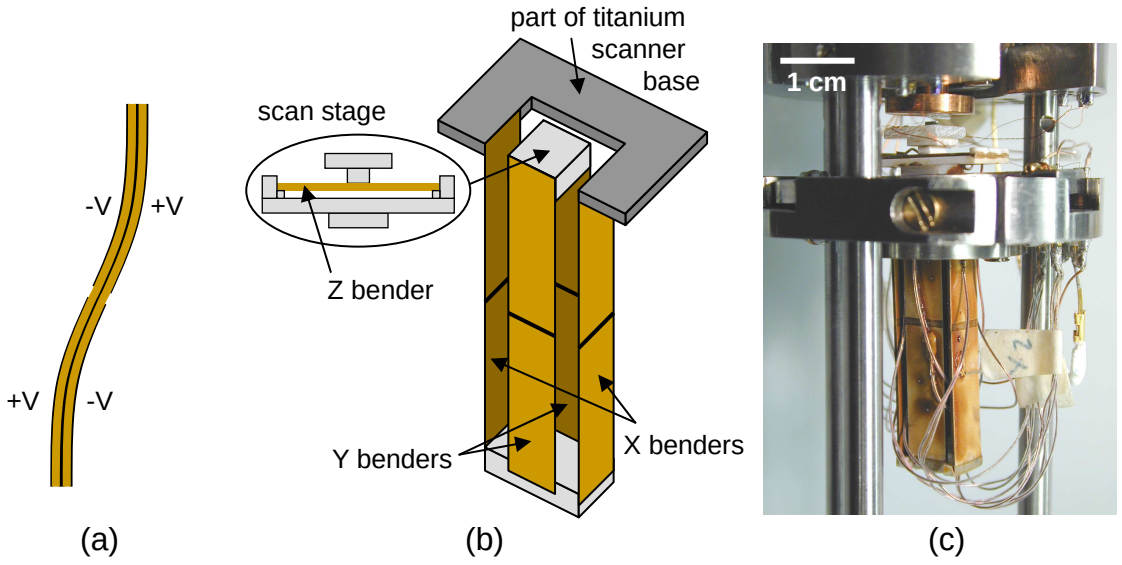

Figure 2.4: Large area scanner built in an S-bender design as originally demonstrated by Siegel et al. (1995). (a) Side view of one of the XY benders. Opposite voltages on the 4 electrodes bend it in an "S" shape. (b) Drawing of the large area scanner (not to scale). The scan stage assembly shown separately is attached to the upper Macor® piece. (c) Photo of the SXM large area scanner.

2.3 Large area scanner

The probe was scanned with a specially designed large area scanner (LAS) to achieve a larger scan range than possible with the tube scanner. This scanner consists of four 1.5″ piezoelectric benders for X and Y and one 0.75″ bender for Z. The benders have a center brass shim with piezoceramic on both sides. Each XY bender has four electrodes so that when opposite voltages are applied the bender forms an "S" shape as shown in Figure 2.4(a). The scanner is configured in a design scheme originally demonstrated by Siegel et al. (1995). See Figure 2.4(b&c). The bottom of the four XY benders are attached to a Macor® piece. The top of the X benders are fixed to a titanium scanner base, which is attached to the main microscope body. The top of the Y benders are glued to another Macor® piece to which the Z bender and scan stage are attached. The probe (or sample) is mounted on this stage. In this way independent X and Y motions are achieved by applying equal + and − voltages to the

X or Y benders. The Z bender has two electrodes and is mounted horizontally with both ends fixed. One side is grounded while the other is supplied with a maximum of ±150 V. This allows independent Z motion. A 5 mm × 5 mm Macor® stage is mounted on the Z bender and the probe setup is glued to this stage.

The titanium plate to which the X benders are fixed is attached to the main microscope body by three springs. This plate can be tilted by means of three set screws which control the spring extensions in order to adjust the probe-sample alignment.

At room temperature the LAS moves ∼0.6 μm/V in X and Y, where the voltage is the voltage difference between the + and − electrodes. At 4 K the motion decreases to ∼0.11 μm/V. The scan range at 4 K is limited by the voltage difference at which the piezos begin to arc. I found this to happen for scans larger than 60 μm × 60 μm, or a voltage difference >270 V (±135 V on the opposite electrodes). When pumping He through the sample space with the SOGEVAC pump, the pressure as measured by a gauge near the pump is several Torr, which I've been told is a bad helium pressure for arcing. A larger scan range could be achieved by changing to longer benders.

2.3.1 Piezo resonances and vibrational noise

I studied the resonant frequencies and vibrational noise of the LAS at room temperature early on in my research. These measurements were made with the microscope in the cryostat and the cryostat suspended by bungee cords as when scanning, but the pump was not connected. The lowest mode of the scanner is ∼40 Hz.

The resonances were studied by mounting pieces of silicon wafer to the scan stage parallel to the X and Y piezo benders. A Polytec Series 3000 vibrometer was used to bounce a laser off the Si to measure its velocity. The + electrodes of the X and Y benders were driven, one direction at a time, with a small sinusoidal voltage of 10 mV at frequency f, and the velocity response at f was recorded. This measurement was made for a sweep of f to give the scanner response as a function of frequency. The velocity response measured by the vibrometer was converted to amplitude by dividing by $2\pi f$. The response of the LAS in μm/V is shown as a function of drive frequency in Figure 2.5. The first mode is just below 40 Hz for both X and Y, and a large resonant

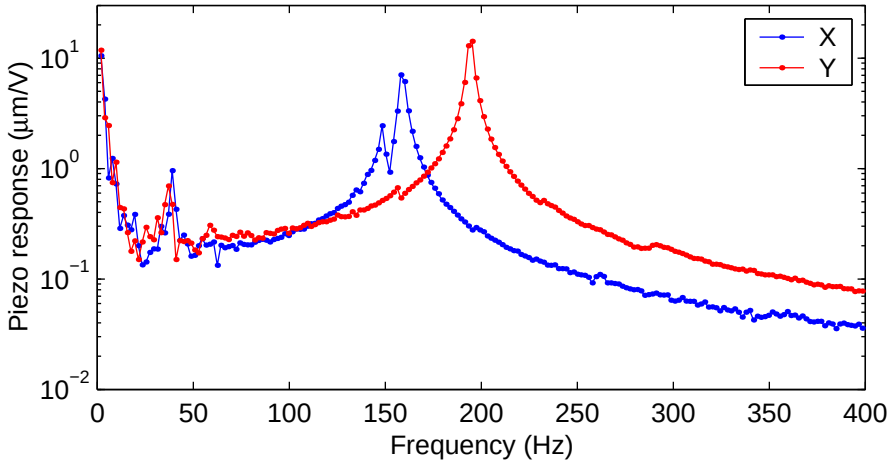

Figure 2.5: Resonances of the LAS. The LAS motion in X (Y) was measured with a vibrometer while a sinusoidal voltage of 10 mV was applied to the + electrodes of the X (Y) benders for a sweep of frequencies.

peak at 158 and 195 Hz also appears for X and Y respectively. The low frequency data (<75 Hz) in Figure 2.5 are not clean. Other data with a higher drive voltage suggest that all but the peak near 40 Hz is just noise at these lower frequencies.

The 40 Hz resonant frequency is a limitation on scan speed. However, typically I did not take Hall probe scans faster than 1 Hz (per line) for good images and 3 Hz for test images, as limited by the Hall probe measurement scheme (detailed in Section 3.6). The piezo drive voltage is a triangle wave, which means there are higher frequencies at the beginning and end of a scan line. If faster scanning was desired one might need to implement a different scanning piezo voltage function that decelerates near the extremes and thus turns around more gradually to minimize higher frequencies. However, at our low frequency scans this has not been an issue.

I also made measurements of the vibrational spectrum of the X and Y benders of the LAS. When a voltage is applied to a piezoelectric material it expands or contracts. For a bender, it bends when one side expands and the other contracts. Conversely, if a bender is mechanically bent a voltage will be produced. With no drive voltage, I measured the frequency spectra of the voltage between the + and − electrodes on the X and Y benders and converted to distance units using the room temperature piezo

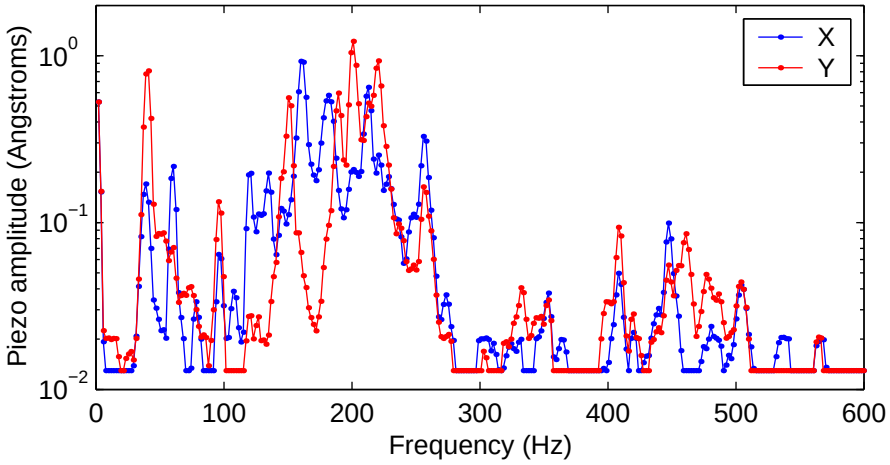

Figure 2.6: Frequency spectra of piezo vibration amplitude for the X and Y benders of the LAS. The amplitude was obtained from the voltage difference produced by the benders. The data are flat at 0.013 Å due to an insufficient sensitivity setting on the spectrum analyzer.

calibration 0.67 μm/V. The spectra for the X and Y benders are shown in Figure 2.6. The amplitudes are surprisingly small, only a few peaks are above or near 1 Å peak amplitude. This method of measurement only considers the modes related to piezo bending. Not surprisingly, there are more peaks in the vibration data than in the resonance data. Note that the resonance peaks clearly appear also in the vibration data.

2.3.2 Piezo calibration

It is important to know the calibration of a piezo scanner in order to convert volts to distances in the temperature range of interest. Piezoelectrics can depole over time which reduces their motion per applied voltage. Arcing can also cause depoling and decrease the piezo coefficient. Thus it is important to have a convenient way to periodically calibrate the scanner.

Ideally a magnetic sample would be used to calibrate a magnetic microscope scanner so that the probe would not need to be changed. I have not found an adequate magnetic sample for XY calibration and instead I operated the SXM as an STM to

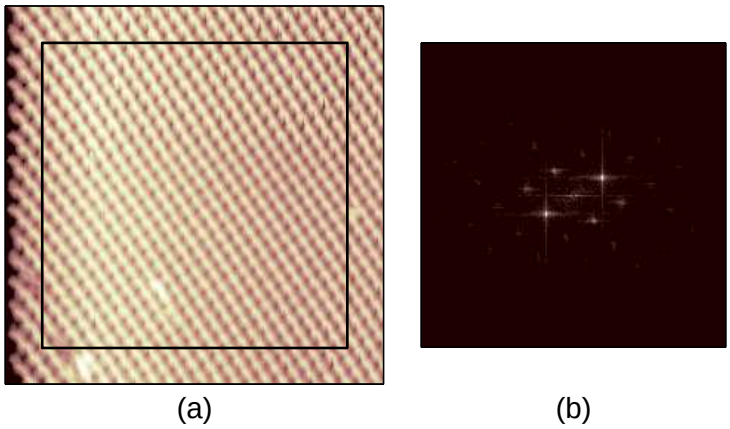

Figure 2.7: STM image and FFT of a gold calibration grid. (a) STM image at $T = 10.3$ K of a gold grid with 1 μm spacing. The voltage differences applied to the X and Y benders were -112.5 V to $+112.5$ V for the scan. (b) FFT of the portion of image (a) inside the crop box.

obtain images of a calibrated gold grid. The Z bender was calibrated from images of a vortex in a superconductor with a small penetration depth where the vortex looked like a monopole.

XY calibration

For the XY calibration I initially used a sample with alternating magnetic bits of known spacing (shown in Figure 1.4(b)). This sample was a good starting point, but did not allow for independent calibration of the X and Y directions simultaneously. There is no a priori reason for the calibrations to be exactly the same for the two directions.

Simultaneous calibrations of the X and Y piezos was achieved by STM imaging of a 1 μm gold grid. A low temperature STM image of the grid and a discrete 2D Fourier transform (FFT) are shown in Figure 2.7. The image is distorted slightly at the edges of the scan, particularly at the left edge. This image was taken from left to right with vertical line scans from bottom to top. The FFT was taken for a cropped region of the image as shown, leaving out the distorted edges. Thus the calibrations obtained are most accurate for features away from the edges of an image.

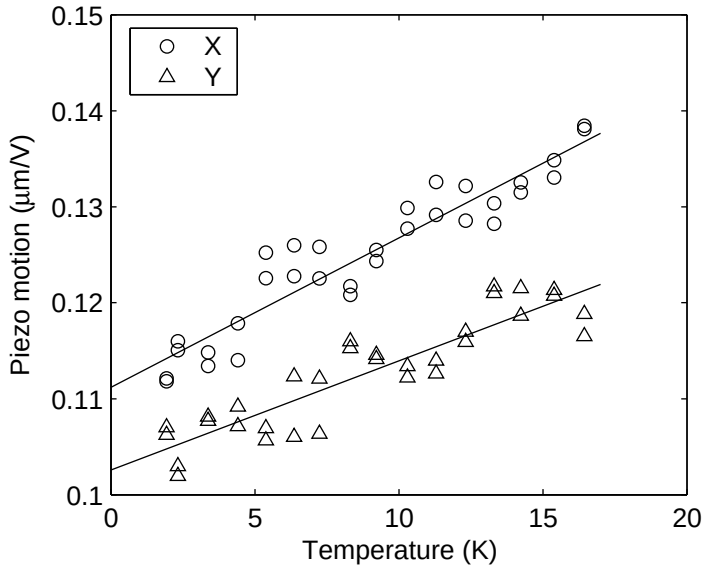

Figure 2.8: Low temperature calibration data for the large area scanner (LAS) obtained from STM images of a gold grid. The two data points per temperature are from forward and reverse scan line images. The linear fits give the calibration functions used to convert the size of scanning probe image to microns for $T < 20$ K.

STM images of the gold grid were taken at a range of temperatures. The Fourier-space basis vectors of the grid can be obtained by eye from the 2D FFT or using a fitting script written by Hendrik Bluhm that fits Gaussians to the peaks in Fourier-space including the harmonics. The X and Y calibrations are easily obtained in μm/V from the basis vectors. Figure 2.8 shows the most recent low temperature calibration using this method. The calibration appears step-like in temperature due to the limited number of pixels in the discrete Fourier-space. However, images were taken at many temperatures and so fits to these data should not be significantly skewed by the lack of resolution in Fourier-space. For this low temperature range <20 K, the calibration looked linear in temperature and so I used linear fits as shown as for the X and Y calibrations. Note that the calibrations are not the same for X and Y.

Ideally, it would be very nice to have a magnetic grid that could be easily imaged with the Hall probe so that only the sample and not the probe would need to be switched in order to perform the calibration. Hendrik Bluhm and I attempted a

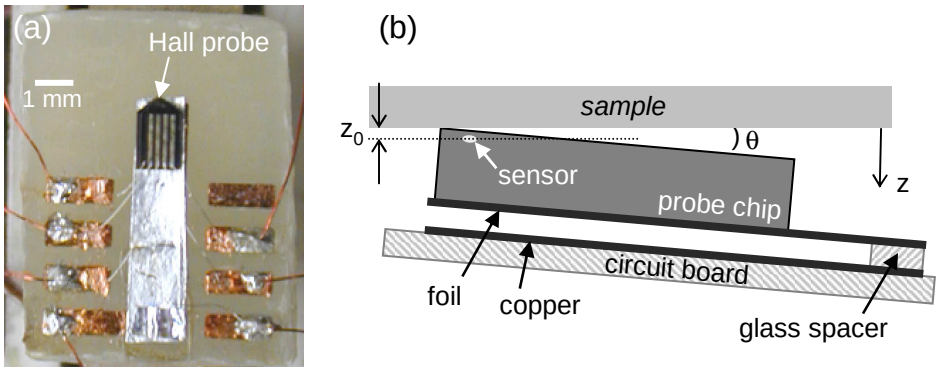

Figure 2.9: The Hall probe mount. (a) The probe is mounted on Al foil which forms a parallel plate capacitor with an underlying Cu pad for height control. Al wire bonds make electrical connection to the probe. (b) Side view sketch of the Hall probe mount, not to scale. The alignment angle θ affects the minimum height z_0 of the probe active area above the sample.

calibration using the Hall probe to image the magnetic field from the current in a wire meander designed with loops of 5 μm spacing. We were not able to see anything in images of this sample, perhaps because of breaks in the meander or poor alignment. An ideal sample would be a grid of small strongly magnetized features.

Z calibration

The LAS Z-bender was calibrated from Hall probe images of an isolated vortex in a superconductor with penetration depth $\lambda \sim 70$ nm. Hendrik Bluhm took these images for a range of probe heights by changing the voltage applied to the Z-bender. I fit the vortex images to the monopole model (see Appendix A.1) and extracted the parameter $(z + \lambda)$, where z is the height of the sample above the surface. The resulting data of z versus Z-bender voltage were quite linear and gave 6.8 nm/V, or 2.0 μm for the full range of V_z from -150 to $+150$ V at 4.4 K.

2.4 Probe and sample set-up

The Hall probe is shown mounted on a small circuit board in Figure 2.9(a). This

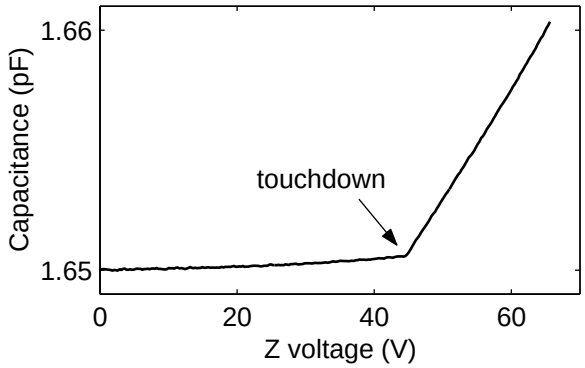

Figure 2.10: Capacitance curve for sample-probe z positioning. Parallel plate capacitance versus voltage applied to the Z piezos of both the LAS and tube scanner at room temperature.

circuit board is mounted on the LAS stage. The Hall probe is glued with GE varnish to the end of an aluminum foil diving board. The foil is attached to a glass spacer 160 μm thick which is mounted on a copper pad extending the length of the foil. This creates a parallel plate capacitor of $\sim$1 pF (see Figure 2.9(b)). The copper and aluminum capacitor plates are connected by separate shielded coaxes to a General Radio 1615-A analog capacitance bridge. The bridge is run with an SR530 lock-in. Deflection of the Hall probe and thus also the foil shows up as a change in capacitance. In this way the location of the sample surface in the z direction can be determined from a capacitance versus Z voltage sweep. The point at which the capacitance abruptly begins increasing indicates the z position at which the probe touches the sample. See Figure 2.10 for an example C versus V_z curve. At low temperature the touchdown point can be determined with an accuracy of $<$10 nm. However, if the sample or probe is charged there can be an attractive force that causes the probe to snap-in or a repulsive force that delays touchdown. These situations decrease the accuracy in the z measurement of the sample's position.

The capacitance signal can also be used to obtain a crude topography map by operating with the probe slightly pressed into the sample. This can be useful to determine if there are uneven spots on the surface. Ideally the sample surface is smooth and flat. The probe and sample are rarely perfectly aligned, so there is an

angle between the scan plane of the probe and the plane of the sample surface. This is compensated by a home-built analog circuit box that gives a Z voltage corresponding to a plane as a function of X and Y piezo voltages. The slopes m_x and m_y of the plane are controlled by potentiometer knobs and the values are obtained by checking the touchdown points on the surface for 3 or more locations within the image area.

A drawback of the way the probe and sample are mounted is that it is not possible to fine adjust both the angle of the probe and the angle of the LAS scan plane to the sample surface. This is because the probe rather than the sample is attached to the scanner, and the angle between the probe and scan plane is not fine tunable (it is determined by the angle of the aluminum foil). The three tilt screws for the LAS do allow fine adjustments of the scan plane, but if it is adjusted parallel to the sample surface often the angle of the Hall probe to the sample is too large or too small. One solution would be to mount the probe on the sample puck which is held by the tube scanner and kept stationary, and mount the sample on the LAS stage. This has two major drawbacks which outweigh the alignment issue. First, it is not nearly as easy to switch samples as when the sample is mounted on the puck. Second and more fundamental is that this arrangement would scan the sample rather than the probe. For many samples this would not be an issue, but the vortices observed in the very underdoped YBCO studies were sometimes rather mobile, especially the "partial" ones discussed in Chapter 6, and vortex motion might be induced by scanning the sample.

Electrical connection is made to the Hall probe with aluminum wire bonds from copper pads on the circuit board (Figure 2.9(a)) to the end of the Hall probe contact pads furthest from the Hall probe tip. For large samples it is important to bond the wires as far from the tip as possible since the 0.001″ wire width is the limiting factor on the angle between the probe and sample. Many of the $YBa_2Cu_3O_{6+x}$ crystals were smaller than the Hall probe and thus the wire bonds could hang off the edge of the sample and were not an issue. Typically I polished the aluminum foil on which the probe was mounted to make it thinner to reduce its spring constant and minimize the force between the probe and sample when touching. However, it became apparent that the wire bonds to the Hall probe were the most significant contribution to the

spring constant. Thin copper wires were soldered to the circuit board pads and connected on the other end to the sockets in the microscope. The wire chosen was the thinnest reasonable to work with to ensure that the wires would not hinder the scanning of the probe.

2.5 Scanning hardware and software

The scanning and coarse motion was done with the commercial TOPS 3 System from Oxford Instruments.[2] Initially I also used the TOPS hardware and software and the attached computer for data acquisition. I later switched to taking data on a separate computer because TOPS caused noise problems with the Hall probe.

The TOPS system has 5 high voltage amplifiers: +X, −X, +Y, −Y, and Z. The four XY amplifiers have full range ±225 V and the Z amplifier is set for ±150 V but the maximum amplitude can be adjusted. (I recently increased this Z amplitude from ±75 V in order to enable larger area scans without maxing out the fly-in-plane.) The coarse motion waveforms are also produced and controlled by the TOPS system. TOPS has 8 differential analog-to-digital inputs for recording the sensor signal. Brian Gardner wrote a nice program to input images from the TOPS data format to MABLAB®.

I stopped acquiring data with the TOPS system after noticing scan related noise in Hall probe images in 2002. See Figure 2.11. The noise was systematic, as it appeared as steps in the signal at fractions of the scan size, the most prominent at $\frac{1}{4}$, $\frac{1}{2}$, and $\frac{3}{4}$ of the scan line. To eliminate the intrinsic $1/f$-like noise of the Hall probe, images are taken quickly and averaged together. However, averaging just brought out this TOPS scan step noise. The noise was also subtly present in early images taken with a 2 μm Hall probe, but back then the data taking was not yet optimized and other noise dominated. I was never able to pinpoint the cause of this step noise, though it seemed that there was a significant grounding problem with the A/D inputs to the TOPS system. Changing the gain did not change the signal-to-noise, and putting an isolation amplifier between the Hall probe output (from a lock-in) and the A/D

[2]The TOPS system is no longer produced.

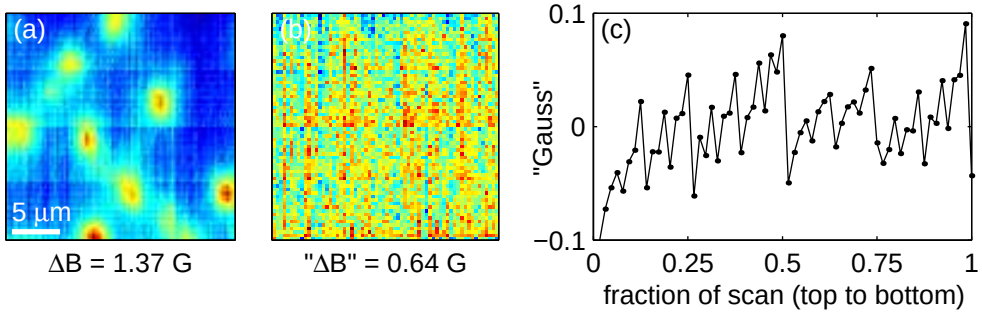

Figure 2.11: Noise steps in images due to TOPS electronics. (a) Image of vortices in a $T_c = 8.3$ K YBCO crystal at $T = 2.2$ K. The horizontal jumps are caused by the data acquisition electronics. The image was taken with vertical scan lines and is an average of 20 images. (b) Image of nothing to examine the noise jumps. Average of 10 images. (c) Plot of the mean of each row from image (b), clearly showing the noise steps. Note: The vertical streakiness in the images is due to low frequency noise intrinsic to the Hall probe.

inputs did not solve the problem. I overcame this issue by bypassing the TOPS system entirely for data input. I wrote a MABLAB® program to take the data using a separate computer with an A/D card while TOPS controlled the scan motion. My program records the voltages applied by TOPS to the X, Y, and Z piezos and triggers on each new scan line and records the Hall probe signal. When the Hall probe lock-in is not connected at all to TOPS the step noise is not present.

The above data taking scheme, though successful, is cumbersome and requires redundant scan parameter inputs by the user. Another noise issue with TOPS occurred when using a scanning SQUID. The SQUID output became much noisier when the TOPS system was on. For both of these reasons it will be desirable for a future user to implement a new scan system, perhaps fully home-built.

Chapter 3

Submicron scanning Hall probes

In addition to implementing the scanning Hall probe microscope (Chapter 2) and using it for vortex imaging studies in very underdoped $YBa_2Cu_3O_{6+x}$ (Chapters 4–6), I also fabricated submicron scanning Hall probes from GaAs/AlGaAs two-dimensional electron gas (2DEG). The smallest probes from this fabrication were 0.5 μm lithographically, a factor of four smaller than the previous probes I was using, and enabled measurements of the apparent vortex size (Chapter 5) and partial vortex imaging (Chapter 6) in the YBCO.

There are numerous qualities to consider when selecting and developing a scanning magnetic sensor: spatial resolution, magnetic field sensitivity, ease of interpretation, extent of sample preparation, temperature and field range, and dynamic speed. The three sensors used in the Moler Lab (MFM, SQUIDs, and Hall probes) were compared in Section 1.1.1 and Table 1.1. The main advantages of Hall probes are that they directly measure the magnetic field, can be made at least as small as $\sim$100 nm, are non-invasive, and operate over a large temperature range (0–300 K).

This chapter gives a brief review of the Hall effect, details my fabrication of 0.5–2 μm Hall probes with gates, and lastly describes noise measurements made on these and later probes. My probes improved the spatial resolution of the scanning Hall probe microscope at least four-fold, and the addition of a grounded gate over the active area improved image quality by screening out local electric fields. The noise studies of scanning Hall probes ranging in size from 0.13 μm to 10 μm show that field sensitivity decreased for smaller probes, but flux sensitivity increased. This

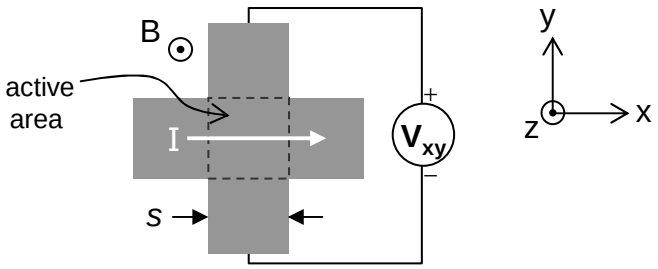

Figure 3.1: The Hall cross. The Hall voltage V_{xy} is proportional to the current I in the x direction and the z component of the magnetic field B within the active area.

suggests that sub-100 nm Hall probes could be fabricated without compromising flux sensitivity.

3.1 The Hall effect

Hall probes are based on the simple principle of the Hall effect, discovered by Hall (1879). If a current carrying conductor is placed in a perpendicular magnetic field, a transverse voltage (the Hall voltage V_{xy}) appears due to the Lorentz force on the charge carriers. This voltage is proportional to the current and field, and inversely proportional to the carrier density n of the conductor. The Hall effect is often used to determine n and the sign of the charge carries in a material, however it can also be used to measure a magnetic field if n is known. The basic geometry of a Hall probe, the Hall cross, is shown in Figure 3.1.

The equation for the Hall effect[1] in three dimensions is given by

$$V_{xy} = -\frac{I_x B_z}{n_{3D} q t}, \tag{3.1}$$

where q is the charge of the current carriers and t is the conductor thickness in the z direction. Decreasing n_{3D} increases the response of the Hall voltage to changes in magnetic field. Our Hall probes are made from a two-dimensional conductor (described in Section 3.3) with very low carrier density. In 2D the Hall effect equation

[1]For more details on the Hall effect a good reference is Seeger (1997), section 4.2.

becomes

$$V_{xy} = \frac{I_x B_z}{n_{2D} e} = R_H I_x B_z, \tag{3.2}$$

with the charge carriers taken to be electrons ($q = -e$) and the Hall coefficient defined as $R_H = (n_{2D}e)^{-1}$.

The above discussion has assumed a constant B-field distribution and ignored any effect of the voltage leads on the current flow. There are two regimes to consider: diffusive transport where the mean free path of the carriers is much less than the Hall probe dimensions, and ballistic transport where the mean free path is much larger than the probe dimensions.

In the diffusive limit, the current density extends partially into the voltage leads, and approximately doubles the effective area of the probe (Bending and Oral 1997). If the magnetic field varies on a length scale much smaller than the Hall probe dimensions, a response function of the Hall probe voltage to the inhomogeneous magnetic field must be computed in order to accurately interpret the Hall probe images. Bending and Oral (1997) compute the Hall probe response function numerically for the example of the field from a vortex. Thiaville et al. (1997) have calculated an analytical response function of an idealized Hall cross (i.e. two perpendicular infinite straight arms). If the field does not vary significantly over the Hall probe area, then it is reasonable to approximate the field as constant over the probe area, with some smoothing due to the finite Hall probe size. In addition to spatial resolution concerns, this is additional motivation to make smaller Hall probes (so that the convolution of the field with the probe is minimal). In my vortex imaging in very underdoped $YBa_2Cu_3O_{6+x}$, the B-field did not vary rapidly over the 0.5 μm $\times$ 0.5 μm probe area located at a distance $>$0.4 μm from the sample, so I approximated the convolution of the field with the probe as simply the average field over the probe area (i.e. the integral of the B over the probe area, divided by the probe area).

In the ballistic limit, the charge carriers primarily do not scatter while in the probe area. In this regime the active area is essentially just the square intersection of the current and voltage leads in an idealized probe geometry. Peeters and Li (1998) calculated the response of a ballistic Hall probe in the presence of an inhomogeneous

magnetic field and found that for low magnetic fields the Hall response is determined simply by the average field in the cross region. However, undesirable behavior for typical Hall probe measurements – namely quenching of R_H – can occur in the ballistic regime. Simplistically, quenching at small fields occurs because the field does not bend the trajectory of the carriers enough to get them into the voltage leads. Ford et al. (1989) made Hall crosses of various geometries in the ballistic limit and observed quenching, enhancement, and even negative R_H. Thus it is desirable to make Hall probes in the diffusive regime, that is, from a material with an effective mean free path smaller than the probe dimensions.

There is another deviation from the idealized Hall cross in Figure 3.1 that should be mentioned. In the two-dimensional electron gas systems from which Hall probes are often made, the carrier density n_{2D} is not constant over the probe, it peaks at the center and falls off at the edges. This is more significant in smaller probes as the fall-off length of n_{2D} becomes comparable to probe size. In very small probes, the center n_{2D} peak can be suppressed below the bulk n_{2D}. Because of the non-constant n_{2D}, it is necessary to measure the effective Hall coefficient for each probe. The spatial variation of the carrier density is another motivation to make smaller probes in order to minimize complicated convolution (and image processing deconvolution) of the imaged magnetic field with the unknown density profile of the probe.

3.2 Motivation for 2^{nd} generation Hall probes

The first generation of Hall probes in the Moler Lab had nominally 2 μm $\times$ 2 μm active areas defined by optical lithography and wet etching. These probes were fabricated mainly by Kathryn Moler at IBM Yorktown on GaAs/AlGaAs wafers grown by David Kisker. I made the contacts on these probes, which are shown in Figure 3.2. I used these first generation Hall probes successfully for imaging vortices in very underdoped $YBa_2Cu_3O_{6+x}$ while searching for $2\Phi_0$ vortices as discussed in Section 4.2. While these probes were quite sufficient to determine if a vortex carried flux $2\Phi_0$ or Φ_0, there were two main reasons to make a second generation of improved Hall probes for future experiments. The first was the desire for better spatial resolution,

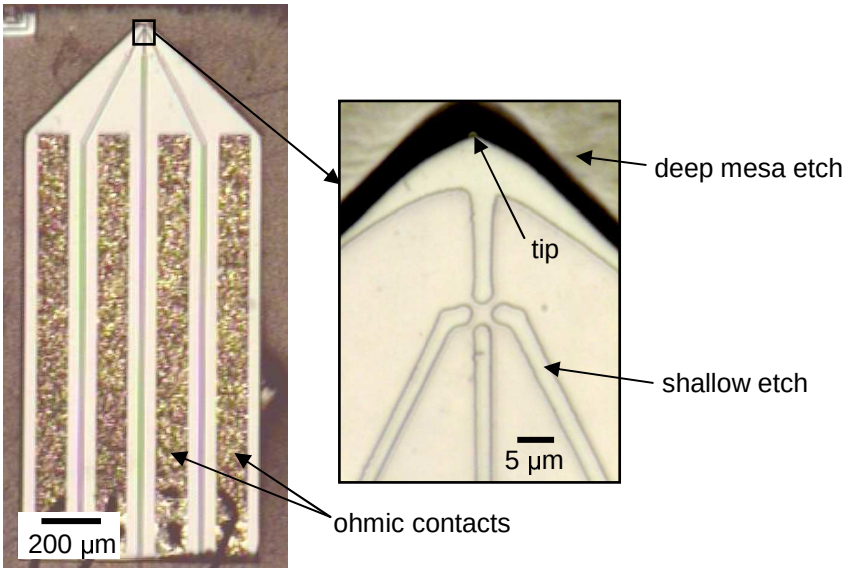

Figure 3.2: First generation 2 μm Hall probes.

particularly for studying vortex field profiles, and the second was to include a gate over the active area to screen out interfering electric fields.

The spatial resolution of a magnetic image is roughly $\sqrt{s^2 + h^2}$, where s is size of the Hall cross active area and h is the height of the sensor above the sample. To obtain the best spatial resolution, both s and h need to be minimized. Also, by making s comparable to or smaller than the spatial variations of the imaged field, the less important it is to account for convolution of the field with the active area geometry and n_{2D} spatial variations, both of which are not easily measured. For the second generation of Hall probes, I fabricated probes with s lithographically as small as 0.5 μm. The minimum probe height is determined by the depth d of the active area below the surface, the distance l between the active area and tip, and the sample-probe angle θ by the relation $h_{\min} = d + l \sin\theta$ for small angles.[2] To decrease h, I made $l \approx 8$ μm for the 0.5 μm probes, three times smaller than for the first generation probes.

The need for a gated Hall probe became clear after imaging samples that had

[2]For probes with a gate that coats the tip (like those discussed here), the gate metal thickness also add to $h_{\min}$.

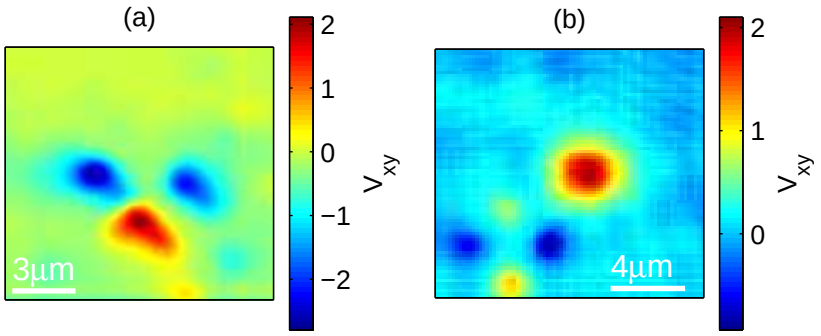

Figure 3.3: Four-fold electric charge pattern in images taken with an ungated 2 μm Hall probe. (a) On an LSCO thin film. The top lobe did not appear in this case (see text). Image width 12.8 μm. (b) Next to a vortex (center) in a YBCO crystal. Image width 14.4 μm.

stray charges on the surface. Often just touching or dragging the Hall probe on the surface left behind charged particles, possibly GaAs dust. The images in Figure 3.3 show the typical four-fold pattern, which we believe result from localized electric fields altering the carrier density of the Hall probe as the active area corners passed over a charged particle. Further investigation with alternate arrangements of current and voltage leads on the Hall cross were consistent with this explanation. The image in Figure 3.3(a) does not show the top lobe, perhaps due to the angle of the probe or specific geometry of the probe, though a fourth lobe was apparent at this site when alternate (non-transverse) current voltage arrangements were tested. This electric field disturbance can interfere with the desired mapping of the magnetic field. When there is only one big charged particle, it is easy to distinguish the E and B effects (e.g. the vortex in Figure 3.3(b) is still obvious despite the four-fold pattern in the lower left). In some cases, though, the electric charges obscured the measurement of interest, such as in the images I took of the response of a YBCO ring to an applied B-field shown in Figure 3.4. Fortunately, for those data it was possible to subtract the E-field contributions. The stray charges problem was solved by putting a thin grounded gate on top of the Hall probe to screen out electric fields effects without disturbing the magnetic measurement.

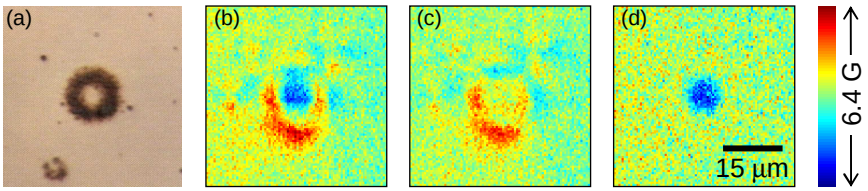

Figure 3.4: Image of an optimally doped YBCO ring obscured by electric charges, taken with a 2 μm ungated Hall probe. The ring was cooled to $T = 70$ K in zero field. (a) Optical image of a YBCO thin film ring fabricated by Rafael Dinner. (b) Raw V_{xy} image in an applied B-field of 6.5 G. (c) Raw V_{xy} image in zero applied B-field. All the features in this zero-field image are due to local electric charges perturbing the Hall probe carrier density. (d) Clean image of the ring shielding the applied 6.5 G field obtained by subtracting (c) from (b).

3.3 GaAs/AlGaAs 2DEG

The chosen material for the Hall probes is a GaAs/AlGaAs heterostructure with a two-dimensional electron gas (2DEG) just below the surface. This material is desirable because the carrier density (n_{2D}) of the 2DEG at low temperatures can be set very small during the heterostructure growth process by tuning the number of dopants. Also, the mobility (μ) can be very high, decreasing the resistance of the leads.

Our first and second generation Hall probes were fabricated on wafers grown using chemical vapor deposition by David Kisker, formerly at IBM. This 2DEG lies 140 nm below the wafer surface. The wafer structure is shown in Figure 3.5. Our third generation Hall probes were made by Clifford Hicks on a shallower (40 nm deep) 2DEG grown using molecular beam epitaxy by Hadas Shtrikman at the Weizmann Institute of Science (WIS). These newer probes are described briefly in Section 3.4.5. The structure of the WIS 2DEG is shown in Figure 3.6 along with a conduction band diagram.

The 2DEGs are designed such that the conduction band forms a sheet of electrons at a GaAs/AlGaAs interface (Figure 3.6). The thickness of this sheet perpendicular to the layers is narrow, confining the electrons to two-dimensions and they exhibit two-dimensional physics. Above the 2DEG is an undoped $Al_{0.3}Ga_{0.7}As$ spacer layer,

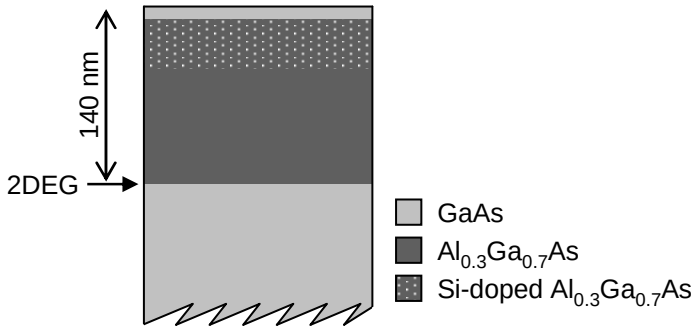

Figure 3.5: 2DEG structure for our 1st and 2nd generation Hall probes. The bottom GaAs layer shown is not the base wafer, rather it is also grown by chemical vapor deposition to achieve a high-quality substrate. Grown at IBM by David Kisker.

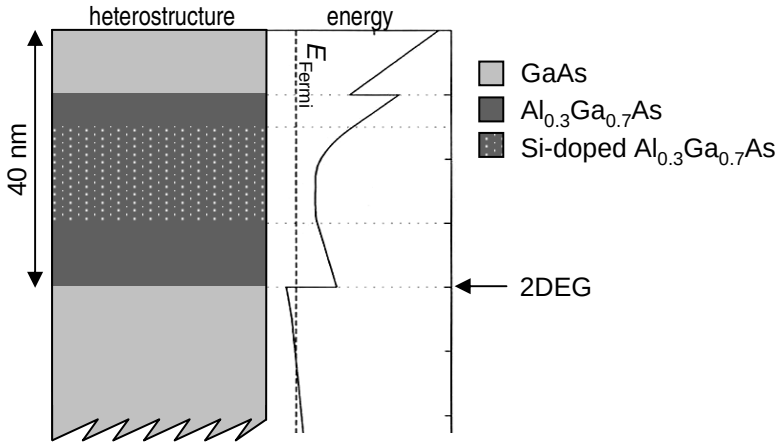

Figure 3.6: 2DEG structure grown at Weizmann by Hadas Shtrikman for 3rd generation probes. Also shown, the conduction band energy (calculation done by Clifford Hicks).

Table 3.1: Properties of the two GaAs/AlGaAs 2DEG heterostructures used for our Hall probes. The range of lithographic cross sizes of (working) probes we fabricated from each structure are also given.

Bulk Values (at 4 K)	IBM structure (David Kisker)	Weizmann structure (Hadas Shtrikman)
2DEG depth	140 nm	40 nm
2D carrier density	5×10^{11} cm^{-2}	4×10^{11} cm^{-2}
mobility	5×10^{4} cm^2/Vs	3×10^{5} cm^2/Vs
mean free path	0.6 μm	3 μm
Hall probe sizes	0.5 to 2 μm	0.13 to 10 μm

followed by a silicon-doped $Al_{0.3}Ga_{0.7}As$ layer in which the Si atoms act as electron donors for the 2DEG and the Si ions create the necessary band bending. The presence of the spacer layer significantly reduces impurity scattering. At top is a GaAs cap which terminates the structure to prevent Al oxidation.

Table 3.1 gives some properties of the IBM and WIS structures. Note that the bulk mean free path (which was calculated from the other parameters) is larger than some of the probe dimensions. But all the probes exhibited constant R_H versus field (measured for low fields up to a few hundred Gauss), indicating that the effective mean free path in the active area was reduced below the bulk value and we were always in the diffusive regime. The smallest probe of 130 nm made from the WIS 2DEG had a Hall coefficient $\sim$30% higher than that of the much larger probes, meaning that the average n_{2D} was measurably reduced below the bulk value in this smallest probe.

Depth of the 2DEG is the ultimate limit on the sample-probe distance h. The depth also limits the size s of Hall probe than can easily be fabricated due to 2DEG depletion next to a boundary (discussed in Section 3.4.1). Thus for good spatial resolution, it is desirable to start with a shallow 2DEG. The 140 nm depth of the IBM 2DEG is not very shallow by today's standards. 2DEGs as shallow as 20 nm have been grown (Goldhaber-Gordon et al. 1998), and surface 2DEGs such as InAs are also being explored. Shallower GaAs/AlGaAs 2DEGs are more difficult to grow reliably and may be noisier as the spacer layer is forced smaller and the dopants are

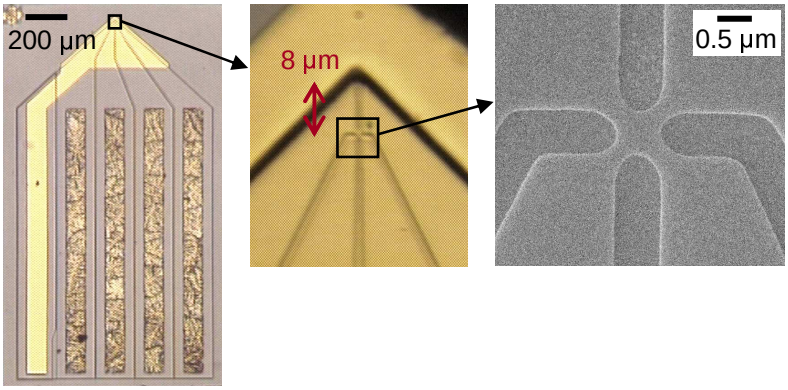

Figure 3.7: Second generation Hall probes. Shown here is one with a 0.5 μm cross. The final manual polish (to bring the chip edge close to the deep mesa tip) had not yet been done on the probe in the leftmost image.

more closely spaced. Our third generation Hall probes were able to be made with lithographic dimension as small as 130 nm because they were made on the shallower 40 nm WIS 2DEG.

3.4 Hall probe fabrication

In 2001 I fabricated our second generation Hall probes (Figure 3.7) in the Stanford Nanofabrication Facility (SNF) and in the student microfabrication lab in Ginzton. The Hall cross active areas ranged in lithographic size from 0.5 μm to 2 μm. The fabrication consists of four steps on a piece of wafer slightly larger than 1 cm $\times$ 1 cm: active area definition by e-beam lithography and dry etching, ohmic contact definition, deep mesa etching to define a tip close to the active area, and evaporation of a gate to screen electric fields. These steps are described below. After the fabrication steps were completed, the probes were diced by American Precision Dicing, Inc. in San Jose, CA.[3] Before scanning, a probe is manually polished to bring the wafer edge close to the deep mesa tip to minimize sample-probe separation.

[3]GaAs cleaves easily along the crystal axes, so probes can generally be cleaved apart by hand. However, my fabrication was slightly misaligned with the crystal axes and dicing was required to preserve all the probes.

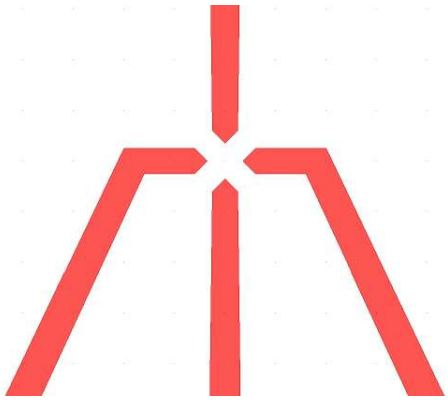

Figure 3.8: Zoom in of Hall probe shallow etch pattern for a 0.5 μm Hall probe.

3.4.1 Active area definition

The first step in the fabrication of the submicron Hall probes is to define the Hall cross. This is done by depleting the 2DEG with a carefully patterned etch. The lithography for this step was done in the SNF with the Hitachi HL-700F e-beam lithography system, followed by a shallow dry etch in the Plasma Quest ECR etcher. The etch does not need to be all the way down to the 2DEG level to deplete the 2DEG. In some structures etching just the GaAs cap can be sufficient to alter the band structure enough to fully deplete the underlying 2DEG. Shallower etches reduce scattering at the boundaries. I aimed for an etch depth of 80–100 nm in this 140 nm deep wafer, as that depth had been tested previously.

The shallow etch pattern (Figure 3.8) was designed for use with a positive resist. The pattern defines where the resist will be exposed and subsequently where the wafer will be etched and the 2DEG depleted. The corners get rounded out somewhat in the exposure and the etching. The 2DEG is also depleted a certain distance laterally beyond the physical etch, referred to as the *depletion width*, which is of order the depth of the 2DEG for a relatively deep etch. The effect of depletion width on a Hall probe is shown schematically in Figure 3.9. A probe is too small and will not work when the depletion regions meet and pinch off the leads to the active area. Since depletion width scales with 2DEG depth, smaller probes are more easily made from shallower 2DEG. (In principle, probes with small effective sizes can be made

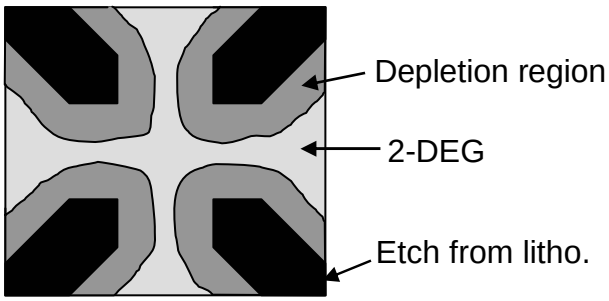

Figure 3.9: Schematic effect of depletion width on a 2DEG Hall cross.

from deep 2DEG, but the design of the shallow etch pattern would need to be highly optimized.)

The linewidths in the pattern (Figure 3.8) defining the active area were scaled with the size of the Hall cross. I made probes with a range of Hall cross sizes (s) of 0.5, 0.7, 1.0 and 2.0 μm on a 1 cm^2 piece of 2DEG wafer. Due to the depletion width, the physical shape of the Hall cross active area in the 2DEG is rounded out and the size is smaller than the lithographic size. A 0.5 μm lithographic probe from this batch has effective geometric size of roughly $s \approx 0.5 - 2(0.140) = 0.22$ μm, where I made the guess that the depletion width equals the 2DEG depth of 140 nm. Farther away from the active area, the etch lines in the pattern widen to ensure development, reaching a width of 5 μm where they extend to the rear of the probe to isolate separate contact areas. A wider tab of 22.5 μm was included at the rear of one line so that a surface profilometer could be used to measure the etch depth.

I used Shipley UV5 resist because it withstands dry etching better than PMMA. I followed this procedure for UV5:

1. Three solvent clean (5 min. sequentially in acetone, methanol, isopropanol).
2. Singe 150°C hot plate 5 min.
3. Poor a few drops of fresh Shipley UV5 resist on the wafer piece.
4. Spin at 6000 RPM for 30 sec.
5. Pre-exposure bake 130°C hot plate 1 min.
6. Expose to e-beam at 10 to 20 μC/cm^2.
7. Post-exposure bake 115°C hot plate 90 sec.

8. Develop in Shipley LDD-26W developer for 45 sec.
9. Hard bake at 145°C hot plate 3 min.

It is important to bake and develop the resist just after the exposure. During the e-beam run for these Hall probes I used 13–16 μC/cm^2 for the largest to smallest Hall cross sizes respectively. Lower exposures were used for the larger linewidths because neighboring regions get partially exposed by the nearby beam due to the proximity effect (Williams 1990, p. 143).

The next step in defining the active area was the etch process on the exposed and developed wafer. First I did an oxygen plasma descum in the Plasma Asher in Ginzton to remove any residual resist left behind in the exposed regions. It was not clear if this was necessary, but it may have helped ensure homogeneous etching. Then I ran the wafers in the SNF Plasma Quest. The process was 15 sccm Ar, 10 sccm BCl_3, and 3 sccm Cl_2, with RF forward power at 35 and reflected power measuring 2.0. I etched for 40 sec. with sample temperature $\sim$23°C which gave an average depth of 85 nm. This process was chosen as a non-selective GaAs/AlGaAs etch.

3.4.2 Ohmic contacts

The next step in the Hall probe fabrication was to put ohmic contacts on the probes which allow electrical connections to be made to the 2DEG. I used a Ni-Au-Ge structure for the metal ohmics. It is believed that the during the anneal of the contacts, Ga atoms diffuse out of the wafer and Ge atoms spike down into the wafer creating electrical connection to the 2DEG. The Ni acts as a wetting layer and can be successfully replaced with Pt (Lin and Lee 1990) in critical applications where no magnetic material can be present.

The four ohmic contact pads per probe were 90 μm $\times$ 1500 μm and can be seen in the left-most picture in Figure 3.7. Their mottled appearance indicates a successful anneal. Optical lithography with a Karl Suss MA-6 Contact Mask Aligner was used to define these large features. The ohmic fabrication process was as follows:

1. Three solvent clean.
2. Singe 150°C hot plate 5 min.

3. Poor a few drops of fresh Shipley 3612 photoresist on the piece.
4. Spin at 3500 RPM for 35 sec.
5. Pre-exposure bake 90°C hot plate 1 min.
6. Remove resist at corners with a pointed Q-tip wet with acetone.
7. Expose on SNF Karl Suss for 1.2 sec. (at 15 mW/cm^2).
8. Develop in Shipley LDD-26W developer for 90 sec.
9. O_2 plasma descum in Ginzton 0.08 min. (Process 5).
10. HF dip just before evaporation, 15 sec. in 20:1 BOE.
11. Evaporate Ni-Au-Ge metal layers.
12. Lift-off in acetone.

The HF dip is done to strip off oxide so that the metal will stick. After the dip I dunked the sample in DI water then blew it dry. Some oxide may reoccur during the quick DI dip, but HF is highly toxic, so I felt it was best to rinse first then blow dry. The metal was evaporated by Tom Carver with an e-beam evaporation system in this order:

Ni	40 Å
Ge	100 Å
Au	100 Å
Ge	60 Å
Au	240 Å
Ni	160 Å
Au	2500 Å

After liftoff the ohmics can be annealed. The anneal was done in the Rapid Thermal Annealer (RTA) in Ginzton. The two parameters temperature and time can be chosen for the anneal and to an extent, increases in either have a similar effect on the outcome. For these Hall probes I had to anneal at a high temperature of 530°C for 40 sec. to get the mottled appearance indicative of a good anneal. This is a significantly higher temperature than I used in earlier fabrications (475°C for 30 sec.) and than is used in the literature (e.g. Lin and Lee 1990). Tests by Yu-Ju Lin and my own tests with dummy GaAs pieces in this RTA around the same time showed that lower temperature readings were not sufficiently annealing the contacts. The RTA may have

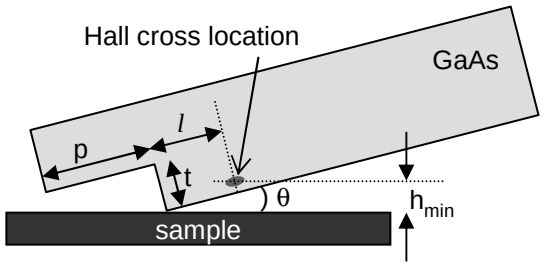

Figure 3.10: Schematic of deep etch of depth t. The GaAs chip is manually polished to a distance p from the mesa tip, close enough so that for all possible alignment angles, θ, the mesa tip and not the chip corner touches the sample. The Hall probe active area is l from the tip. The minimum sample-probe distance $h_{\min}$ is determined by l, θ, and the depth of the 2DEG.

needed recalibration. The appearance of the contacts changes from smooth metal to a bubbly or textured appearance after sufficient annealing. This is presumably caused by the Ga atoms diffusing out of the wafer and through the metal.

The anneal can be done after liftoff, or postponed until after the deep mesa etch. I did it after the deep mesa etch so that the probes were electrically isolated from each other, allowing me to test the contacts immediately after the anneal. The anneal must be done before the gate evaporation so as not to anneal the gate. A simple test of good ohmics is to check that they are not rectifying, or a test pattern can be made to measure any contact resistance (Williams 1990, p. 234–8).

3.4.3 Deep mesa etch

The next step in the fabrication is a deep mesa etch to define the outline of the whole probe. This deep etch is important because it allows the active area to be brought closer to the sample. The mesa edge is close to the active area and defines a tip which will touch the sample surface when properly aligned. A side view sketch of the probe with a deep etch of depth t is shown in Figure 3.10. With a deep etch of several microns, it is then only necessary to mechanically polish the GaAs chip to several tens-of-microns from deep mesa tip, reducing polishing stresses on the probe.

The lithography steps for the deep etch are the same as described for the ohmic

contacts steps 1–8, followed by a 110°C bake on the hot plate for 60 sec. after developing. The wet etch recipe is from DeSalvo et al. (1992) and is a 4:1:10 ratio by volume of a citric acid mix, H_2O_2 (30% concentration), and water. The citric acid mix is a 1:1 mix of anhydrous citric acid and water by weight, or in my case a 1.187:1 mix by weight of citric acid monohydrate and water. The solution's 4:1:10 ratio was chosen for its non-selectivity of GaAs and AlGaAs. Other ratios can be used for a selective etch (DeSalvo et al. 1992). The etch rate is $\sim$0.14 μm/min. The solution etches vertically and laterally at approximately the same rate, so it is important to consider the lateral etching when aligning the deep etch pattern to the Hall probe active area. The depth t should be at least 2 μm. From Figure 3.10 we see that for the tip of the mesa to touch the sample surface, the depth of the etch must be $t > p \tan\theta$. So to not have to polish the wafer closer than $p = 30$ μm, and to be safe for all $\theta \leq 3°$, we need $t > 1.6$ μm.

3.4.4 Screening gate

The final Hall probe fabrication step is to put a metal gate over the active area. Its main purpose is to screen electric fields which can interfere with the magnetic Hall signal, as described above in Section 3.2. The gate is intended to be grounded, although it could also be held at a fixed voltage with respect to the Hall probe in order to alter the carrier density. Possible side benefits of the gate may also be to improve the mechanical robustness of the tip and for use as a scanning tunnelling microscopy (STM) tip.

The gate was designed to overlay several hundred microns of the probe near the tip and to extend out over the deep mesa edge by tens of microns. On the mask, the gate extends out over the deep mesa edge by 20 μm. This distance was chosen to be close enough that the metal would not be polished when manually polishing the probe for scanning, but far enough away to make sure the tip was covered (for STM use if desired) and that any edge wall from the metal evaporation would remain in the deep etched region. The gate can be seen in Figure 3.7.

Gold was chosen for the gate metal, since it is non-magnetic and easy to wire

bond. First, a thin titanium layer was evaporated as a wetting layer to help the gold stick. Tom Carver recommended 5–25 nm for the wetting layer thickness. For the overall thickness, it is desirable to have as thin a gate as possible so as not to add significantly to the minimum scanning height of the Hall probe. However, the gate needs to be thicker than the shallow etch depth (80–100 nm) to ensure continuity.

Shipley Megaposit SPR220-7 positive photoresist was used since it is necessary to entirely cover the probes after the deep mesa etch. I altered the SNF process for 7 μm resist by increasing the spin speed to 6500 RPM, giving 5.2 μm thickness. The metal gate process is as follows:

1. Three solvent clean.
2. Singe 150°C hot plate 5 min.
3. Poor a few drops of fresh Shipley SPR220-7 photoresist on the piece.
4. Spin at 6500 RPM for 45 sec. (accel. 2000 on Laurel spinner).
5. Bake 90°C hot plate for 200 sec.
6. Remove resist at corners with a pointed Q-tip wet with acetone.
7. Over-expose 11.5 ± 3 sec. on SNF Karl Suss (at 15 mW/cm^2).
8. Develop in Shipley LDD-26W developer for 1–2 min.
9. O_2 plasma descum in Ginzton 0.08 min. (Process 5).
10. HF dip just before evaporation, 15 sec. in 20:1 BOE.
11. Evaporate 125 Å titanium followed by 1250 Å gold.
12. Lift-off in acetone.

Tom Carver did the HF dip and evaporation.

For future Hall probe processing, it may make sense to sacrifice the STM ability (which I have never used) by not bringing the gate over the edge of the tip. Then the gate process can be done before the deep etch using a much thinner resist. It is advantageous to have the gate cover only a very small area of the 2DEG around the Hall cross to reduce coupling between the gate and 2DEG, but I did not realize that when I designed my mask.

A concern for gates on shallow 2DEG is leakage between the 2DEG and the gate. For Hall probes made on the 140 nm deep 2DEG, this is not an issue at 4 K. I applied a voltage between the gate and one Hall probe ohmic contact. See Figure 3.11. For

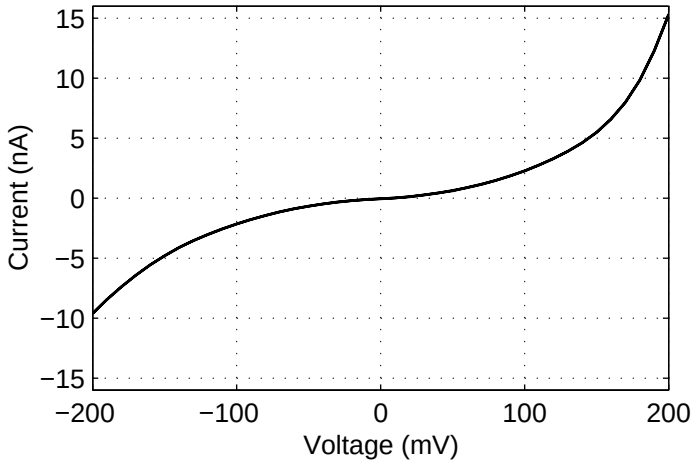

Figure 3.11: Gate leakage to 2DEG at $T = 4$ K. Measured leakage current versus applied voltage between the gate and one of the Hall probe leads of the 0.5 μm probe. In typical operation with a 10 μA bias current, the voltage difference does not exceed 50 mV. The curve was the same for all Hall probe leads.

a voltage difference up to 100 mV, the leakage current was only a few nA. The typical resistance between two Hall probe pads is 10 kΩ at 4 K. Since my gate covers a large area, we can pessimistically assume that the gate covers this entire change of resistance. Then for my typical operation bias current of 10 μA, the maximum potential difference between the 2DEG and the gate will be 50 mV when the gate is grounded and the Hall probe is biased to keep the active area at ground potential. The leakage to the gate is <1 nA or <0.01%. For shallower 2DEG the leakage may be greater, which heightens the importance of making the gate as small as possible so that it is at the same potential as the underlying 2DEG.

3.4.5 Subsequent fabrications

The third generation of scanning Hall probes in the Moler Lab was fabricated by Clifford Hicks in 2002 at the Weizmann Institute. See Figure 3.12. Several improvements were made from the second to third generation. Cliff's probes were made on GaAs/AlGaAs 2DEG grown by Hadas Shtrikman that was only 40 nm deep (Figure

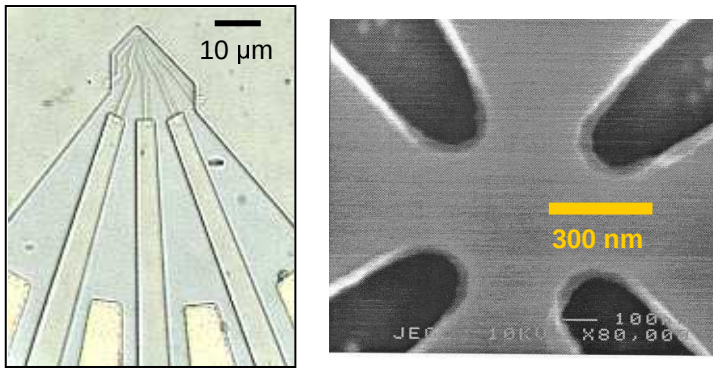

Figure 3.12: Third generation Hall probe fabricated by Clifford Hicks. The probes ranged in Hall cross size from 130 nm to 10 μm. An SEM picture of a 300 nm cross is shown on the right.

3.6). This improvement knocks 100 nm off the minimum sample-probe height compared to the second generation probes. The shallower 2DEG also made it possible to fabricate smaller working Hall probes. Cliff patterned probes ranging in size from 80 nm to 10 μm, however the probes smaller than 130 nm did not work. These third generation probes also had a shallow etch pattern surrounding each probe to gently terminate the 2DEG rather than termination by the deep etch. We thought this might reduce scatterers at the boundaries. Lastly, the gate design covered a much smaller area of the underlying 2DEG. This is advantageous because the 2DEG covered by the gate is then all at approximately the same potential, minimizing leakage currents and capacitive coupling between the 2DEG and gate. The gate step was not completed on these probes though, and they have not been used for scanning.

3.5 Hall probe sensitivity

In the second part of this chapter I will describe noise measurements made on the Hall probes from the second and third generations. Decreasing the Hall probe size is desirable for improving spatial resolution. However, it can also change the noise characteristics. We desired to compare small probes to large probes and also compare probes made on deep (140 nm) and shallow (40 nm) GaAs/AlGaAs 2DEG. The data

showed that while field noise does increase with decreasing Hall probe size, flux noise improves with smaller probe size down to the smallest probe of 130 nm.

3.5.1 Noise sources in 2DEG Hall probes

Ideally, the Hall voltage is related to the current and magnetic field by the expression $V_{xy} = R_H IB$. However, in reality there are other contributions to V_{xy}. In the time domain the measured voltage is more accurately expressed as

$$V_{xy}(t) = I(R_H B + R_{\text{offset}} + R_{\text{noise}}) + V_{\text{preamp}} + V_{\text{Johnson}}. \tag{3.3}$$

The signal-to-noise ratio in the frequency domain is

$$SNR = \frac{IR_H B}{\sqrt{(IR_{\text{noise}})^2 + V_{\text{preamp}}^2 + V_{\text{Johnson}}^2}}. \tag{3.4}$$

R_{offset} is quasi-ohmic and is thought to be the result of imperfect symmetry of the lithographically defined Hall cross or of the 2DEG itself. Typically $R_{\text{offset}} \lesssim 50\ \Omega$. R_{noise} is a resistive noise that may be due to fluctuations in the 2D carrier density or the mobility. V_{preamp} is white noise of 4 nV/$\sqrt{\text{Hz}}$ above 10 Hz, and V_{Johnson} is from the voltage leads of the resistor and has magnitude $\sim$1.5 nV/$\sqrt{\text{Hz}}$ for a typical $R = 10\ \text{k}\Omega$ submicron Hall probe at 4 Kelvin.

A point worth emphasizing is that our main source of Hall probe noise is *resistive* noise. As Equation (3.4) shows, the bias current I of the Hall probe can be increased to overcome the preamplifier and Johnson voltage noise. But once I is large enough that IR_{noise} is the dominant voltage noise, increasing the current does not help. In fact, at high currents R_{noise} becomes non-ohmic and increases with I. I^2R heating also places a constraint on I and thus it is desirable from that standpoint, as well as for reducing Johnson noise, to have a low resistance R for the leads to the Hall cross. Careful design of the probe to minimize the number of "squares" and choice of a material with high mobility μ help to minimize R. There is an optimal current (or range of currents) that minimize the SNR for a given frequency. Not surprisingly, we found that this optimal current is larger for larger probes.

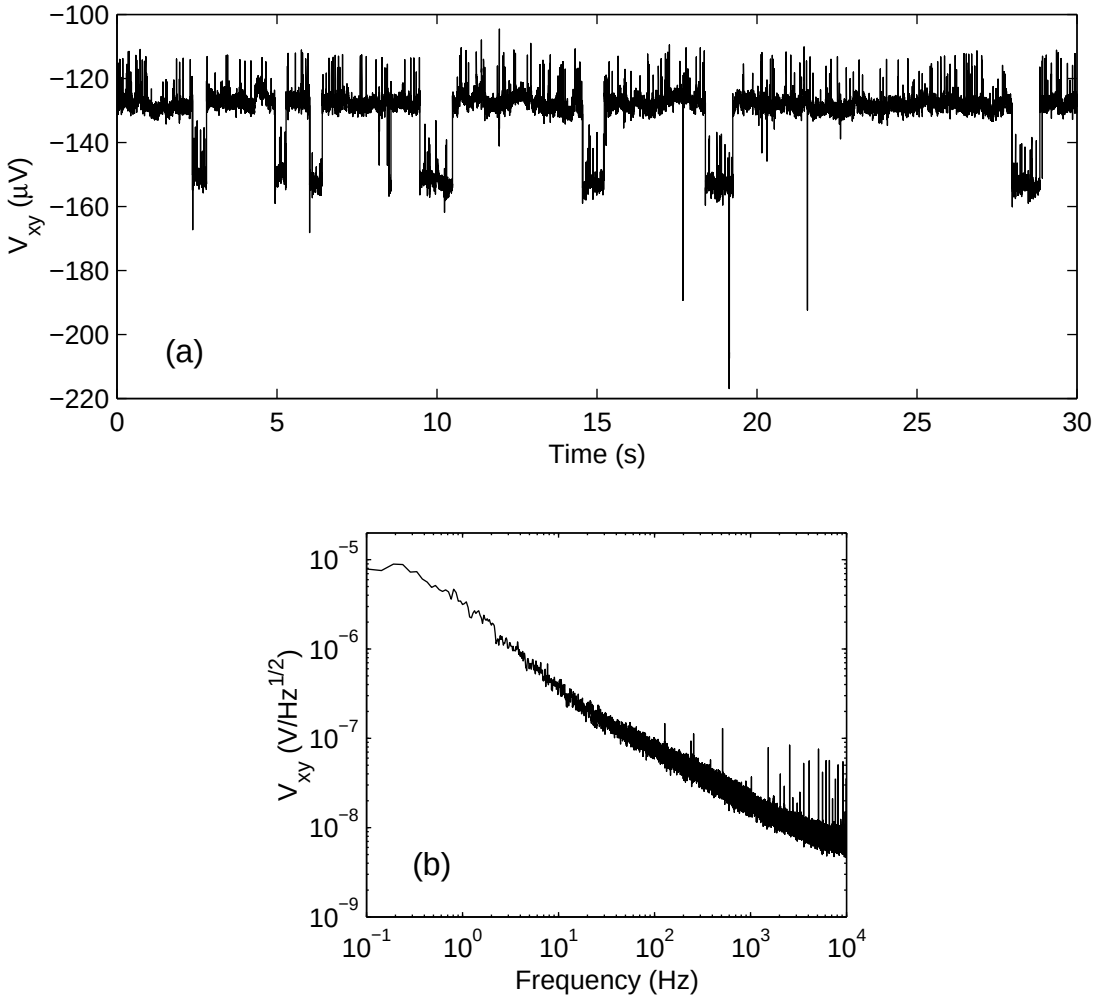

Figure 3.13: Telegraph noise in a 130 nm Hall probe with $I_{\rm bias} = 3$ μA. (a) Time trace. Two switching events with ΔV_{xy} approximately 26 μV and 15 μV are dominant and have different frequencies. (b) FFT of the time trace data. The flattening at low frequency is the Lorentzian of the biggest switcher.

The resistive noise manifests itself in the submicron Hall probes as telegraph noise in $V_{xy}(t)$. Figure 3.13 shows a time trace (a) for the smallest Hall probe (130 nm) in zero field, and the Fourier transform (b) of the time trace. Two "switchers" can be seen that cause telegraph noise. Telegraph noise from a single switcher is a Lorentzian in frequency space. If there are many switchers it becomes $1/f$-like in frequency space (Kurdak et al. 1997). It is suspected that the telegraph noise is caused by changes

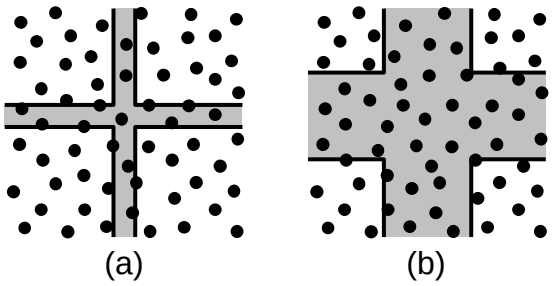

Figure 3.14: Schematic of switchers (dots) vs. Hall probe size. The Hall cross active area of the small probe in (a) has only one switcher above it and would exhibit telegraph noise, while the large probe in (b) has many switchers above the active area which would combine to give 1/f-like noise.

in the remote impurity or dopant configuration. One impurity or dopant changing between two states or positions would constitute one switcher. This is consistent with our observation of telegraph noise in small Hall probes and $1/f$-like noise in larger probes, as illustrated by the schematic in Figure 3.14.

The switching states can vary from cooldown to cooldown. Electrical shocks or physical trauma to the Hall probe can also greatly increase $R_{\rm noise}$. The probe recovers from this increased noise with cycling the temperature (typically to room temperature, although I have seen improvement after cycling only to 100 K). Exposing the probe to optical photons can also help recover the minimum noise state, presumably by releasing trapped photo-induced carriers. To avoid unnecessary shocks, the Hall probe is completely hooked up to the electronics whenever possible before it is cooled. The time trace for the 130 nm probe shown in Figure 3.13(a) was after the probe was inadvertently shocked, so its telegraph steps are large.

3.5.2 Measurements of Hall probe noise spectra

To characterize the Hall probe noise we took extensive noise spectra on five different Hall probes ranging in size from 130 nm to 10 μm. Four of the five probes were the third generation probes, while the 0.5 μm probe was from the second generation. Basic properties of the two 2DEG wafers were given in Table 3.1. The details of each

Table 3.2: Summary of Hall probe noise tests ($T \approx 4$ K).

size (μm)	which 2DEG	best $I_{\rm bias}$ (μA)	field noise at 1 Hz (G/$\sqrt{\rm Hz}$)	corner freq (Hz)	measure location	measured by whom
0.13	WIS	2	0.5	10^4	dip probe	Guikema
0.39	WIS	4	0.4	10^3	fridge	Björnsson
0.5	IBM	24	0.03	100	SXM	Guikema
1	WIS	15	0.01	500	dip probe	Gardner
10	WIS	200	0.002	10^4	fridge	Björnsson

probe studied are shown in Table 3.2.

We biased the Hall probes with a DC current sourced from a battery box in series with a large resistor. It is advantageous to have a large battery voltage and a large series resistance, because that minimized the effect of uncertainties or fluctuations in the Hall probe resistance on the bias current. Large voltage with a large resistor also minimizes shot noise in the Hall probe, though shot noise is not a significant noise source here. The 0.5 μm probe was the only probe with a gate, so for that probe the bias current was supplied from balanced +6 and −6 V sources through equal large variable resistances and the gate was grounded. This kept the Hall cross active area and the gate at the same voltage, ignoring from any difference between the Hall probe lead resistances, which would contribute a few mV. It is important to keep the probe and gate at the same voltage because if the potential difference is too large, leakage will occur (see Figure 3.11).

The Hall voltage V_{xy} was first sent to a small home-built preamplifier[4] with a fixed gain of 210 at the top of the cryostat or dewar. It was amplified again with a SRS560 preamplifier, then sent to a analog-digital converter. Time traces and fast-Fourier-transform (FFT) spectra were recorded with a MABLAB® program written by Mark Topinka (with revisions by Per Björnsson).

We wanted to measure the best field noise density and flux noise density for each

[4]The home-built amplifier was a standard 3-op-amp instrumentation amplifier from Horowitz and Hill (1989, p. 425). $R_1 = 100$, $R_2 = 1$K, the two center $R = 100$, and the two rightmost $R = 1$K. Gives gain of 210.

probe at both low and high frequencies. The Hall voltage V_{xy} spectra were measured for a range of bias currents. From this the resistive noise density $R_{xy} = V_{xy}/I_{\rm bias}$ was determined for each current value. This was converted to magnetic field noise density by $B = R_{xy}/R_{\rm H}$, where $R_{\rm H}$ is the measured Hall coefficient for each probe. Typically $R_H \approx 0.12\ \Omega$/G for the IBM 2DEG probes and $R_H \approx 0.15\ \Omega$/G for the larger WIS 2DEG probes, though the smallest probe of 130 nm had an enhanced $R_H \approx 0.20\ \Omega$/G. For studying small magnetic features, flux noise and not field noise is the sensitivity we care about. Thus finally the noise spectra is converted to flux noise density $\Phi_B = B\, s^2$, where s is the size of the Hall probe. As mentioned earlier, the effective size of the Hall probe is smaller than the lithographic size s due to 2DEG depletion. It is not straightforward to determine the true size of the probe, so I have conservatively taken $s \times s$ as the probe area, which overestimates the flux noise somewhat.

The spectra were recorded for a range of currents to determine the optimal bias current for each probe. Figure 3.15 shows V_{xy} and R_{xy} noise densities for the 1 μm probe. From the R_{xy} spectra it is clear that $I_{\rm bias} \approx 15\ \mu$A is the optimal current for low frequencies. Low frequency noise is of interest because the Hall probe images are taken at 10 ms/pixel or slower (typically 64^2 or 96^2 pixels per image), or 1–3 minutes per image. Figure 3.16 shows spectra for the 0.5 μm probe for $I_{\rm bias}$ ranging from 0 to 42 μA. The R_{xy} spectra (not shown) reveals that $I_{\rm bias} = 24\ \mu$V is ideal at low frequencies. However, measurements of the Hall coefficient for this 0.5 μm probe showed that $R_{\rm H}$ dropped when $I_{\rm bias}$ exceeded $\sim$12 μA (see Figure 3.17). This was surprising and was not observed for any of the other probes, indicating that it was likely an effect of the gate. Therefore whenever this probe was used for scanning, I did not exceed 10 μA.

One point worth mentioning is that we saw no dependence of the noise on magnetic field up to 600 G, which is well within the field range of interest. Therefore no noise term for field dependence was included in Equations (3.3) and (3.4).

Figure 3.18 shows the best voltage, resistive, field and flux noise spectra for each of the five Hall probes. The curves are for the optimal currents, chosen because they minimized the field noise at low frequencies. In general the smaller the probe, the

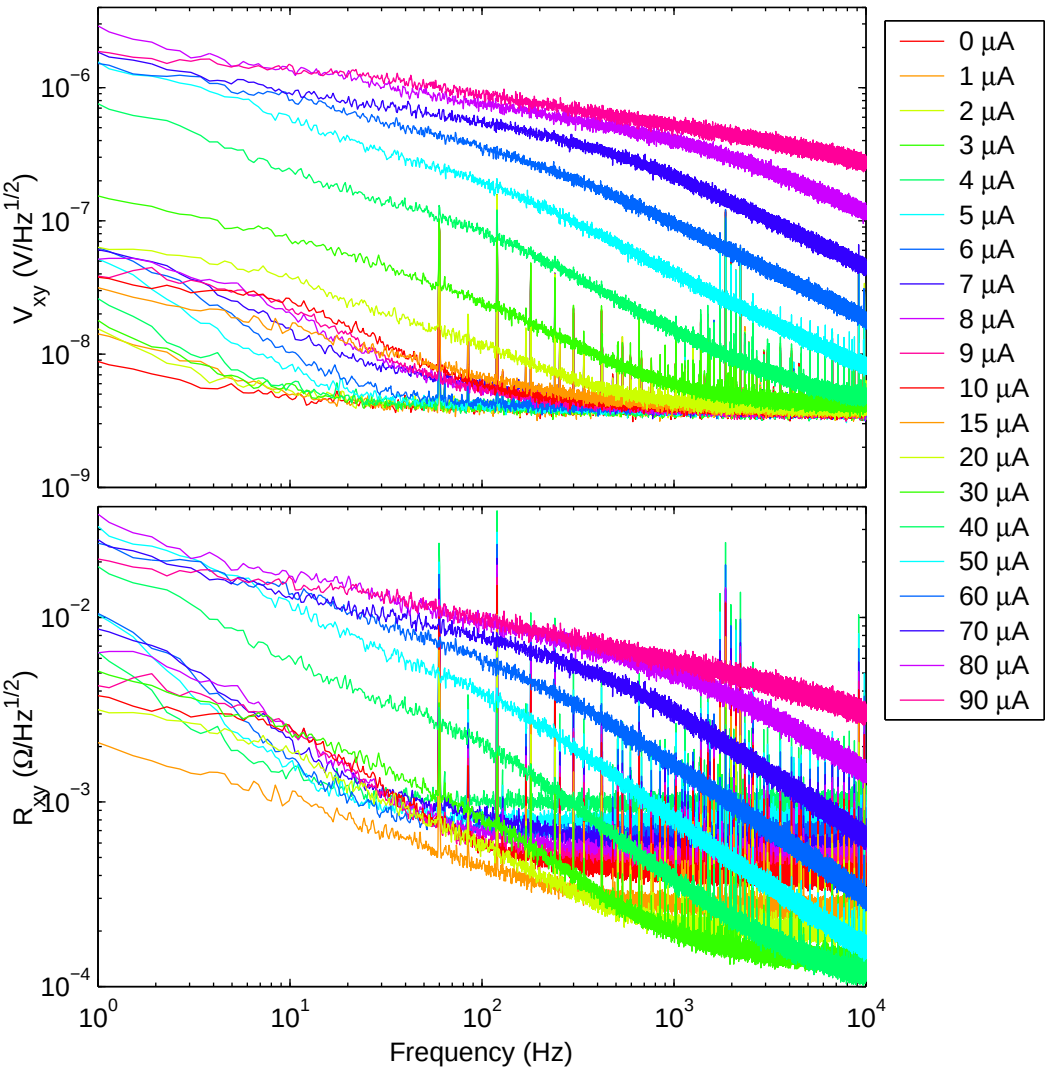

Figure 3.15: V_{xy} and R_{xy} noise spectra for the 1 μm Hall probe at $T \approx 4$ K. Data taken by Brian Gardner.

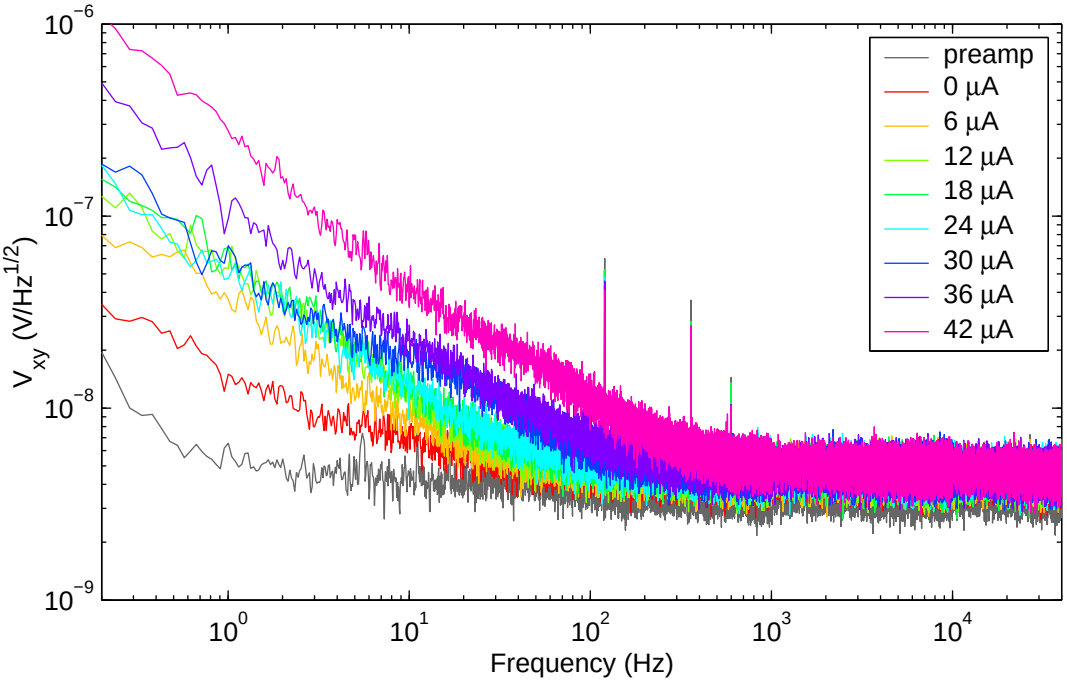

Figure 3.16: V_{xy} noise spectra for the 0.5 μm Hall probe.

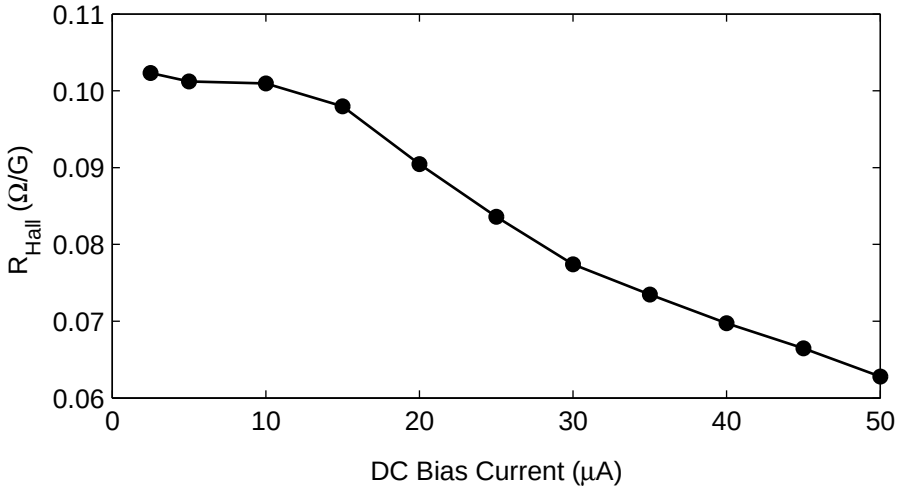

Figure 3.17: Current dependence of the measured Hall coefficient (R_H) of the gated 0.5 μm probe.

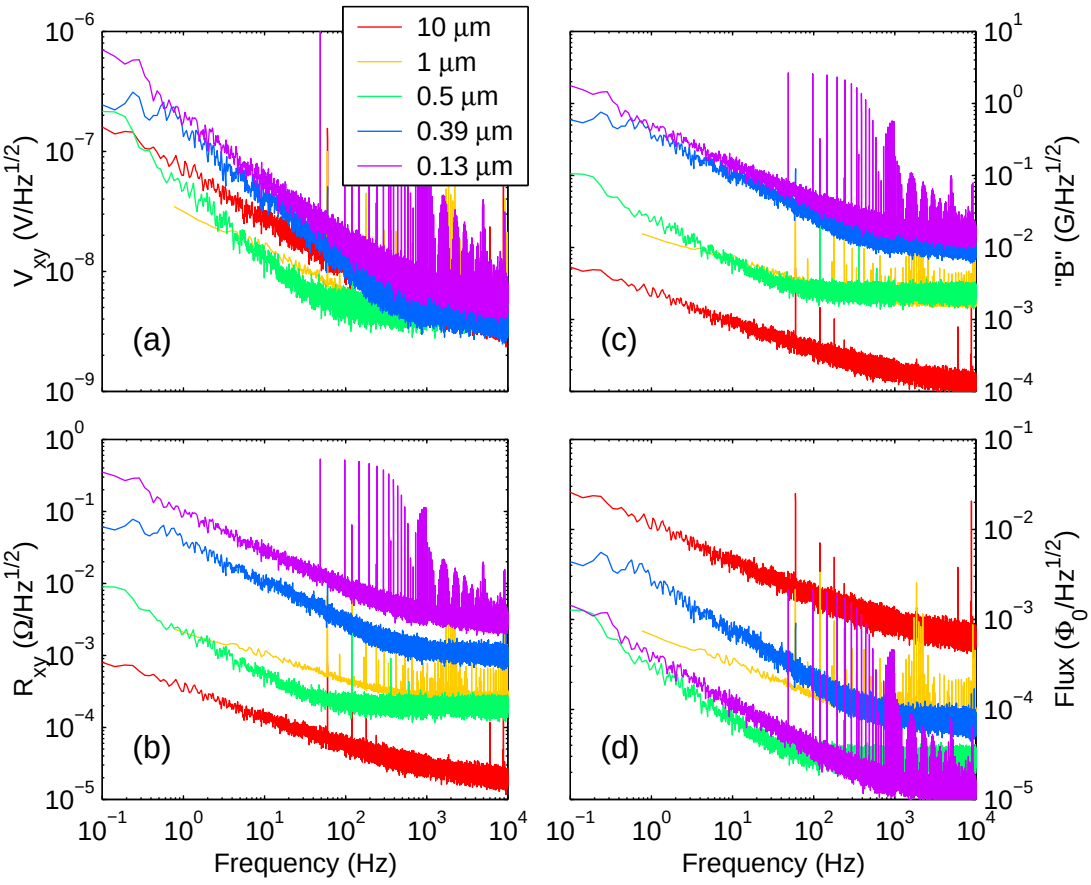

Figure 3.18: Best noise spectra for five Hall probes. The bias currents were (from largest to smallest probe): 200, 15, 24, 4, and 2 μA.

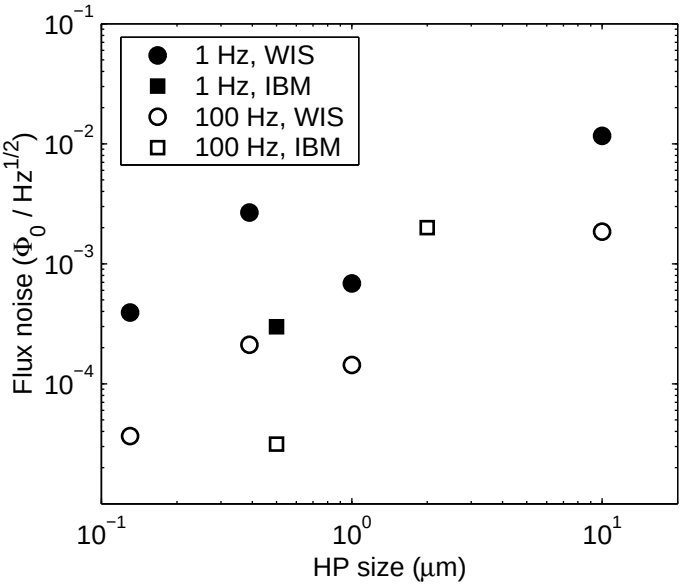

Figure 3.19: Flux noise vs. Hall probe size at 1 Hz and 100 Hz.

smaller the optimal current (Table 3.2). However, the 0.5 μm probe fabricated on the deeper IBM 2DEG had a higher optimal current than the 1 μm probe made from the shallower WIS 2DEG. Figure 3.18(c) shows that generally the larger probes do have lower noise in magnetic field units, but Figure 3.18(d) shows that the flux noise generally decreases as probe size shrinks. This is summarized in Figure 3.19 which shows the flux noise at 1 Hz and at 100 Hz for each probe. We have not reached a limit in flux noise by going to smaller Hall probes, the smaller probes are better.

The data on the 0.5 μm probe fabricated on the 140 nm deep IBM 2DEG suggest that this is a slightly quieter 2DEG than the 40 nm deep WIS heterostructure. However, more wafers would need to be studied to determine if this is just due to random variations in 2DEG growth or if shallower depth increases the noise. The noise is not substantially worse for the WIS structure, which makes that structure more desirable due to the shallower depth and thus the ability to make smaller Hall probes.

We expect that we could fabricate a 100 nm Hall probe in GaAs/AlGaAs by further optimizing the Hall cross lithographic shape. Mark Topinka, Hendrik Bluhm, and Jenn Cho have been working recently on fabricating smaller Hall probes.

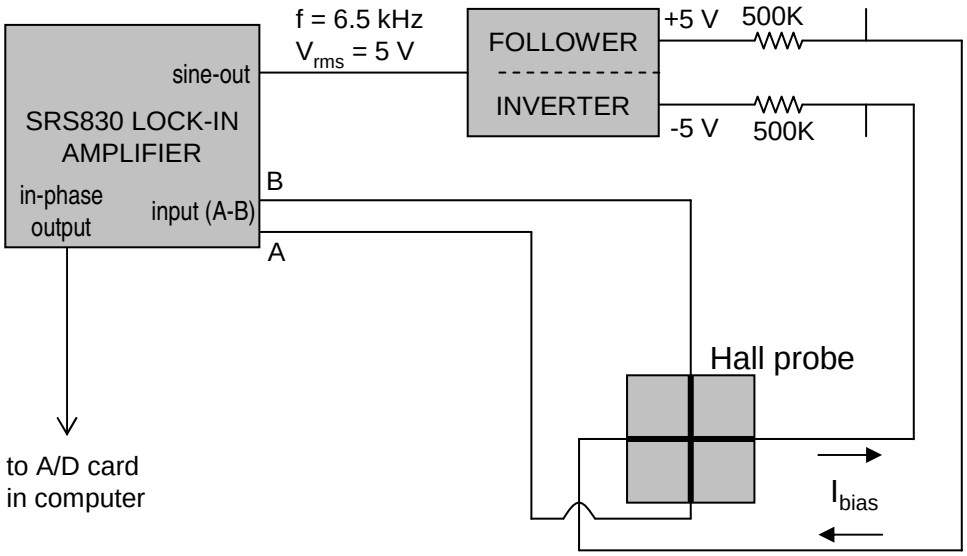

Figure 3.20: Diagram of the Hall probe electronics. The grounded gate of the Hall probe is not shown. The tees to the right of the 500K resistors allow the Hall probe to be grounded with BNC shorting caps.

3.6 Hall probe electronics for scanning

During my research, I found that the optimal way to drive the Hall probe for scanning in the SXM was with an AC current ∼6.5 kHz and lock-in detection, averaging 10–50 images together to filter out low frequency Hall probe noise. The number of averages needed for a good image depended on the signal strength and the noise characteristics of the probe. A diagram of the Hall probe electronics is shown in Figure 3.20.

Using an AC current to bias the Hall probe is advantageous because with lock-in detection we eliminate many extrinsic noise sources. The 6.5 kHz frequency was chosen because above that, capacitive coupling of the leads became significant. However, this lock-in technique does *not* take care of the low frequency telegraph or $1/f$-like resistive noise. To minimize this effect on the images, scans are taken as quickly as possible and averaged together. With $f \approx 6.5$ kHz, the fastest time constant that seemed reasonable was $\tau = 1$ ms on the lock-in, with the 24 dB rolloff setting. The wait time with the full 24 dB rolloff is 10τ, so the scan speed was set for 10 ms/pixel.

Images can be acquired faster than this for diagnostic purposes or locating features of interest. The lowest resonant frequencies of the S-bender scanner are $\sim$40 Hz, so this scan speed of $<$2 Hz per line is certainly safe.

Chapter 4

Tests for spin-charge separation

Despite intense effort over the last 18 years, agreement on the mechanism of superconductivity in the cuprates has not been reached. Many theories of cuprate superconductivity make their sharpest predictions for very underdoped samples, where the superfluid density is lowest (see the cuprate phase diagram in Figure 4.1(a)). One promising class of such theories is superconductivity mediated by spin-charge separation (SCS). Recently a quantitative microscopic SCS theory was formulated by Senthil and Fisher (2000). This chapter discusses two experimental tests that we performed to test their theory (Wynn et al. 2001; Bonn et al. 2001). Both tests gave null results, limiting the applicability of SCS in the cuprates.

4.1 Spin-charge separation and visons

Spin-charge separation is an appealing theory for the high-temperature superconductors because it can explain some of the unusual properties of the pseudogap and the high transition temperatures. Anderson (1987) first proposed SCS for the cuprates in his resonating valence bond state. In SCS the electron *fractionalizes* into a chargeless spin 1/2 fermion (called a *spinon*) and a spin-less charge e boson (called a *holon* or *chargon*). SCS has been experimentally observed in one-dimensional systems, but thus far has only been proposed theoretically in two-dimensions, and evidence for it in the cuprate superconductors is indirect.

In conventional superconductivity, electrons form Cooper pairs (charge $2e$ bosons)

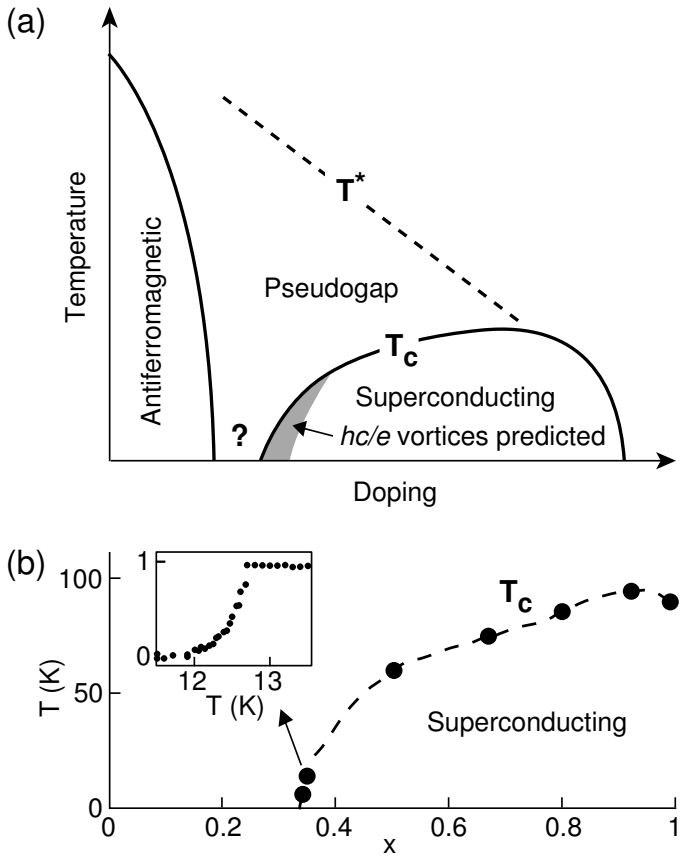

Figure 4.1: (a) Schematic temperature-doping phase diagram of the cuprate superconductors. The question mark indicates a poorly understood region. Samples with doping below that which gives the maximum T_c are called *underdoped*. The shaded area qualitatively indicates where hc/e vortices are predicted in theories of spin-charge separation (Sachdev 1992; Nagaosa and Lee 1992; Nagaosa 1994; Senthil and Fisher 2001a). (b) T_c as a function of oxygen content in $YBa_2Cu_3O_{6+x}$ crystals (Liang et al. 1998, 2002). Inset: Magnetic transition of a $YBa_2Cu_3O_{6.35}$ crystal measured locally with a Hall probe in an applied AC field of 0.06 mT. Vertical axis is the magnetic field measured by the Hall probe normalized by the applied field.

which condense to the superconducting state. In SCS superconductivity, the chargons could directly Bose condense without the need for pairing. Naively, hc/e flux quantization would be expected from SCS superconductivity, because a charge e particle circling an hc/e vortex acquires a 2π phase shift. This would be in contrast to the conventional $hc/2e$ superconducting flux quantum, which have also been observed in cuprates (Gough et al. 1987). (See Sections 1.2.1 and 6.1 for details on fluxoid quantization.) SCS theories do in fact allow $hc/2e$ vortices (Kivelson et al. 1988), but it has long been recognized that SCS may lead to hc/e vortices, specifically in samples with low superfluid density and a high energy scale for SCS (Sachdev 1992; Nagaosa and Lee 1992; Nagaosa 1994; Senthil and Fisher 2001a). Senthil and Fisher (2000) introduced an excitation called a *vison* (vortex in a Z_2 gauge) which provides a π phase shift to a circling chargon, thereby enabling $hc/2e$ vortices at an energy cost of $E_{\text{vison}} \approx k_B T^*$, where T^* is the pseudogap temperature (Senthil and Fisher 2001a). The balance of superfluid energy, vortex core energy, and vison energy determines whether hc/e or $hc/2e$ vortices are preferred.

The first experiment discussed below (Section 4.2), published as Wynn et al. (2001), looked for hc/e vortices in very underdoped crystals of $YBa_2Cu_3O_{6+x}$ with very low transition temperatures $T_c \sim 12$ K. The choice of samples was important, as hc/e vortices have been predicted only for low superfluid density. In particular, Senthil and Fisher (2001a) predict the energy of an hc/e vortex to be less than the energy of two $hc/2e$ vortices at $T = 0$ when $7\pi T_c < T^*$, with increasing preference for hc/e as $T \to T_c$. No hc/e vortices were observed in our scanning magnetic images. This set an upper limit on the vison energy much lower than predicted by the theory.

It is conceivable that the lack of hc/e vortices was due to metastable $hc/2e$ vortices, so we performed an experiment proposed by Senthil and Fisher (2001b) which addresses the dynamics of visons and is thus a more stringent test of the theory (Section 4.3 and published as Bonn et al. (2001)). This experiment looks for the signature of a vison trapped in a superconducting ring. The ring is prepared with (without) a vison in the hole by first trapping an odd (even) number flux quanta in the hole and then warming just above T_c to let the flux escape. If a vison is present in the hole when the ring is recooled below T_c, an $hc/2e$ vortex must be generated, even when

cooled in zero field. In this way the ring exhibits "memory" of the initial state of the ring (odd or even flux). Visons would be more readily trapped in samples with low T_c, and thus we performed this experiment on the very underdoped $YBa_2Cu_3O_{6+x}$ crystals fabricated in a ring geometry. No evidence for visons was seen, setting a stringent limit on the vison energy that – like the limit from the null hc/e results – was much lower than the theoretically predicted $E_{\rm vison} \approx k_B T^*$.

It should be remarked that the meaning of SCS and the generality of the Senthil-Fisher approach have been under debate (Moessner et al. 2002), since some forms of SCS do not require visons. But our experiments deem unlikely at least one group (Senthil and Fisher 2000; Franz and Tešanović 2001; Sedgewick et al. 2002) of theories that predict visons and/or a vortex memory effect in the cuprates.

4.2 The hc/e search[1]

A key feature of superconductivity is magnetic flux quantization. Experimentally, flux is found to be quantized in units of $hc/2e$ in both conventional superconductors (Deaver and Fairbank 1961) and near-optimally doped cuprates (Gough et al. 1987), but flux quantization in high quality samples of the cuprate superconductor $YBa_2Cu_3O_{6+x}$ (YBCO) in the very underdoped region has not been previously studied.

We report magnetic imaging experiments on four single crystals of $YBa_2Cu_3O_{6.35}$ with critical temperatures (T_c) of 11–13 K. This work was motivated by the general importance of flux quantization, and by specific scenarios in which superconductivity results from spin-charge separation. As discussed above in Section 4.1, SCS predicts energetically favorable hc/e vortices for very underdoped cuprates, with increasing preference near T_c.

Over 170 vortices were imaged in the $YBa_2Cu_3O_{6.35}$ samples with scanning Superconducting QUantum Interference Device (SQUID) microscopy and scanning Hall probe microscopy, both of which measure magnetic flux quantitatively. The Hall probe measurements are somewhat noisier but cover a wider temperature range and

[1]This hc/e experiment was published as Wynn et al. (2001).

have higher spatial resolution. All the observed vortices carried a single conventional flux quantum, $hc/2e$, within experimental error. These results set a semi-quantitative upper limit on the energy scale for SCS which is much lower than predicted.

4.2.1 YBCO samples

Our low-T_c samples of $YBa_2Cu_3O_{6+x}$ are the product of recent improvements in crystalline perfection with the use of $BaZrO_3$ crucibles for crystal growth (Liang et al. 1998, 2002). Figure 4.1(b) shows T_c as a function of the oxygen content that sets the doping in these high purity crystals. The lowest T_c's are found around $x = 0.35$, produced by annealing crystals at 900°C in flowing oxygen. After this first anneal the crystals were sealed in a quartz ampoule, together with pieces of $YBa_2Cu_3O_{6.35}$ ceramic, and heated to 580°C to homogenize the oxygen content. After quenching to room temperature, these samples are not superconducting, but annealing near room temperature for a few weeks (Veal et al. 1990) allows the intercalated oxygen to order into CuO chains (Liang et al. 2002), producing samples with $T_c \approx 12$ K and $\Delta T_c \lesssim 2$ K (Figure 4.1(b) inset). The platelet-shaped crystals were 10–100 μm thick along the c-axis and about 1 mm × 1 mm with the ab-plane parallel to the surface (Liang et al. 1998, 2002). These crystals were described in more detail in Section 1.3.

4.2.2 SQUID data and fits

Over 110 vortices in three single crystals of $YBa_2Cu_3O_{6.35}$ were studied with the scanning SQUID in the temperature range 2–7 K. The microscope and Nb SQUID have been described elsewhere (Gardner et al. 2001). The SQUID's 8 μm square pickup loop is aligned parallel to the sample surface at a height $z \approx 1.5$ μm. For comparison, vortices in crystals with $x = 0.50$ ($T_c \approx 60$ K) were also imaged. The apparent shape of the vortices is due primarily to the shape of the pickup loop (Figure 4.2(a)).

The total flux carried by vortices in the SQUID images was determined by integration and fits. Integrating the signal from isolated vortices over a relatively large area of 1000 μm^2 yielded flux $\Phi = 0.9 \pm 0.2$ $hc/2e$. The quoted errors include conservative

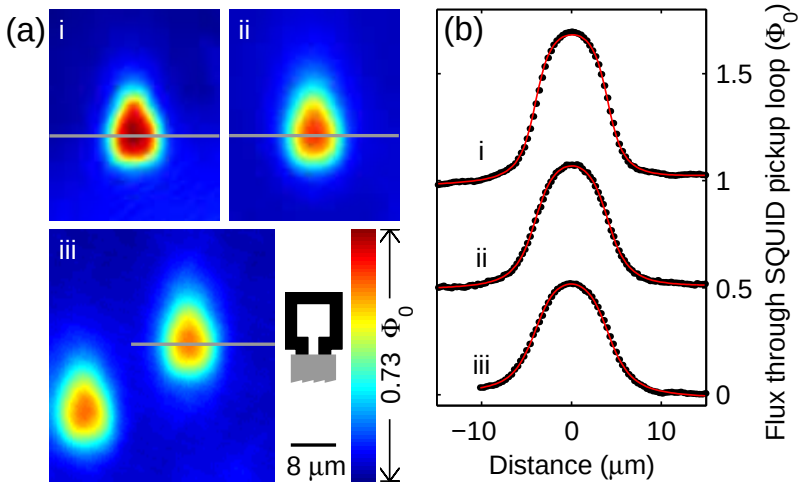

Figure 4.2: (a) Scanning SQUID microscopy of vortices in high purity $YBa_2Cu_3O_{6+x}$ crystals. (i) At $T = 3.4$ K in an $x = 0.50$ ($T_c \approx 60$ K) crystal; (ii) at 2.1 K, and (iii) at 6.3 K in an $x = 0.35$ ($T_c \approx 12$ K) crystal. The color-scale corresponds to the flux through the SQUID pickup loop in units of $\Phi_0 = hc/2e$. The teardrop shape is due to the shielded leads of the pickup loop. Inset: Sketch of the SQUID pickup loop drawn to the same scale. (b) Data (points) with fits (red lines) from image cross-sections corresponding to the gray lines in (a), offset by 0.5 Φ_0 for clarity. The model is discussed in the text. Images in (a) and cross-sections in (b) are displayed with a constant background subtracted. The fits gave (i) $z + \lambda_{ab} = 1.5 \pm 0.2$ μm and $\Phi = 1.00 \pm 0.07$ Φ_0, (ii) 2.0 ± 0.2 μm and 0.96 ± 0.07 Φ_0, and (iii) 2.3 ± 0.2 μm and 0.97 ± 0.07 Φ_0.

estimates of uncertainties in the effective SQUID pickup loop area, the distance calibration of the scanner, and the background determination. Throughout this Section 4.2, flux values rounded to the nearest tenth are representative of the analysis of numerous vortices. The total flux was also determined by fitting a model of the vortex magnetic field. Consider a vortex in a half-infinite sample oriented along the c-axis in the limit $\sqrt{r^2+z^2} \gg \lambda_{ab}$, where $\vec{r} = (x, y)$ is the distance from the vortex center, z is the height above the sample surface, and λ_{ab} is the in-plane penetration depth. The field is closely approximated by a monopole (Pearl 1966; Chang et al. 1992)

$$B_z(r,z) = \frac{\Phi}{2\pi} \frac{z+\lambda_{ab}}{[r^2+(z+\lambda_{ab})^2]^{3/2}}, \tag{4.1}$$

where $B_z(r,z)$ is the magnetic field perpendicular to the surface of the sample and Φ is the total flux of the vortex. For our very underdoped YBCO measurements, the limit $\sqrt{r^2+z^2} \gg \lambda_{ab}$ is not strictly valid for small r, but comparison to a full model (given in Appendix A) indicates that the approximation remains acceptable.[2] The measured signal is the total magnetic flux through the SQUID pickup loop, treated as a perfect 8 μm $\times$ 8 μm square for fitting. Cross-sections through the vortex center were fit with free parameters $(z+\lambda_{ab})$, total flux Φ, and a linear background. See examples in Figure 4.2(b). The fits consistently gave $\Phi = 1.0 \pm 0.1\ hc/2e$ for vortices in the $x = 0.35$ and $x = 0.50$ crystals.

4.2.3 Hall probe data and fits

We also made scanning Hall probe (Chang et al. 1992) images of vortices in a crystal of $YBa_2Cu_3O_{6.35}$ with an onset T_c of 12.7 K (Figure 4.1(b) inset), and for comparison and calibration, in a $YBa_2Cu_3O_{6.95}$ crystal with $T_c = 92$ K. Figure 4.3 shows images at 4.2 K after cooling in magnetic fields chosen to give desirable vortex densities in each crystal. Vortex images from the $x = 0.95$ crystal (Figure 4.3(a))

[2]The calculated field B_z for $r = 0$ and $z = \lambda_{ab}$ is only 16% greater for the monopole model compared to the full model. This error will be less for our SQUID images, since they are a convolution of the 8×8 μm^2 pickup loop with the vortex field.

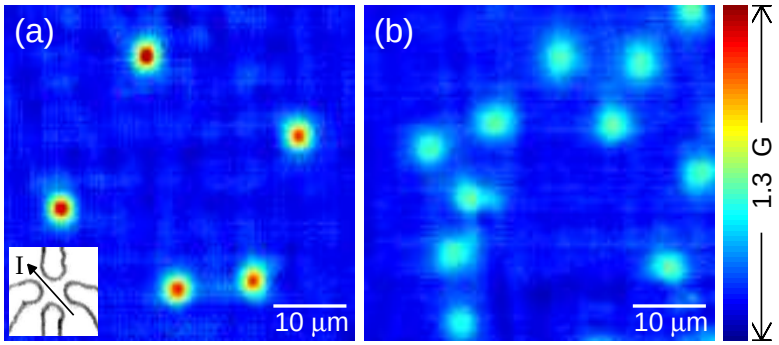

Figure 4.3: Scanning Hall probe images of $hc/2e$ vortices in $YBa_2Cu_3O_{6+x}$ crystals at 4.2 K with line by line background subtraction. (a) In a nearly optimally doped sample with $x = 0.95$ and $T_c = 92$ K. Inset: The Hall probe at the same scale, with the direction of the AC current (I) as shown. (b) In a very underdoped sample with $x = 0.35$ and $T_c = 12.7$ K. The density of vortices was determined by the applied field when cooled. Note the lower peaks and wider profiles of the vortices in (b) compared to (a).

appear to be resolution-limited, consistent with the known low temperature penetration depth in similar near-optimally doped samples, $\lambda_{ab} \approx 0.16$ μm (Basov et al. 1995). Fits to the vortex images in that sample were therefore used to characterize the size and shape of the nominally 2 μm $\times$ 2 μm Hall probe (shown in Figure 4.3(a) inset). The images in Figure 4.3 were obtained on adjacent, aligned, flat samples in an attempt to have a constant $z \approx 1$ μm.

Although the Hall probe measurement had more background and less field sensitivity than the SQUID measurement (making averaging necessary), the Hall probe was crucial for a thorough survey of vortices in the very underdoped samples, since hc/e vortices should be most stable close to T_c (Sachdev 1992; Nagaosa and Lee 1992; Nagaosa 1994; Senthil and Fisher 2001a), as schematically shown in Figure 4.1(a). We imaged vortices formed after cooling just below the $T_c = 12.7$ K of the $YBa_2Cu_3O_{6.35}$ sample. This addressed a scenario in which energetically favored hc/e vortices might not form if $hc/2e$ vortices, which repel each other, were already present. Often we continued cooling and imaged the vortices for T as low as 3 K, and then warmed and imaged again just below T_c. The vortex locations did not change with this temperature cycling below T_c, indicating that vortices neither split nor condensed, and thus

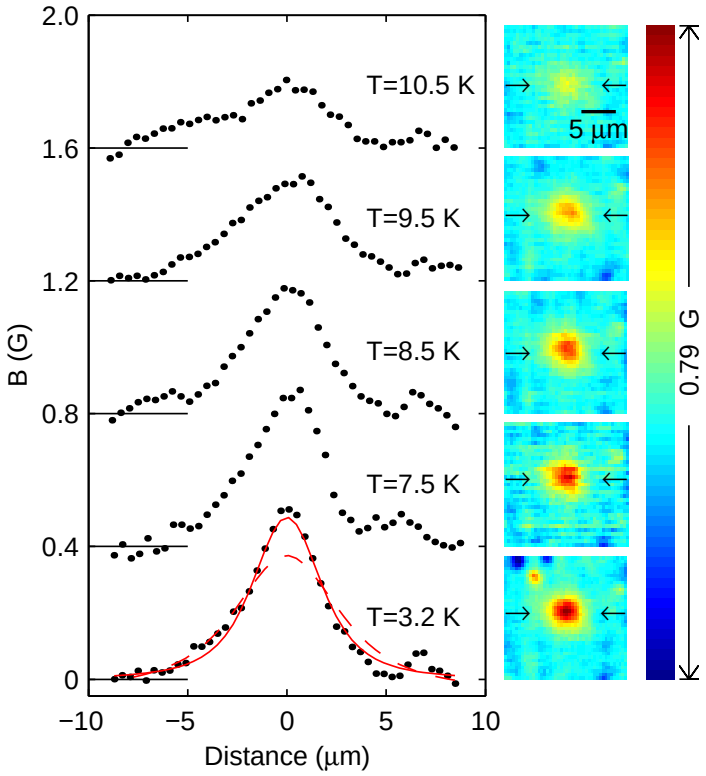

Figure 4.4: Hall probe images of a vortex in $YBa_2Cu_3O_{6.35}$ while cooling below $T_c = 12.7$ K. Linear fitted backgrounds have been subtracted. The bright and dark spots in the upper left of the 3.2 K image and elsewhere are understood as the Hall probe interacting with the electric field of charges on the sample surface (discussed in Section 3.2). Cross-sections, as indicated by the arrows, are shown offset by 0.04 mT for clarity. The full-width half-maximum decreases from 5.3 ± 0.3 μm at 10.5 K to 4.0 ± 0.3 μm at 3.2 K. The red lines are from 2D fits to the vortex with Φ set at $hc/2e$ (solid) and hc/e (dashed).

that each carried an unchanging amount of flux at low temperatures up to at least 11 K, where we had insufficient sensitivity to resolve the vortices. One such cooling cycle is shown in Figure 4.4. When cycled above T_c to 15 K and back down, vortices sometimes but not always formed at the same locations.

The $hc/2e$ flux quantization was best established by the SQUID measurements, supplemented by the Hall probe to study temperature dependence. For consistency, we also used integration and fits to determine Φ of vortices in the Hall probe images. The integration had a large error associated with the vortex signal dropping into the

noise quickly, potentially losing tenths of a flux quantum. Single vortex integration gave $\Phi = 0.7$ to 0.9 $hc/2e$ in the near-optimally doped sample, where vortices are known to be $hc/2e$, and $\Phi = 0.6$ to 0.8 $hc/2e$ in the $x = 0.35$ sample for $T \lesssim 10$ K. In both cases, conservatively estimating the error in background determination to be its standard deviation gives an error <0.6 $hc/2e$ for Φ, and estimating a maximum error of 20% in the scanner area calibration gives error 0.13 $hc/2e$. Hall probe images of isolated vortices were also fit in two dimensions to Equation (4.1) with free parameters $(z + \lambda_{ab})$, Φ, and a planar background. The best fits in the $x = 0.35$ sample gave total flux Φ primarily from 0.8 to 1.1 $hc/2e$ for $T < 10$ K, and from 0.6 to 1.0 $hc/2e$ for $\sim$11 K. Systematic errors dominate, such as the high correlation between the parameters $(z+\lambda_{ab})$ and Φ, the planar background fit, and the validity of the monopole model near T_c. An estimate of ± 0.2 μm for the error in $(z + \lambda_{ab})$ gives error bars ≤ 0.11 $hc/2e$ for Φ, while the latter sources of error are more difficult to quantify. Fits with Φ fixed at $hc/2e$ and at hc/e clearly show $hc/2e$ as the better fit (Figure 4.4). In all, we observed 60 vortices with the Hall probe in the very underdoped YBCO sample.

The Hall probe images show apparent vortex spreading in $YBa_2Cu_3O_{6.35}$ compared to the near-optimally doped crystal (Figure 4.3) that may be due to a penetration depth that is not negligible compared to the 2 μm Hall probe. Alternative hypotheses include vortex bending, fast vortex motion confined to a micron-scale region, or a non-superconducting layer on the crystal surface. The images in Figure 4.4 show the temperature dependent vortex spreading in the very underdoped YBCO, consistent with a $\lambda_{ab}(T)$ that increases with temperature. The full-width half-maximum of a vortex image in the $x = 0.95$ sample is 3.0 ± 0.3 μm (resolution-limited), while in the $x = 0.35$ sample it is 4.0 ± 0.3 μm at 3.2 K and 5.3 ± 0.3 μm at 10.5 K. From these numbers, and from the 2D fits with $(z + \lambda_{ab})$ as a free parameter, we interpret the major source of vortex spreading in the $x = 0.35$ YBCO as a penetration depth $\lambda_{ab} \gtrsim 1$ μm which increases with temperature. This inferred λ_{ab} is somewhat larger than expected from higher-T_c extrapolations (Uemura et al. 1989). A more thorough and quantitative study of λ_{ab} as a function of doping in underdoped cuprates is possible with higher resolution Hall probes, and is the subject of Chapter 5.

4.2.4 Discussion

Overall, we saw no hc/e vortices in SQUID and Hall probe images of more than 170 vortices in $YBa_2Cu_3O_{6.35}$. This result sets limits on scenarios of spin-charge separation; in particular, we set an upper limit on the vison energy in the Senthil-Fisher formulation. They propose that $E_{\rm vison} \approx k_B T^*$ (per 2D superconducting layer) (Senthil and Fisher 2001a,b). In usual Ginzburg-Landau theory, the energy per unit length of an $nhc/2e$ vortex is given by $E^{nhc/2e} = E_{\rm sf}^{nhc/2e} + E_{\rm core}^{nhc/2e}$, where

$$E_{\rm sf}^{nhc/2e} = \left(\frac{nhc/2e}{4\pi\lambda_{ab}}\right)^2 \ln(\lambda_{ab}/\xi) \tag{4.2}$$

is the superfluid energy, n is an integer, ξ is the coherence length, and $E_{\rm core}$ is small compared to $E_{\rm sf}$ (Tinkham 1996, p. 153–4). The vison can be cast as an excess core energy for an $hc/2e$ vortex (Senthil and Fisher 2001a). Thus we write $E^{hc/2e} = E_{\rm sf}^{hc/2e} + E_{\rm core} + E_{\rm vison}$, while $E^{hc/e} = 4E_{\rm sf}^{hc/2e} + E_{\rm core}$. The most natural interpretation of our observations of only $hc/2e$ vortices is that $2E^{hc/2e} < E^{hc/e}$, and therefore $E_{\rm vison} < E_{\rm sf}^{hc/2e}$ (neglecting pinning energy[3]). Conservatively using $\lambda_{ab} \approx 1$ μm and taking $\ln(\lambda_{ab}/\xi) \approx 5$, we set an upper limit on the excess core energy associated with an $hc/2e$ vortex: $E_{\rm vison}/k_B < 60$ K.[4]

In the context of the Senthil-Fisher predictions, the significance of this upper limit depends on the exact value of T^*, which will be difficult to measure in these very underdoped samples because the dopant oxygens disorder above room temperature. Early NMR measurements indicate that T^* exceeds 300 K in $YBa_2Cu_3O_{6.48}$ (Alloul et al. 1989). A more recent interpretation of the T^* energy scale indicates values as high as 500–700 K in very underdoped samples (Tallon and Loram 2001). Thus our upper bound on the vison energy is much below the predicted value. To reconcile this result with the predictions would require a superconducting transition which is

[3]With vortex pinning, $E^{nhc/2e}$ has an additional term $-E_{\rm pin}^{nhc/2e}$. Pinning potentials in high purity crystals may arise from small spatial variations in the doping. $E_{\rm pin}$ of a traditional vortex should be at most $\sim E_{\rm core}$, while here $E_{\rm pin}^{hc/2e}$ could include a vison contribution $E_{\rm pin}^{\rm vison}$. Since in theory $E_{\rm vison} \approx k_B T^*$, $E_{\rm pin}^{\rm vison}$ due to doping variations should be much smaller than $E_{\rm vison}$. Thus our energy balance expression becomes $E_{\rm vison} - E_{\rm pin}^{\rm vison} \approx E_{\rm vison} < E_{\rm sf}^{hc/2e}$ as before.

[4]$E_{\rm vison}/k_B < 120$ K if there is one vison per unit cell instead of per copper-oxide plane.

strongly first-order (Sachdev 1992; Senthil and Fisher 2001a), or a theoretical model of vortex formation that does not permit hc/e vortices even when they are energetically preferred (Senthil and Fisher 2001a). We tested one such model by imaging vortices after cooling just below T_c. Senthil and Fisher also proposed an ingenious experiment to address the dynamics issue by trapping a vison in a hole in a cuprate cylinder (Senthil and Fisher 2001b). These experiments have been done (Bonn et al. 2001; Kirtley et al. 2001), see Section 4.3.

In the overall context of cuprate superconductivity, this work has extended experimental studies of single magnetic flux quanta into a new part of the phase diagram which was first theoretically explored a decade ago (Sachdev 1992; Nagaosa and Lee 1992). Further vortex imaging in these very underdoped samples have allowed measurements of the apparent size of a vortex (an upper limit on the in-plane penetration depth) as a function of temperature and doping (Chapter 5), and studies of single vortex dynamics and energetics.

4.3 The vortex memory experiment[5]

A more stringent test for spin-charge separation in the cuprates is an elegant experiment devised by Senthil and Fisher (2001b) which tests for clear signatures of the proposed topological defects known as visons. The experiment address the dynamic nature of the vison, and thus interpretation of the results is not restricted by caveats of metastability as in the hc/e search discussed above. In this section I report our results of these experimental tests, which conservatively placed an upper limit of 190 K on the vison energy.

4.3.1 Experimental proposal

To test their theory of SCS, Senthil and Fisher (2001b) proposed a "smoking gun" experiment in which a vison is trapped in a ring made from a cuprate superconductor. Figure 4.5, as well as the inset to Figure 4.6, summarizes the experiment. The ring

[5]This vortex memory experiment was published as Bonn et al. (2001).

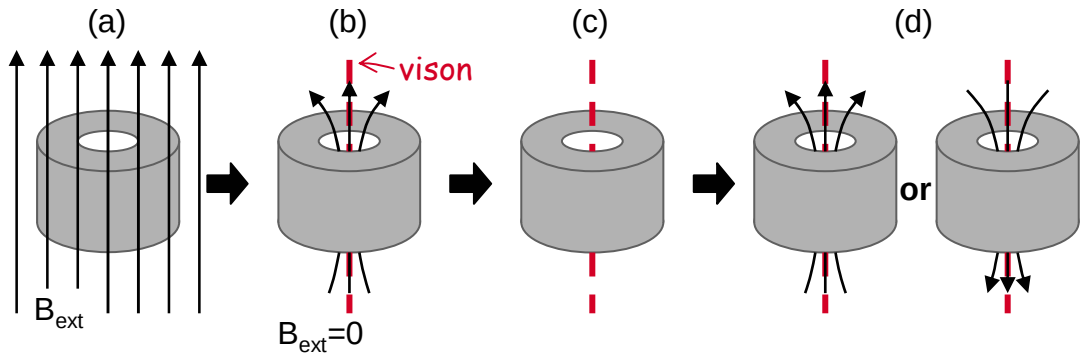

Figure 4.5: The Senthil–Fisher ring experiment to test for visons in a cuprate superconductor. The steps are as follows: (a) Field cool the ring below T_c with $B_{\rm ext}$ chosen to trap one flux quantum in the hole. (b) At low temperature turn off the field, leaving an $hc/2e$ vortex and the accompanying vison in the hole. (c) Quickly warm just above T_c to let the vortex escape but not the vison. (d) Cool back down below T_c in zero field. An $hc/2e$ vortex of random sign must appear in the hole due to the presence of the vison. $n > 1$ vortices can instead be prepared in the hole in step (a), but a vison would only be present if n was odd.

is cooled through T_c in an external field, of magnitude chosen to yield the desired number of vortices in the hole. The field is turned off at low temperatures and n flux quanta (each $hc/2e$) remain trapped in the hole. If n is odd, the ring must also contain a vison in order to preserve the single-valuedness of the wave function; but if n is even, no vison will be present. The ring is warmed just above T_c and the vortices escape. If the ring was prepared with n odd, and is recooled in zero field faster than the vison escape time, the ring must create a single flux quantum of random sign, since a vison cannot be naked in the superconductor. (If the ring was prepared with n even, this "vortex memory" upon cycling above T_c would not be expected, since no visons would be present.) We performed this experiment in very underdoped rings of $YBa_2Cu_3O_{6+x}$, where the vison escape time is the longest, and saw no signs of the vortex memory effect. Our null results place a limit on the vison energy that is less than the predicted energy scale, further supporting the null results discussed in Section 4.2, and constraining the theory.

For this experiment to work, the T_c of the superconducting ring must be low enough such that the temperature can be cycled faster than the vison escape time

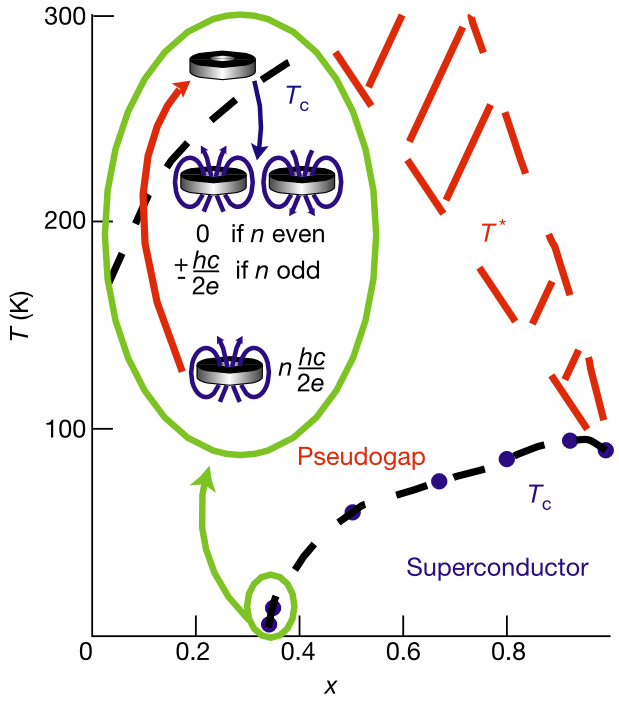

Figure 4.6: Vortex memory in the $YBa_2Cu_3O_{6+x}$ phase diagram. The superconducting transition temperature T_c can be tuned by adjusting the oxygen content x. The phase diagram also includes the characteristic pseudogap crossover temperature T^*. The lowest T_c's are found close to $x = 0.35$ and the search for visons is concentrated in this range. One predicted effect is the "vortex memory" shown in the inset. A superconducting ring containing one or more magnetic flux quanta is raised above T_c in zero magnetic field, but may still contain a vison if the starting point was an odd number of flux quanta. The presence of this vison would then spontaneously generate a vortex of random sign when the ring is recooled.

given by

$$\tau_{\text{vison}} = \tau_0 \exp[E_{\text{vison}}/k_B T], \tag{4.3}$$

where τ_0 is a microscopic attempt time and E_{vison} is the energy barrier for vison escape (Senthil and Fisher 2000). The escape time of a trapped vortex in the hole can be expressed similarly for $T < T_c$, where E_{vortex} includes a contribution from E_{vison} (if n is odd). An underdoped sample with a low T_c is desirable because $k_B T$ can be kept small during the thermal cycling. Also, E_{vison} is predicted to be the pseudogap energy scale $k_B T^*$ (shown in Figure 4.6), which increases with decreased doping.

4.3.2 Data and results

The low T_c $YBa_2Cu_3O_{6+x}$ crystals used in this experiment were from the same generation of samples used in the hc/e experiment (Section 4.2) and were grown by the same process as all the underdoped YBCO discussed in this dissertation. (See Section 1.3 and Liang et al. (1998, 2002) for details about the crystals.) The T_c of these high purity crystals is shown again in Figure 4.6 as a function of x. The ring experiment was performed on four crystals with successively lower transition temperatures, each of which had a single 10 μm diameter hole created with a focused ion beam. The flux trapped in the hole was imaged with the scanning SQUID microscope with an 8 μm $\times$ 8 μm pickup loop (Gardner et al. 2001). Three of the samples were cleaved into squares of roughly 50 μm $\times$ 50 μm so that the entire sample fit within the SXM microscope (Chapter 2) scan range. This allowed us to ensure that magnetic flux was not trapped in the sample outside the hole.

Figure 4.7 shows an set of vortex memory experiments to test for visons in the first of the small rings. The series of images show even and odd numbers of magnetic flux quanta trapped in the 10 μm hole, after cooling in an applied field and turning off the field at low temperature. The somewhat irregular shape is due to irregularities in the cleaved sample. The ring was prepared in each state by cooling in a small magnetic field and trapping between +6 and −3 flux quanta. After imaging, the sample was quickly heated and cooled again in zero external magnetic field. Subsequent imaging indicated that the flux escaped upon heating to 9.5 K for less than 10 s, and did not

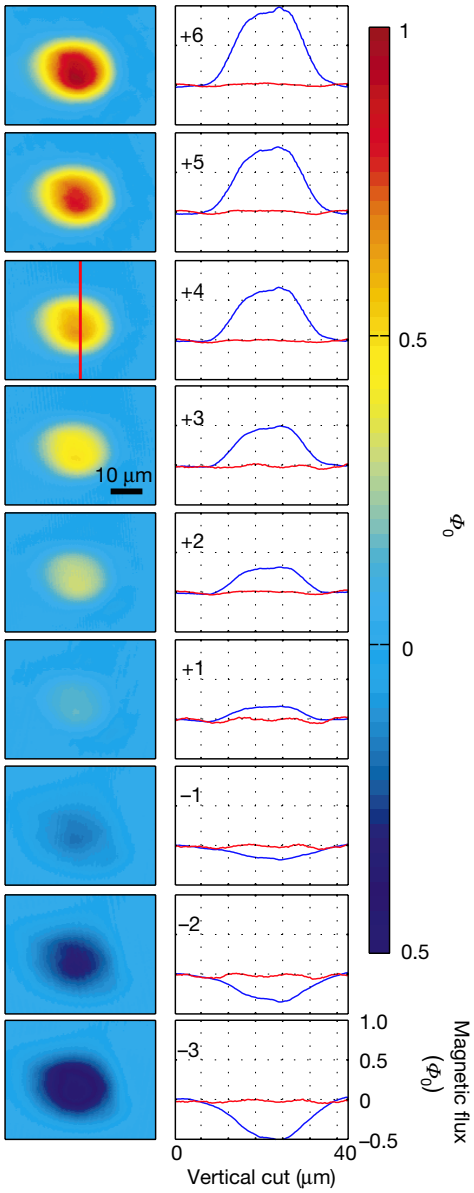

Figure 4.7: Magnetic flux trapped in a superconducting ring. The scanning SQUID images on the left show different numbers ($+6\Phi_0$ to $-3\Phi_0$) of flux quanta trapped in a 10 μm hole in a $YBa_2Cu_3O_{6.35}$ sample after cooling in a small magnetic field. On the right, vertical cross-sections of each image show the magnetic flux in the hole before (blue) and after (red) cycling the ring's temperature in zero external magnetic field. The after images are not shown. In all cases, the trapped vortices escape in less than 10 s at 9.5 K.

reappear. There was no dependence on whether the starting condition was an even or odd number of trapped flux quanta.

A more stringent test was done with two samples annealed to have lower transition temperatures. One sample had $T_c \approx 7.5$ K, and the other had an onset T_c of 6.0 K (2 K width) which could be measured in situ with the scanning SQUID. A serious difficulty with the lowest T_c sample was that magnetic flux was frequently trapped in the annulus of the ring rather than in the hole. Sometimes a single quantum of flux seemed to "leak" from the hole into the annulus. This could be "partial vortex" behavior, as discussed in Chapter 6, where a 2D stack of pancake vortices in a layered superconductor is partially displaced. It may also indicate granular behavior even though the rings are made from single crystals. The indications of granular behavior in only the lowest T_c ring could stem from slight inhomogeneity in the oxygen content of the crystal, leading to inhomogeneous doping. If this is the case, then the material that constitutes the junctions between superconducting grains is slightly more underdoped than the material in the bulk of the grains. In the Senthil-Fisher picture, the inter-grain material is a "fractionalized insulator" and the vison gap would still exist in the barrier (Senthil and Fisher 2001a). So, despite this possible indication of granularity, when discrete flux quanta were clearly trapped in the hole, the temperature could be cycled in null field to test for memory effects. Figure 4.8 shows cross-sections and images of quantized flux in the $T_c = 6.0$ K ring. Flux quanta of Φ_0 and $2\Phi_0$ were repeatedly trapped in the ring and then found to escape by heating to slightly below T_c, typically after only 1 s at 5.6 K, again with no sign of vortex memory.

4.3.3 Discussion

The null results of our ring experiments can be expressed as a limit on the energy of a vison by inserting the 1 s limit at 5.6 K into Equation (4.3). The value of τ_0 is unknown, but a lower limit is the time for an electron to cross one unit cell of the CuO_2 lattice. This estimate of $\tau_0 = 2 \times 10^{-15}$ s gives a conservative upper limit of $E_{\text{vison}}/k_B < 190$ K, far below the predicted pseudogap energy scale $k_B T^*$. A less

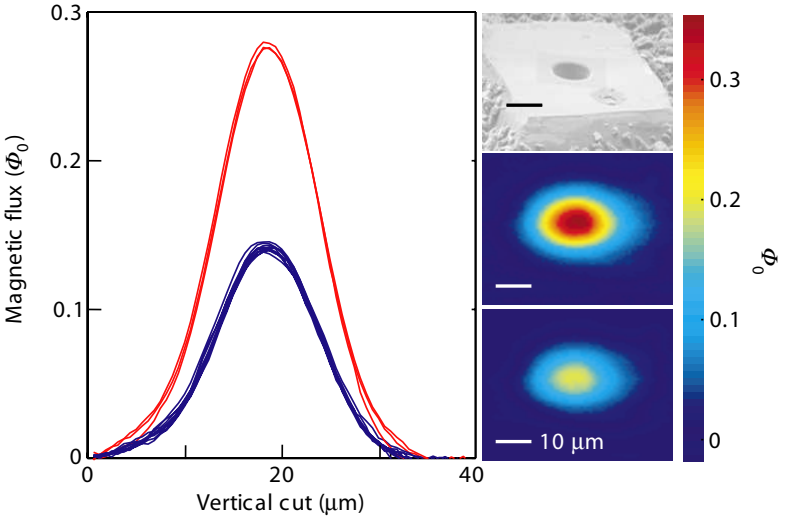

Figure 4.8: Cross-sections and images of flux quanta trapped in a ring with $T_c = 6.0$ K. The upper right image shows the typical geometry of the rings. They are squares (50 μm$\times$50 μm) of single-crystal $YBa_2Cu_3O_{6.35}$, with a 10 μm hole drilled using a focused ion beam. The middle and lower right images show double ($2\Phi_0$) and single (Φ_0) flux quanta trapped in the ring. Integration of the total flux in the images confirmed that the flux quantization is $\Phi_0 = hc/2e$. The cross-sections shown on the left are obtained from 20-pixel-wide vertical stripes through the images, with the 20 pixels averaged in order to reduce noise and carefully confirm the reproducibility of the flux quanta. The many cross-sections show that single and double flux quanta (blue and red curves, respectively) could be repeatedly generated in the ring, although there were also numerous instances where some of the flux appeared to "leak" into the annulus of the ring. When the ring was heated in null field to only 5.6 K for 1 s, then recooled to 2 K, imaging indicated that these flux quanta escape with no sign of the vortex memory associated with visons.

conservative lower bound on τ_0 that is commonly used in discussions of vortex creep in conventional superconductors is $\tau_0 = 10^{-12}$ s, based on the characteristic frequencies of lattice vibrations (Beasley et al. 1969). This higher estimate of τ_0 would give an upper limit of $E_{\rm vison}/k_B < 160$ K.

These ring experiments give a larger upper limit on $E_{\rm vison}$ than the observations of only $hc/2e$ static vortices in these samples discussed in Section 4.2. But the vortex memory experiment is a stricter test for visons, since it could be that the $hc/2e$ vortices in the earlier experiment were metastable. Measuring two steady states in the ring experiment (before and after thermal cycling) gives information on the dynamics, and thus also the energy scale, of possible trapped visons. The limit of $E_{\rm vison}/k_B < 190$ K restricts any role that visons might have in the physics of these materials in the underdoped regime.

4.4 Summary and the future of SCS

We conducted two experimental tests for a promising microscopic formulation of spin-charge separation (Senthil and Fisher 2000) in the underdoped cuprate superconductors. Both tests utilized the flux imaging capabilities of our scanning SQUID and scanning Hall probe microscope, and were made possible by the recent progress in the growth and preparation of high quality very underdoped single crystals of $YBa_2Cu_3O_{6+x}$ (Liang et al. 2002). In the first experiment we saw no evidence of hc/e vortices in very underdoped YBCO samples, though hc/e vortices are predicted by SCS for very underdoped cuprates. We also performed an experiment proposed by Senthil and Fisher (2001b) but saw no vortex memory effect, which would have been the signature of visons, the topological defects of the Senthil-Fisher SCS theory. The first experiment set a limit of $E_{\rm vison}/k_B < 60$ K, while the more stringent vortex memory experiment set a strict limit of $E_{\rm vison}/k_B < 190$ K. Both of these limits are much less than the predicted vison energy scale $E_{\rm vison} \approx k_B T^*$ (Senthil and Fisher 2001a). Together our experiments make unlikely any SCS scenarios for the cuprates which require visons.

SCS scenarios for the cuprates have not been abandoned however. Paramekanti

et al. (2002) propose a new model of an "exciton Bose liquid" in which bosonic Cooper pairs on a square lattice interact via ring exchange. They call their model a "middle ground" between a Mott insulator and the fully fractionalized SCS scenario. Ribeiro and Wen (2003) predict that there will be no fractionalization in hole-doped cuprates (such as YBCO), but they show that SCS is a candidate for the metallic pseudogap phase of electron-doped cuprates. Experimental studies on electron-doped cuprates are needed to test this possibility. Other theoretical work by Paramekanti et al. (2003) calculates that the vison gap in the cuprates could be much smaller than in the original Senthil and Fisher (2001a) formulation. They state that E_{vison} could be $\lesssim$50 K, which would mean fractionalization would only appear at very low temperatures and thus could not be responsible for the properties of the pseudogap.

Though the outlook for SCS in the cuprates is dubious, there is interest currently in the strong possibility of fractionalization in highly frustrated magnets. Coldea et al. (2001) saw evidence for a 2D fractional spin liquid in neutron scattering measurements on the frustrated antiferromagnet Cs_2CuCl_4. Senthil and Motrunich (2002) construct microscopic models of fractionalized phases and show that it is possible to have a SCS magnetic phase. Chung et al. (2003) examined the Cs_2CuCl_4 system theoretically. They computed models for both bosonic and fermionic[6] spin liquid states which predict different temperature dependent behavior for neutron scattering measurements. Further experiments are needed to determine which type fractionalization exists in the magnetically frustrated Cs_2CuCl_4 system. Frustrated magnets are promising candidates for 2D fractionalization because the inherent frustration leads to deconfinement of the antiferromagnetic spins.

[6]The spin-charge separation tested for cuprates in this chapter is of the fermionic sort, since the spinon had spin 1/2.

Chapter 5

Penetration depth measurements

The submicron scanning Hall probe microscope and the newly available extremely underdoped superconducting $YBa_2Cu_3O_{6+x}$ (YBCO) single crystals from UBC (Liang et al. 2002) enable studies of magnetic vortices in the very underdoped region of the cuprate phase diagram (Figure 1.1). This region of very small superfluid density is theoretically important but until recently remained unexplored experimentally due to the absence of good samples with sharp superconducting transitions. In this chapter I discuss my attempts to measure the in-plane penetration depth (λ_{ab}) in the very underdoped YBCO.

This chapter first introduces the penetration depth (λ), summarizes various methods used to measure λ in the literature, and introduces the widely accepted "Uemura relation" that $T_c \propto 1/\lambda^2(0)$. Then I detail my Hall probe imaging studies of individual vortices in a very underdoped $YBa_2Cu_3O_{6.375}$ crystal, which had a variable T_c from 5 to 15 K. Fits of my images to a model of the vortex field profile allowed the size of the vortex to be measured. The size (as I am defining it) of a traditional 3D vortex is λ_{ab}, though in these anisotropic crystals it is possible that staggered pinning of 2D pancake vortices contribute to the measured apparent size. If staggered pinning is not the case, my results suggest a larger penetration depth than predicted by the Uemura relation for at least $T_c \leq 6.5$ K.

5.1 Introduction

An important parameter of a superconductor is the magnetic penetration depth. It is the length scale over which external magnetic fields penetrate the superconductor and are exponentially screened. In the vortex state λ determines the extent or size of the vortices, that is, the length over which the vortex magnetic field and supercurrent fall off. The penetration depth is directly related to the superfluid density, n_s/m^*, by the relation $n_s/m^* = (c^2/4\pi e^2)\lambda^{-2}$, where n_s is the superconducting carrier density and m^* is the effective mass.[1] The superfluid density is a parameter of great theoretical importance. Its value and dependence on doping and temperature allow theories of superconductivity to be tested and formulated. This is of particular importance in the high-T_c cuprate superconductors where the mechanism of superconductivity is not yet understood.

In anisotropic superconductors, such as the cuprates, the penetration depth and m^* are direction dependent. The superconductor in this case can be described by an anisotropic version of the London model with λ_a, λ_b, and λ_c associated with the *abc* crystal axes. (The YBCO crystal structure was shown in Figure 1.11.) λ_a is the decay length for supercurrent flowing in the a direction, similarly for b and c. In terms of magnetic field, if B (either external or from a vortex) points along the c-axis, λ_a is the distance the field penetrates in the b direction, and λ_b is the distance the field penetrates in the a direction. This statement holds for cyclic permutations $abc \rightarrow bca \rightarrow cab$. In cuprates, λ_c is large compared to λ_a and λ_b, while $\lambda_a \sim \lambda_b$ and they are often referred to collectively as the in-plane penetration depth $\lambda_{ab} = \sqrt{\lambda_a \lambda_b}$.

5.1.1 Methods of measuring λ

The absolute value of the penetration depth is difficult to measure. There is no universal easy method to do so, though several classes of techniques have been developed, each of which have advantages and drawbacks. Broadly, the techniques

[1] The literature is not consistent in defining the term superfluid density. Emery and Kivelson (1995a) define it as n_s, Pereg-Barnea et al. (2003) define it as n_s/m^*, and Tallon et al. (2003) define it as λ^{-2}.

are those that measure λ by examining (1) the magnetic susceptibility in the Meissner state, (2) transmission and spectroscopy, or (3) the field distribution in the vortex state. I will briefly discuss the predominant techniques below. In this chapter I fit the field profiles of isolated c-axis vortices at the sample surface in an attempt to measure λ_{ab} in very underdoped $YBa_2Cu_3O_{6+x}$. Though there are caveats to this measurement, namely I have actually measured the apparent vortex size which could have contributions besides λ_{ab}.

Magnetic susceptibility techniques can very accurately measure penetration depth relative to a base temperature: $\Delta\lambda(T) = \lambda(T) - \lambda(T_{\rm base})$. This has been done at DC (Krusin-Elbaum et al. 1989), microwave (Hardy et al. 1993), and radio frequencies (Carrington et al. 1999). Cavity and planar resonators have both been used for the AC measurements. As the penetration depth changes (e.g. with T), the volume of the sample which is superconducting changes, and thus very accurate $\Delta\lambda$ measurements can be made. However, the absolute penetration depth is difficult to obtain via these methods, since it would require unrealistically precise knowledge of the sample dimensions. An exception is for very large penetration depths, such as the recent microwave cavity measurements of absolute λ_c in underdoped $YBa_2Cu_3O_{6+x}$ by Hosseini et al. (2003).

An improved approach to the planar resonator technique has been implemented by Talanov et al. (2000) which does allow absolute measurement of λ. In their apparatus, a parallel plate resonator is composed of either the thin film or bulk superconductors in which λ is to be measured. The key feature of their apparatus is that the spacing between the parallel plates can be continuously varied with known spacing. The resonant frequency is dependent on the penetration depth and the spacing, and thus λ can be determined from fits to the experimentally measured resonant frequency as a function of spacing.

Pereg-Barnea et al. (2003) at UBC have devised a new microwave technique for measuring absolute values of the three λ components from the Meissner state. They grew single crystals of $YBa_2Cu_3O_{6+x}$ with 1% of the Y^{3+} ions randomly replaced by magnetic Gd^{3+} ions. Measurements of the electron spin resonance (ESR) of the Gd atoms in an applied microwave field reveals the number of Gd in the field. Since only

the Gd within one penetration depth are exposed to the field, the penetration depth on all three axes can be found from the ESR measurement.

A successful transmission technique for measuring λ involves measuring the mutual inductance of two coaxial coils separated by a thin film superconductor (Fiory et al. 1988; Lee et al. 1994). This method is restricted to thin films, and the film thickness and uniformity must be know for an accurate result. Infrared spectroscopy (Basov et al. 1995) has also been used to measure λ and is not restricted to thin films. Each component of the penetration depth (λ_a, λ_b, and λ_c) can be measured independently. Infrared spectroscopy is a challenging technique and requires measurement over a very large frequency range to obtain the λ results.

Muon spin resonance (μSR) is a technique that measures λ from the magnetic field distribution inside a superconductor in the vortex state. Polarized muons are implanted in a sample and the precession of the muon spin depends on the local magnetic field. The muon decays into two neutrinos and a positron, and the direction of the positron emission is dependent on the direction of the instantaneous muon spin polarization at the time of decay. Thus by detecting the emitted positrons, the distribution of magnetic field in the sample can be probed. Since the field profile of the vortex lattice depends on the bulk penetration depth, λ can be determined from fits to the μSR data. For a thorough review of μSR applied to the vortex state, see Sonier et al. (2000). μSR cannot measure the penetration depth for a single axis, rather it measures a mean such as λ_{ab}. The μSR measurement of λ depends on having a detailed model of the magnetic fields of the vortex lattice. Also, at high fields the measured λ can differ from the Meissner state λ. The assumed model for the magnetic field distribution, the geometry of the vortex lattice, and twinning boundaries can each contribute errors to the absolute measurement of λ_{ab}, but measurements of $d\lambda_{ab}/dT$ are relatively unaffected by these uncertainties (Sonier et al. 2000). The μSR technique is also limited to measuring $\lambda \lesssim 1$ μm (Uemura et al. 1991).

All of the above techniques have advantages and disadvantages, and rely to varying extents on underlying models in order to measure the penetration depth. Some of the techniques cannot measure the absolute value of λ, or cannot isolate the components

of λ in anisotropic crystals, or are limited to measuring thin films or small penetration depths. Therefore, having a number of independent techniques is beneficial for confirming penetration depth results and overcoming systematic uncertainties. Also, the techniques discussed above are predominantly bulk or whole surface measurements, so they do not allow for measurement of λ inhomogeneity. The technique implemented in this chapter, measurement of λ_{ab} from Hall probe images of individual vortices, can in principle measure the degree of homogeneity of λ_{ab} within one vortex and by comparing vortices. This technique is best at measuring larger penetration depths, which is appropriate for the very underdoped YBCO.

5.1.2 The Uemura relation

It is generally accepted in cuprate superconductivity that the superconducting transition temperature T_c is proportional to the zero-temperature superfluid density in the underdoped regime. This result is called the "Uemura relation" because it was first suggested by μSR measurements of the penetration depth reported by Uemura et al. (1989, 1991). Their measurements on many high-T_c cuprates and other unconventional superconductors revealed a universal linear relation between T_c and the superfluid density for underdoped samples: $T_c \propto \lambda(0)^{-2} \propto n_s(0)/m^*$. Because of the theoretical importance of the Uemura relation and its wide acceptance as a phenomenological rule, it is important extend tests of this relation into the very underdoped range, where $T_c \lesssim 0.1\ T_{c,\max}$ and the superfluid density is very low.

Emery and Kivelson (1995a) explained the Uemura relation as a bound on T_c from thermal phase fluctuations:

$$T_\theta^{\max} = A\frac{\hbar^2 n_s(0) a}{4m^*} = A\frac{(\hbar c)^2 a}{16\pi e^2 \lambda(0)^2}. \tag{5.1}$$

For the quasi-2D underdoped cuprates, $A \to 0.9$ and $\lambda \to \lambda_{ab}$ as interlayer coupling vanishes, and $a = \max(d, \xi_c)$, where d is the average plane spacing and ξ_c is the c-axis coherence length. In the cuprates $d > \xi_c$ over the experimentally explored phase space, and Equation (5.1) quantitatively explains the Uemura relation. Quantum phase fluctuations can also play a role in further limiting the T_c in underdoped samples, by

a factor of 5–7% in pristine YBCO crystals (Emery and Kivelson 1995b) and more in disordered samples. At optimal doping the phase ordering temperature $T_\theta^{\max}$ becomes comparable to the mean-field transition temperature (T^{MF}), while for overdoped samples $T_\theta^{\max} > T^{MF}$ and so the T_c is determined by T^{MF} (Emery and Kivelson 1995a).

Despite the wide acceptance of the Uemura relation, a few recent papers such as Tallon et al. (2003) and Pereg-Barnea et al. (2003) question this relation with penetration depth results that do not fall on the Uemura slope. These recent reports are even further motivation for measuring λ_{ab} in the very underdoped $YBa_2Cu_3O_{6+x}$ crystals.

5.2 Measurements of vortex size in $YBa_2Cu_3O_{6.375}$

I took scanning Hall probe microscopy images of individual vortices in a newly available single crystal of $YBa_2Cu_3O_{6.375}$ (Liang et al. 2002). T_c was tuned in situ by room temperature annealing, giving T_c's ranging from 5 to 15 K. The apparent vortex size was measured by fitting the vortex images. This imaging technique allowed direct observation of spatial variations down to the submicron scale. The vortices became more homogeneous and sharper as T_c increased, as can be seen in Figure 5.1.

The vortex images were taken with the goal of measuring the in-plane penetration depth λ_{ab}. The size[2] of a vortex in the bulk is λ_{ab} for a conventional vortex. In highly anisotropic superconductors, the superconductivity occurs primarily in 2D layers, and a c-axis vortex can be modelled as a stack of 2D pancake vortices (Clem 1991) as shown in Figure 5.2(a). Figure 5.2 also shows other possible pancake configurations. Sketch (b) shows a "split" pancake vortex stack, which when imaged from above looks like isolated "partial vortices" each carrying sub-Φ_0 flux (if the horizontal split displacement is greater than the Hall probe microscope's spatial resolution). Partial vortices were observed often in this $YBa_2Cu_3O_{6.375}$ crystal, with decreasing occurrence as T_c was increased, and are discussed in detail in Chapter 6. For the λ_{ab}

[2]By "vortex size" I mean the extent of the vortex flux or supercurrent in the bulk, not the vortex *core* size.

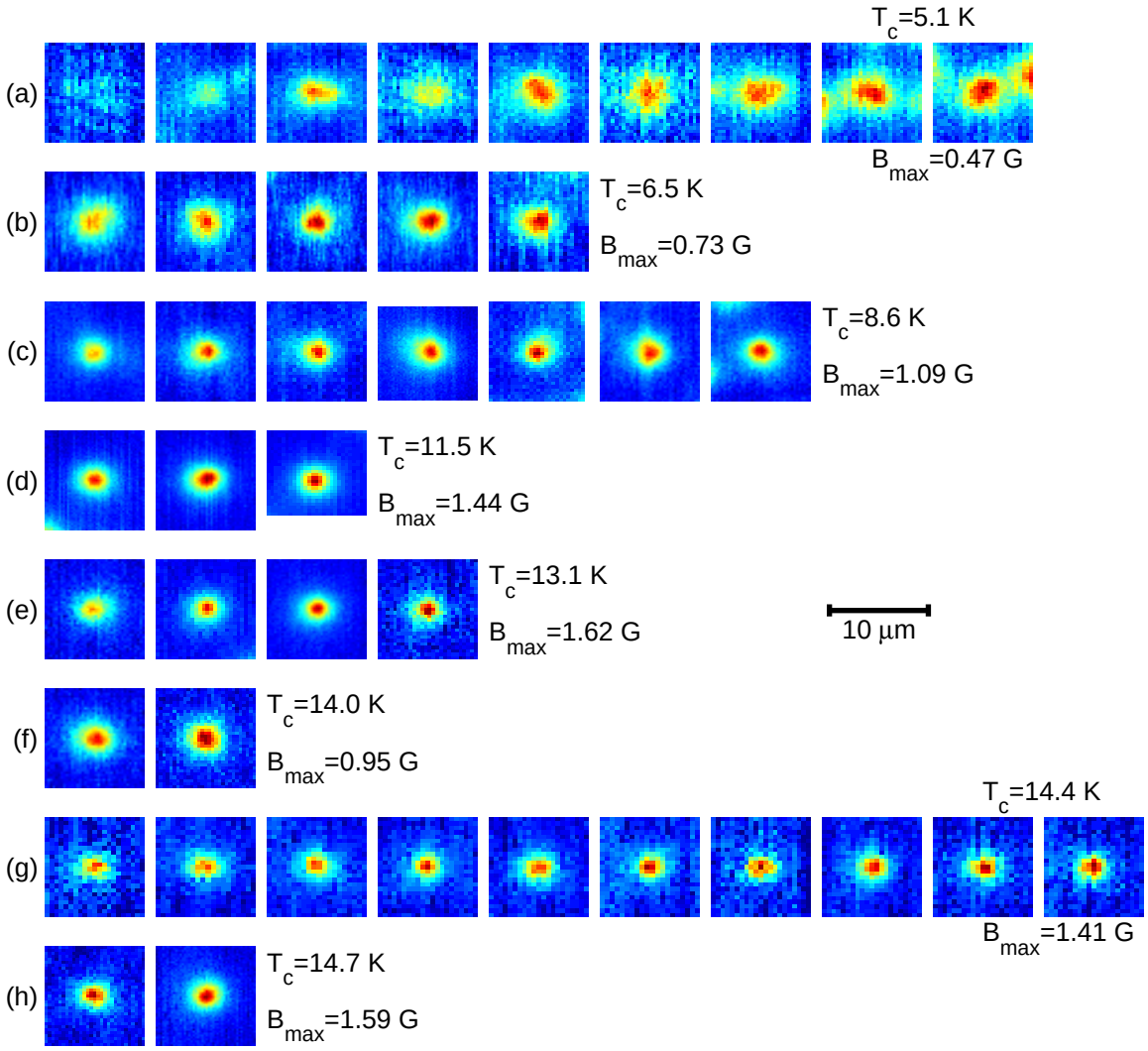

Figure 5.1: Individual vortices imaged with a 0.5 μm Hall probe in a $YBa_2Cu_3O_{6.375}$ crystal with variable T_c. These 42 images were each fit to a model of the vortex field profile to determine the apparent vortex size (s_{ab}, where $s_{ab} = \lambda_{ab}$ if there is not staggered pinning of pancake vortices). Rows (a)–(h) show images obtained for increasing T_c values. In each row the images are arranged from left to right by decreasing fitted s_{ab} values. A constant offset, determined by fitting, was subtracted from each image. The color-scale for each row extends from $-B_{\max}/10$ (blue) to $+B_{\max}$ (red). The height of the Hall probe $z = z_0 + \Delta z$ was not the same for all images, Δz differed by a controlled amount $\leq$0.16 μm, though we believe z_0 was constant.

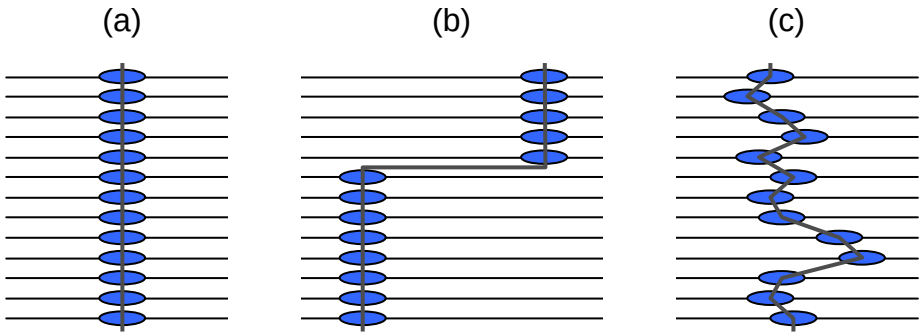

Figure 5.2: Possible configurations of 2D pancake vortices in a layered superconductor. (a) A straight pancake vortex stack is identical to a conventional 3D vortex in the limit of small layer spacing. (b) A split stack which looks like isolated "partial vortices" when viewed from above. (c) A vortex with staggered pinning of the pancakes. The apparent size of a staggered stack is larger than that of the straight stack in (a).

measurements, I chose images of vortices which were quasi-isolated and brighter than any nearby partial vortices, in an attempt to select full vortices described by Figure 5.2(a) rather than split stacks as in Figure 5.2(b). However, this does not exclude the possibility of a staggered stack as sketched in Figure 5.2(c), in which the pancakes are pinned in each layer with slight random displacements. The apparent size of a vortex composed of staggered pancakes would be larger than λ_{ab}. We cannot tell from our images if the apparent full vortices are described by Figure 5.2(a) or (c). My vortex fits measure the apparent vortex size, which I will denote as s_{ab}. This size is the sum of λ_{ab} and the average of the pancake displacements in the staggered stack. If there is no staggered pinning of the 2D pancake vortices, then $s_{ab} = \lambda_{ab}$.

5.2.1 The YBCO sample

It has proven difficult to make very underdoped cuprate superconductors with sharp T_c's. In YBCO, the doping is controlled by high mobility chain oxygens, making it possible to achieve a high degree of homogeneity. Very underdoped high-purity YBCO crystals are grown with a recently improved self-flux method in $BaZrO_3$ crucibles by Liang et al. (1998, 2002). The desired oxygen content is set during a 900–930°C anneal in flowing oxygen, then oxygen inhomogeneities are removed during

a 1–2 week 570°C anneal in a small tube with YBCO ceramic at the same oxygen content. Initially after quenching to 0°C, the crystals are non-superconducting, but annealing at room temperature allows the oxygen atoms to order into Ortho-II chain fragments whose increasing length provides the carrier doping in the CuO_2 planes. T_c increases with room temperature annealing until saturation is reached after several weeks, giving final T_c values of 5–20 K with bulk susceptibility transition widths (10%–90%) less than 2 K (Liang et al. 2002). During the room temperature anneal, a crystal can be observed at a range of T_c values for the same sample. The platelet shaped crystals are about 1 mm × 1 mm with the *ab*-plane parallel to the surface, and typically have thickness 10–100 μm. As grown, the crystals have twinning boundaries (interchanging of the a and b axes), but they can be detwinned by applying high pressures at elevated temperatures. The crystals were discussed in more detail in Section 1.3.

The results presented here are from an 8 μm thick $YBa_2Cu_3O_{6.375}$ crystal imaged at eight stages during the room temperature oxygen ordering anneal. After 36 hours of room temperature annealing, the crystal had $T_c \sim 5.1$ K and transition width $\Delta T_c \sim 3$ K. Subsequently, T_c increased quasi-logarithmically with anneal time, giving a range of T_c values all having $\Delta T_c < 1.5$ K. The maximum T_c measured was 14.7 K after a total anneal time of 39 days. Table 5.1 (and Figure 1.13) gives details of the transition temperature obtained versus anneal time for this crystal. T_c values were obtained in situ by the Hall probe in an 8.3 mHz applied field of amplitude 0.20–0.25 G. The observed transitions are described as midpoint T_c's with determination of the full widths limited by the ∼10% resolution of the susceptibility measurement. Figure 5.3 shows the full susceptibility transitions measured with the Hall probe. Note that the Hall probe response in the normal state does not always saturate at the same values. This could indicate small fractions of the sample with a higher T_c, or just be due to fluctuations in the Hall coefficient of the probe from cooldown to cooldown.

Table 5.1: T_c values and apparent vortex size (s_{ab}) results from fits to vortices in a $YBa_2Cu_3O_{6.375}$ crystal. The actual error from z_0 uncertainty should be similar for all T_c values, since z_0 is constant though unknown (0.4 μm $< z_0 <$ 1.3 μm). The results are also shown graphically in Figure 5.6.

RT anneal [days]	Midpt. T_c [K]	Est. width 10%–90% ΔT_c [K][a]	# vortex fits	Range of $s_{ab}(T \ll T_c)$ [microns][b]	Average $s_{ab}(T \ll T_c)$ [microns]		
					R_H err.		z_0 err.
1.5	5.1	2.6	9	1.7 – 4.3	2.38	$\pm$0.26	$^{+0.43}_{-0.48}$
1.9	6.5	1.0	5	1.2 – 1.5	1.35	$\pm$0.18	$^{+0.37}_{-0.43}$
2.7	8.6	1.4	7	0.9 – 1.4	1.04	$\pm$0.15	$^{+0.36}_{-0.42}$
6.4	11.5	1.0	3	0.6 – 0.6	0.61	$\pm$0.12	$^{+0.34}_{-0.40}$
12.4	13.1	1.4	4	0.6 – 0.7	0.64	$\pm$0.12	$^{+0.35}_{-0.40}$
20.2	14.0	0.8	2	0.8 – 1.0	0.90	$\pm$0.15	$^{+0.36}_{-0.41}$
28.5	14.4	0.9	10	0.6 – 0.7	0.65	$\pm$0.13	$^{+0.34}_{-0.40}$
39.1	14.7	1.1	2	0.6 – 0.6	0.57	$\pm$0.11	$^{+0.34}_{-0.40}$

[a] ΔT_c fluctuations for $T_c \geq 6.5$ K are from measurement noise, not sample intrinsic.
[b] These s_{ab} values are those obtained assuming $R_H = 0.115$ Ω/G and $z_0 = 0.8$ μm.

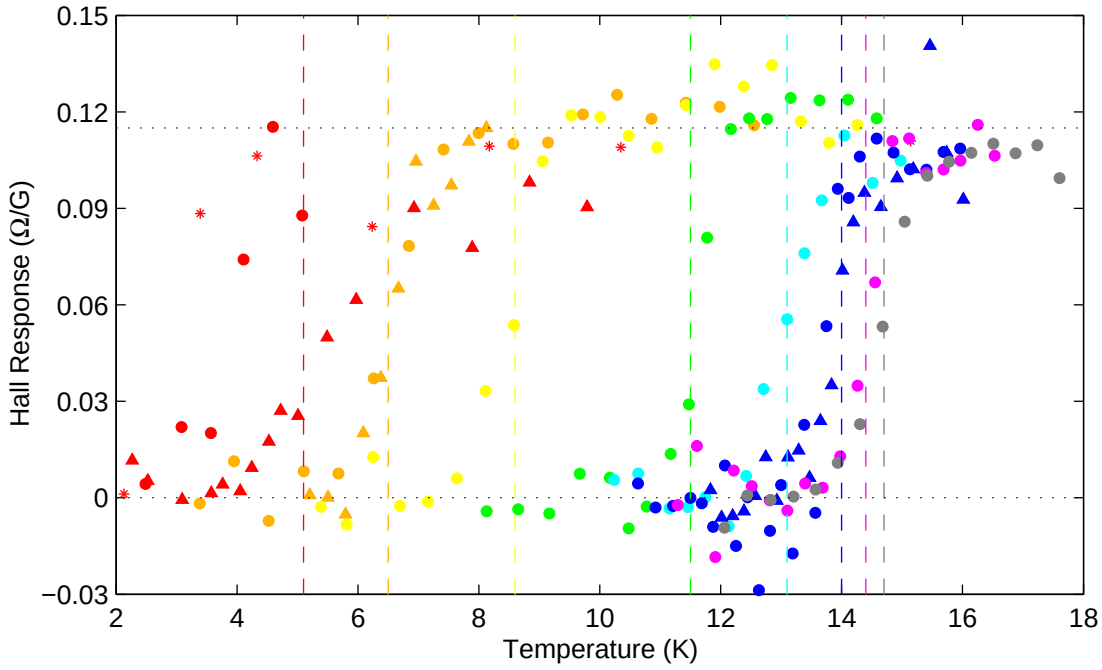

Figure 5.3: Superconducting transitions in the $YBa_2Cu_3O_{6.375}$ crystal as measured by in situ magnetic susceptibility. Each color represents a different anneal stage. Triangles are for second measurements. Vertical lines indicate the estimated midpoint T_c of the full width transition at each anneal stage. The data for the two lowest T_c's (red and orange) were with $B_{\max} = 0.25$ G, except for the red * data points which were with $B_{\max} = 1.0$ G. All higher T_c transitions were taken with $B_{\max} = 0.20$ G. The Hall coefficient was estimated to be $R_H = 0.115 \pm 0.015$ Ω/G.

5.2.2 Vortex imaging

Scanning Hall probe microscopy of single vortices is an established technique (Chang et al. 1992; Davidović et al. 1996; Oral et al. 1996b) first demonstrated by Chang et al. (1992). The Hall probe used here was made from GaAs/AlGaAs two-dimensional electron gas (2DEG) and had lithographic size 0.5 μm $\times$ 0.5 μm. (See Section 3.4). Due to depletion in the 2DEG, the size of the active area is somewhat smaller than the lithographic dimensions. The Hall probe measures the perpendicular magnetic field in the active area, with respect to a constant offset intrinsic to the probe. The minimum height z_0 of the active area above the sample surface is limited by the 2DEG depth (140 nm), by the distance between the active area and the corner of the Hall probe chip (8 μm), and by the angle between the Hall probe chip and the sample ($\geq 1^\circ$). z_0 is determined by precise alignment and is by far the largest source of error in my fit results. For this reason it was critical to make measurements for a range of T_c on the *same* crystal during a *single* alignment to keep z_0 constant and thus control the systematic error. I performed the room temperature annealing of the $YBa_2Cu_3O_{6.375}$ sample in situ to keep z_0 constant.

Isolated vortices were trapped by cooling the sample in a small applied field inside triple-layer mu-metal magnetic shielding with a residual field <25 mG. Figures 5.1 shows vortex images for the range of T_c values. At lower T_c the vortex fields are more spread out and have smaller amplitude, indicative of a larger apparent size s_{ab}. The lower T_c vortices were often non-circular, particularly for the minimum $T_c = 5.1$ K, and also showed more variation in peak height from vortex to vortex. In general, the vortices at higher T_c looked sharper and more uniform. It should be mentioned that the asymmetries of the vortex shapes were not consistently aligned with the *ab* axes, and thus are not a result of differences between λ_a and λ_b. If that were the case, and if our crystal had been detwinned (it was not), this Hall probe technique could in principle independently measure the two components of the in-plane penetration depth.

The apparent vortex size s_{ab} in the bulk is related to the degree of spreading of the vortex field profile above the sample surface. As mentioned earlier, there could be two contributions to the apparent size s_{ab} measured in this very underdoped anisotropic

YBCO crystal. If there is no staggered pinning (Figure 5.2(c)) of the 2D pancake vortices, then $s_{ab} = \lambda_{ab}$, and the inhomogeneities in the vortex shapes could indicate micron-scale inhomogeneities in λ_{ab}. If there is staggered pinning, $s_{ab} > \lambda_{ab}$, and the non-uniform vortex shapes could be due to asymmetric staggering, or similarly a series of split stacks (Figure 5.2(b)) with unresolvable displacements. The observation of what we believe to be split stacks or partial vortices, discussed in Chapter 6, suggests that staggered pinning of the pancake vortices is a possibility in this crystal. In total, I fit 50 images of 42 different vortices in the $YBa_2Cu_3O_{6.375}$ sample. Only vortices which appeared to be isolated and not partial vortices were chosen.

5.2.3 Vortex fitting

The anisotropic London model, in the thick crystal limit[3] with the *ab*-plane parallel to the surface, gives the perpendicular field from a vortex (Pearl 1966; Kogan et al. 1993; Kirtley et al. 1999a,c)

$$B_z(r,z) = \frac{\Phi_0}{2\pi\lambda_{ab}^2}\int_0^\infty dq\,\frac{q\ J_0(qr)\ e^{-qz}}{q^2+\lambda_{ab}^{-2}+q\sqrt{q^2+\lambda_{ab}^{-2}}}, \tag{5.2}$$

where r is the radial distance from the vortex center, z is the height above the sample surface, and $\Phi_0 = hc/2e$. Due to other potential contributions to the apparent vortex size (s_{ab}), I take $\lambda_{ab} \rightarrow s_{ab}$ in Equation (5.2) and perform fits for s_{ab} rather than explicitly for λ_{ab}. (The fitting procedure is the same regardless of whether we call the size s_{ab} or λ_{ab}.) For the fitting model, I integrated Equation (5.2) at constant z over a 0.5 μm diameter circular area representing the Hall probe. The results are insensitive to the exact Hall probe size and shape,[4] which are unknown due to depletion of the

[3]Using the ∞-thick crystal limit introduces only small errors for the 8 μm sample at the largest measured low-temperature vortex size values. Taking a crystal thickness of 8 μm and $s_{ab} = \lambda_{ab} =$ 4 μm, comparison of the ∞-thick solution with the full solution (Kirtley et al. 1999c) accounting for crystal thickness shows that $B_z(r)$ differs by at most 4 mG and $B_z(r=0)$ by a few % for our possible z values.

[4]s_{ab} values obtained from fits directly to Equation (5.2) were nearly identical to those from our convolved model, differing at most by 10 nm, indicating that the Hall probe size could have been neglected entirely.

2DEG. I fit the vortex images using non-linear regression with Mathematica® to extract s_{ab} with fixed z. Free parameters were the location of the vortex center, a constant offset, and s_{ab}. See Appendix A for further details on the model and fitting procedure. The lengths z and s_{ab} are strongly correlated and could not both be free parameters.

In the scanning microscope $z = z_0 + \Delta z$, where z_0 is the sample-probe distance when touching, and Δz is controllable and for these measurements ranged from 0–0.16 μm. A lower bound of $z_0 \geq 0.4$ μm exists from geometric constraints. A very conservative upper bound of $z_0 \leq 1.45$ μm was obtained for this data set by fitting the vortices at maximum T_c with $s_{ab} = \lambda_{ab} = 0$ and z as a free parameter (see Section A.1). A smaller upper bound of $z_0 \leq 1.3$ μm was obtained by assuming that $s_{ab}(0)$ is at least as large as $\lambda_{ab}(0)$ values measured in optimally doped YBCO (Basov et al. 1995). This is still a conservative assumption, since it is well known that the superfluid density decreases (and thus the penetration depth increases) as doping is reduced from optimal. All vortices were fit with a range of z_0 values. Fit results are reported here with a typical value $z_0 = 0.8$ μm, with systematic error bars determined by fits with $z_0 = 0.4$ μm and $z_0 = 1.3$ μm. The choice of the typical z_0 value was based on earlier alignments and measurements of vortices in samples with known λ_{ab}.

I also imaged other very underdoped YBCO crystals at single T_c values, three with a 0.5 μm Hall probe and others with larger sensors, and obtained consistent s_{ab} results. Fits to vortices in a second $YBa_2Cu_3O_{6.375}$ crystal (50 μm thick) measured at $T_c = 8.3$ K gave $s_{ab} = 1.0$–1.1 μm with the choice of $z_0 = 0.8$ μm. Two $YBa_2Cu_3O_{6.358}$ crystals were also imaged at their saturation $T_c = 17$ K. Vortices in these samples gave s_{ab} ranging from 1.3–2.1 μm with the choice of $z_0 = 0.8$ μm. However, these choices of z_0 for the fits were arbitrary and not experimentally verifiable. Roughly, error in z_0 translates to the same magnitude and opposite sign of error in s_{ab}, since the parameters are highly correlated. The measurements in these three crystals had uncontrolled systematic errors, primarily the uncertainty in z_0 which was bounded only by $z_0 > 0.4$ μm, so in this chapter I focus on data obtained from the single sample of $YBa_2Cu_3O_{6.375}$ over a range of T_c, which allowed partial control of the systematic z error.

I did make attempts to measure the angle between the sample and the probe, which would in principle allow calculation of the minimum height z_0 of the probe active area above the sample. This was done with a CCD camera and microscope which could view the sample-probe alignment through the side optical ports of the cryostat. This method of determining z_0 did not give trustworthy results. For example, I imaged vortices in a near-optimally doped YBCO crystal, for which λ_{ab} has been measured by other techniques in similar samples. The anisotropy of optimally doped YBCO is much lower than for the very underdoped crystals, so the observed apparent vortex size s_{ab} should equal λ_{ab} in the near-optimally doped crystal. During one alignment, fits to the vortices in that sample with z as a free parameter gave $z_0 = 2.1$ μm (a larger than usual value), while measurement of the sample-probe angle obtained with the camera predicted only $z_0 \approx 0.7$ μm. The z discrepancies could be due to curvature of the sample, inability to measure the angle accurately from the optical pictures, or even due to extra material on the tip or sample surface which would contribute extra distance to z_0. In light of these problems, I conservatively state the errors in the s_{ab} results without attempting to measure z_0 from the alignment angle.

In another attempt to tighten the uncertainty limits of z_0, I performed many fits to three vortices in the $YBa_2Cu_3O_{6.375}$ crystal at the $T_c = 8.6$ K anneal stage. The fits were done for a large array of fixed z and s_{ab} values to see how the goodness of fit depended on those parameters. (For these vortex images Δz was zero, so $z = z_0$.) The lower the T_c, the larger the s_{ab}, and thus the further away we are from the limit in which Equation (5.2) (with $\lambda_{ab} \rightarrow s_{ab}$) simplifies to a monopole solution (Appendix A.1) where z and s_{ab} enter only as $(z + s_{ab})$. I did not choose vortices with $T_c < 8.6$ K, which had even larger apparent vortex size s_{ab}, since they were less homogeneous and thus not as ideal for fitting. I computed the average squared error between the data and fits for a grid of z and s_{ab}. Selecting only those fits within a 90% confidence interval gave z ranges of $0.1 - 0.6$, $0.3 - 1.1$, and $0.1 - 0.3$ μm respectively for the three vortices. Clearly this is not a sufficient method to place bounds on z_0, since the 90% limits placed by each vortex do not even all overlap, and values $z_0 < 0.4$ μm are not physically possible due to geometric constraints. Furthermore, this analysis assumed a normal distribution of errors, which is not the actual case and

which underestimates the z spread of the confidence intervals. This analysis further confirmed that z and s_{ab} are just too correlated to treat them independently. A new scheme to accurately determine z_0 is highly desirable, such as a probe fabricated with a small STM pillar on top of the active area. Then z_0 would be equal to the pillar height plus the depth of the 2DEG.

5.2.4 Results

Figure 5.4 shows 2D fits of representative vortices at low temperature for the lowest and highest T_c values of 5.1 and 14.7 K. Fitting the radially symmetric model to inhomogeneous vortex profiles such as Figure 5.4(a) is an approximation which gives an average of the apparent vortex size.

For four vortices I also took Hall probe images while warming to investigate temperature dependence. Figure 5.5(a) plots the apparent vortex size $s_{ab}(T)$ for vortices at the minimum and maximum T_c stages. The superfluid density ($\propto \lambda_{ab}^{-2}$) in cuprates has been found experimentally to be linear in T for $T \ll T_c$ (Hardy et al. 1993). This slope $d(\lambda_{ab}^{-2})/dT$ has also been found to be doping independent (Bonn et al. 1996). Within our systematic and statistical errors, it is not possible to extract the details of the temperature dependence of the penetration depth (if we assume $s_{ab} = \lambda_{ab}$) from our measurements. Figure 5.5(b) plots $s_{ab}^{-2}(T)$ for our data along with $\lambda_a^{-2}(T)$ data for $YBa_2Cu_3O_{6.60}$ from (Bonn et al. 1996) for comparison. The slopes of our data are consistent with the $YBa_2Cu_3O_{6.60}$ data, but meaningful conclusions cannot be drawn due to our large systematic error bars. The measured s_{ab} is roughly constant for $T \lesssim T_c/2$ (Figure 5.5(a)). Thus I approximate $s_{ab}(0)$ by $s_{ab}(T)$ with $T \sim 2$ K for $T_c < 12$ K and $T \sim 4$ K for higher T_c's.

The low temperature apparent vortex size s_{ab} versus T_c results are shown in Figure 5.6(a) and summarized in Table 5.1. The apparent vortex size is an upper bound on λ_{ab}, and if there is not broadening due to pinning, $s_{ab} = \lambda_{ab}$. To check the robustness of the fit to the amount of included background, for six vortices I took multiple images varying only the image size. The s_{ab} values varied by at most 0.1 μm and I averaged these s_{ab} results to obtain one data point per vortex. The dominant sources of error

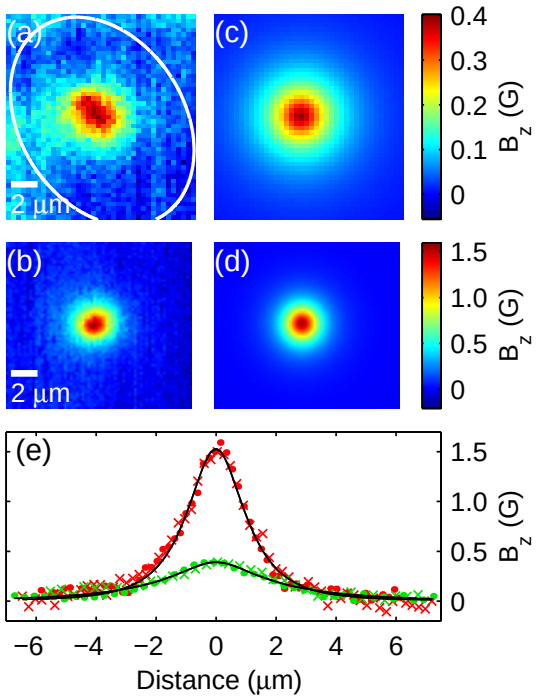

Figure 5.4: Scanning Hall probe vortex images and fits to a model described in the text (with $z_0 = 0.8$ μm) in a $YBa_2Cu_3O_{6.375}$ single crystal. (a) For $T_c = 5.1$ K and $T = 2.0$ K. The non-uniform shape was typical of vortices at this T_c. (b) For $T_c = 14.7$ K and $T = 4.0$ K. (c) 2D fit to image (a) within the white oval with best fit parameter $s_{ab} = 1.86$ μm. (d) 2D fit to image (b) with best fit parameter $s_{ab} = 0.55$ μm. Images and fits are displayed with a constant offset subtracted and color-scales corresponding to the bars at right. (e) Horizontal ($\times$) and vertical ($\bullet$) cross-sections through the vortex center in image (a) (green), image (b) (red), and corresponding fits (c) and (d) (black lines).

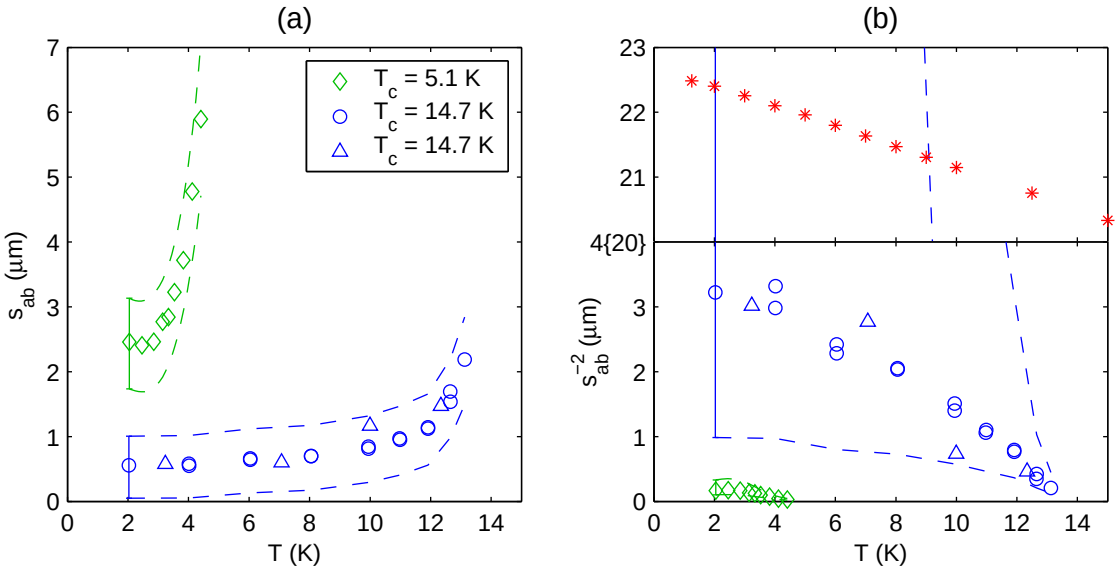

Figure 5.5: Temperature dependence of the apparent vortex size s_{ab} in a $YBa_2Cu_3O_{6.375}$ crystal for T_c values 5.1 K and 14.7 K. In the absence of staggered pinning of the 2D pancake vortices, $s_{ab} = \lambda_{ab}$. For each of our data sets shown, s_{ab} was obtained from fits to scanning Hall probe images of an individual vortex as T increased. The vortices disappeared at $T < T_c$. The dashed lines indicate the maximum extent the data sets could be shifted due to systematic errors. (a) Apparent vortex size s_{ab} vs. T. (b) s_{ab}^{-2} vs. T for the same data as plotted in (a). The red * data are $\lambda_a^{-2}(T)$ from Bonn et al. (1996) for a $YBa_2Cu_3O_{6.60}$ crystal with $T_c = 59$ K. (Note that the vertical axis skips values between 4–20 μm.)

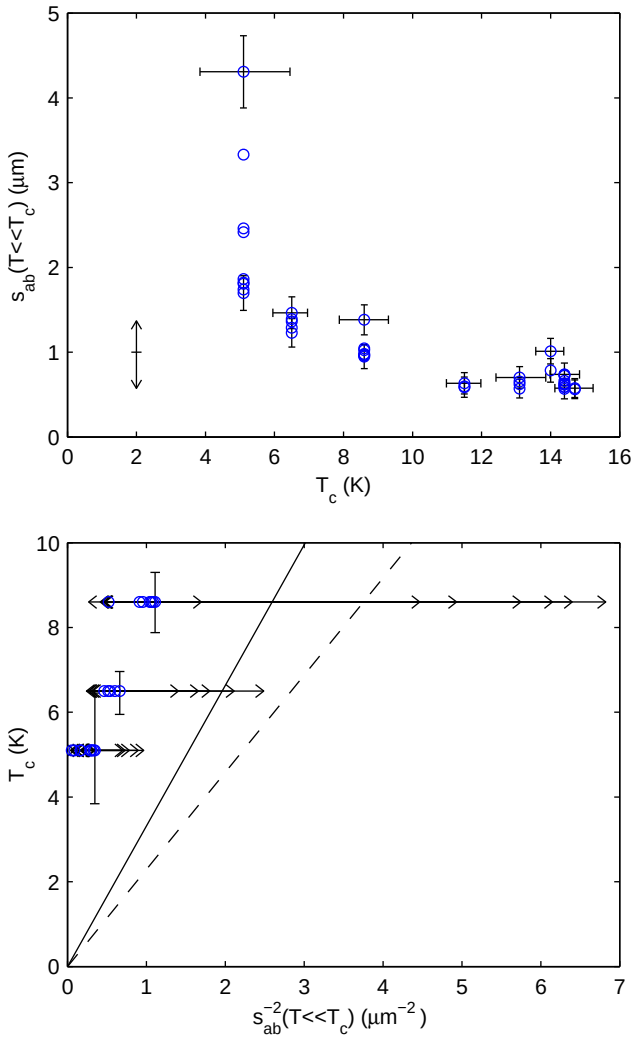

Figure 5.6: Apparent vortex size $s_{ab}(T_c)$ for a $YBa_2Cu_3O_{6.375}$ crystal. (a) s_{ab} versus T_c. $T \leq 2.4$ K for $T_c < 12$ K and $T \leq 4.3$ K for $T_c > 12$ K. s_{ab} was obtained from fits to scanning Hall probe images of 42 different vortices at eight T_c stages of a room temperature anneal. Horizontal bars indicate the resolution-limited full width of the superconducting transition for each T_c. Vertical error bars are from uncertainty in the probe calibration (shown only for the extreme data points). A systematic error from uncertainty in the minimum sample-probe distance z_0 could shift the full data set by the extent indicated by the double arrow at $T_c = 2$ K. Data points shown are with $z_0 = 0.8$ μm. (b) Plot of T_c versus s_{ab}^{-2} for $T_c < 10$ K. Horizontal error bars include *both* the probe calibration *and* z_0 uncertainties. Solid line is $T_\theta^{\max}$ from Equation (5.1). Dashed line is computed assuming a linear relation through zero from a recent measurement of $\lambda_a(0) = 202 \pm 22$ nm in YBCO with $T_c = 56$ K (Pereg-Barnea et al. 2003), consistent with results in Sonier et al. (1997).

in the s_{ab} results are the uncertainty in z_0 (which will be the same for all data points) and the calibration of the probe's Hall coefficient, $R_H = 0.115 \pm 0.015\ \Omega/\mathrm{G}$. Fits with the z_0 extremes show that the corresponding s_{ab} error, indicated by the double arrow in Figure 5.6(a) and given for the average $s_{ab}(T_c)$ in Table 5.1, is roughly constant for all data points. The uncertainty in R_H translates to an s_{ab} error of roughly $\pm 8\%$ of $(z + s_{ab})$. R_H can change slightly from cooldown to cooldown, so unlike z_0, it is not necessarily the same for all the T_c values. Under the assumption that Equation (5.2) with $\lambda_{ab} \rightarrow s_{ab}$ is the correct theoretical description of our measured field profiles, other systematic and statistical errors are small compared to those of z_0 and R_H.

At the lowest T_c of 5.1 K, the apparent vortex size s_{ab} varies significantly from vortex to vortex and ΔT_c is nearly twice that of higher T_c's. This might be explained by local T_c variations on the tens-of-micron length scale and could suggest that the oxygen ordering and in-plane doping was somewhat inhomogeneous after the shortest anneal time. The narrow widths $\Delta T_c < 1.5$ K and smaller s_{ab} variations for $T_c \geq 6.5$ K may indicate increased homogeneity. Alternatively, s_{ab} might be dominated by staggered pinning of the pancake vortices (Figure 5.2(c)) at the lowest T_c's, or undetected split pancake stacks, and thus the variations in s_{ab} could be due to pinning.

It is useful to examine the s_{ab} results in the assumed case of $s_{ab} = \lambda_{ab}$. Figure 5.6(b) shows the low temperature data plotted as T_c versus s_{ab}^{-2} (recall that λ_{ab}^{-2} is proportional to the superfluid density). The data deviate from the linear Uemura relation, shown as the solid line. The fits gave low temperature values $s_{ab} \approx 1.7 - 4.3\ \mu$m for the lowest $T_c \sim 5$ K. In contrast, Equation (5.1) gives $T_c \approx (3.3\ \mathrm{K}\ \mu\mathrm{m}^2)\lambda_{ab}^{-2}(0)$ for YBCO, or $\lambda_{ab}(0) = 0.8\ \mu$m for $T_c = 5$ K. If $s_{ab} = \lambda_{ab}$, then my data indicate that a smaller $n_s(0)$ can yield 5 and 6.5 K transition temperatures. The higher T_c data are inconclusive due to increasingly large error bars from the z_0 uncertainty. If the Uemura line is computed from a recent measurement of $\lambda_a(0)$ by Pereg-Barnea et al. (2003), as shown by the dashed line in Figure 5.6(b), our data deviate even more from the line.

5.2.5 Discussion and implications

The interpretation of my apparent vortex size measurements as a function of T_c in the very underdoped $YBa_2Cu_3O_{6+x}$ is contingent on the behavior of the 2D pancake vortices schematically shown in Figure 5.2. If the imaged vortices were not straight pancake stacks, but instead pinned with unresolvable horizontal displacements, the apparent vortex size s_{ab} would be larger than λ_{ab}.

Let us examine the pancake vortices in more detail. These crystals have a large anisotropy λ_c/λ_{ab}, as confirmed by recent measurements of $\lambda_c(0) \sim 100$ μm for $T_c \sim 6$ K (Hosseini et al. 2003), so it is indeed appropriate to treat a vortex as composed of 2D pancake vortices as first introduced by Clem (1991). Neglecting Josephson coupling ($\lambda_c \to \infty$), the potential of a single pancake dislocated a distance ρ from an otherwise straight stack is (Clem 1991):

$$U_0(\rho) = E_0[\gamma + \ln(\rho/2\lambda_{ab}) + K_0(\rho/\lambda_{ab})], \tag{5.3}$$

where $E_0 = \Phi_0^2 s/(8\pi^2\lambda_{ab}^2)$, γ is Euler's constant, and $s = 1.17$ nm is the YBCO bilayer spacing. Assuming $\lambda_{ab} = 0.8$ μm from Equation (5.1) at $T_c = 5$ K, the potential well width would be $\rho < 0.3$ μm for $U_0(\rho)/k_B < 5$ K. This indicates that pancake thermal fluctuations cannot be the sole source of our large apparent vortex sizes. Bluhm confirmed this calculation with Monte Carlo simulations of the whole pancake stack using the exact magnetic interaction potential including surface effects.

As mentioned already, pinning might cause misalignment of the pancakes. The force required to unpin a vortex has been estimated by Gardner et al. (2002) to be $\sim$0.5 pN for a similar YBCO crystal with $T_c = 11$ K. This is the total force on roughly a thousand pancakes within a penetration depth of the surface. The restoring force on a dislocated pancake calculated from $U_0(\rho)$ is of order 0.5 fN, showing that pinning could be strong enough to distort the straight pancake stack, resulting in a staggered pancake stack (shown in Figure 5.2(c)). Thorough studies of pinning landscapes in these and other cuprates are needed.

If pinning turns out not to be contributing to our measured apparent vortex size s_{ab}, then $s_{ab} = \lambda_{ab}$, and the data indicate that the model of a linear upper bound

on T_c due to phase fluctuations in a quasi-2D superconductor, Equation (5.1) with $a = d > \xi_c$, is not appropriate here. Within the context of Equation (5.1), other length scales could determine a. ξ_c has not been measured in these samples and could be larger than d, as would be expected if the disappearance of superconductivity at low doping is described by a quantum critical point. If there is a continuous $T = 0$ superconducting to non-superconducting transition at a critical doping level x_0, the coherence length ξ (and ξ_c) must diverge as $x \to x_0$. There would be a crossover to 3D physics with $\xi_c \gg d$, and thus at very low doping ξ_c would be the characteristic length scale a, yielding $T_c \propto \xi_c \lambda_{ab}^{-2}(0)$ (Kivelson). Alternatively, if the superconductor is granular and undergoes a percolation transition as doping decreases, a could be determined by the cluster size (Kivelson). Either scenario is qualitatively consistent with our data. The noticeably inhomogeneous field profiles in the lowest T_c data may support the idea of an inhomogeneous superconductor at the micron scale, but give no direct information on granularity at the nanometer or tens of nanometers scale.

5.3 Conclusions

In summary, I used a scanning Hall probe microscope to image individual vortices in very underdoped $YBa_2Cu_3O_{6+x}$ with T_c varied from 5 to 15 K. I observed spatial variations of the vortex field profiles at the lowest T_c's and from fits obtained the apparent vortex size $s_{ab}(T_c)$. If this size is governed only by $\lambda_{ab}(T_c)$, the results do not agree with the widely accepted Uemura relation $T_c \propto \lambda(0)^{-2} \propto n_s(0)/m^*$. Instead, they would indicate that lower superfluid densities can support T_c's of 5.1 and 6.5 K. Note that this deviation cannot be explained by including quantum phase fluctuations (Emery and Kivelson 1995a,b) because that would predict deviations in the other direction (higher n_s/m^* for these T_c values).

The alternative explanation for the large apparent vortex sizes is that the vortices are not appropriately modelled as a straight stack of pancake vortices, but are instead pinned as misaligned or "staggered" stacks. In that case our measurements of the apparent vortex size s_{ab} are a superposition of the in-plane penetration depth and the length scale of the pancake displacements. Our results do yield upper bounds on λ_{ab},

since $\lambda_{ab} \leq s_{ab}$.

The very underdoped region of the cuprate phase diagram is important to study, and is available for experiment thanks to the YBCO single crystals from UBC (Liang et al. 1998, 2002). Other techniques for measuring λ_{ab} should be performed on these very underdoped crystals to supplement the results presented here. The recent results presented by Pereg-Barnea et al. (2003) and Tallon et al. (2003) show deviations from the linear Uemura relation for higher dopings than our very underdoped crystals. More sample development and studies of other very underdoped cuprates will help determine the underlying physics in these samples.

Chapter 6

Partial vortices

In this chapter I will discuss unexpected observations of magnetic vortices which appeared to carry total flux less than the superconducting flux quantum $\Phi_0 = hc/2e$. These features were observed with scanning magnetic microscopy in very underdoped $YBa_2Cu_3O_{6+x}$ (YBCO) single crystals with $x \approx 0.35 - 0.375$. (See Section 1.3 for a basic introduction to the crystals.) Observations were made initially with an 8 μm Superconducting QUantum Interference Device (SQUID) and later more extensively with a 0.5 μm Hall probe.

Fluxoid quantization is a fundamental property of superconductivity. For this reason it was surprising to see these apparent isolated sub-Φ_0 features, which I will call *partial vortices*. In this Chapter I will first briefly review fluxoid quantization in a superconductor. In Section 6.2 I will introduce the partial vortex images, discuss properties of the partial vortices, and give statistics on their prevalence and magnitude. Then I will discuss some of the initial but rejected scenarios for creating these partial vortices before introducing a proposal for what these partial vortices really are. We believe they are caused by a full vortex that is partially displaced horizontally (a "split pancake vortex stack"). This is possible only in quasi-2D layered superconductors where the vortex can be treated as stack of 2D pancake vortices (Clem 1991). Flux quantization is not violated by the split stack. In Section 6.4 I discuss the split stack idea in detail and show that it does indeed agree with experimental observations.

6.1 Review of flux quantization

There are two classes of superconductors: type I and type II. For type II superconductors $\lambda/\xi > 1/\sqrt{2}$, where λ is the magnetic penetration depth and ξ is the coherence length (the length scale over which the superconducting order parameter can vary). Cuprates are type II superconductors. Unlike type I superconductors which exhibit a first order superconducting-to-normal transition at a critical field H_c, type II superconductors have an intermediate range between two critical fields (H_{c1} and H_{c2}) where they remain superconducting but allow bundles of flux to enter. These flux bundles are associated with vortices of supercurrent surrounding a non-superconducting core of radius ξ. When $\lambda > \xi$ (type II), the energy of a normal-superconducting boundary is negative and so the bundles of flux divide into smaller and smaller units to lower the energy. (See Tinkham 1996, p. 11-3).

The flux bundles cannot subdivide into infinitesimal flux units. The flux of each bundle must be quantized, which can be shown from the following argument (from Tinkham 1996, p. 127-8). Superconductivity is a macroscopic quantum state described in Ginzburg-Landau theory by a complex order parameter $\Psi = |\Psi| e^{i\phi}$, where $n_s = |\Psi|^2$ is the superconducting carrier density. The phase of the order parameter must be single valued, so $\oint \nabla\phi \cdot d\mathbf{s} = 2\pi n$, where n is an integer. The supercurrent kinetic energy term in the Ginzburg-Landau free energy expression gives $m^*\mathbf{v}_s = \hbar\nabla\phi - e^*\mathbf{A}/c$. Combining the equations leads to the fluxoid quantization condition

$$\Phi + \frac{m^*c}{e^*}\oint \mathbf{v}_s \cdot d\mathbf{s} = n\frac{hc}{e^*} \tag{6.1}$$

where $e^* = 2e$ (Cooper pairs) and $\Phi = \oint \mathbf{A} \cdot d\mathbf{s}$ is the flux through a closed path. The supercurrent density is $\mathbf{J}_s = 2en_s\mathbf{v}_s$. Chose an integration path that encloses a flux bundle. For distances large compared to the penetration depth, $\mathbf{J_s} \to 0$ and thus $\mathbf{v}_s \to 0$ and the quantization condition simply becomes $\Phi = nhc/2e$. Since the boundary energy in type II superconductors is negative, $n = 1$ gives the lowest energy state and flux enters the superconductor in units of the superconducting flux quantum $\Phi_0 = hc/2e$. A flux bundle carrying $1\Phi_0$ is called a vortex.

Therefore a vortex in a sample with lateral dimensions large compared to λ (so

that there is a path with $\mathbf{v}_s = 0$) cannot carry less than Φ_0 of flux, because the phase would not be single valued. There are exceptions to this statement in situations where something other than flux contributes to the phase winding. An elegant example is the tri-crystal experiments by Kirtley et al. (1996, 1999b) which proved that the superconducting order parameter for cuprates is *d*-wave (rather than *s*-wave like conventional superconductors). Their experiment was done on a thick film of YBCO specially grown in three sections, each with a different orientation of the *ab* axes. The sections met at a single tri-crystal point. The crystal axes orientations and the boundary angles were chosen to create a π phase winding around the tri-crystal point. This is possible with a *d*-wave material because the order parameter has four lobes of alternating sign. Crossing a boundary from a minus lobe to a plus lobe results in a π phase shift. Since there is already a π-shift, the flux at that point must be half-integer to ensure that the total phase winding is $2\pi n$. The observation by Kirtley et al. (1996, 1999b) of a spontaneously generated half-integer flux quantum at the tri-crystal point gave conclusive evidence for *d*-wave superconductivity.

The tri-crystal example shows that the presence of grain boundaries of particular orientation in a *d*-wave superconductor can result in vortices of half-integer multiples of Φ_0 without violating the single-valuedness of Ψ. However in a *single crystal*, like the $YBa_2Cu_3O_{6+x}$ discussed in this dissertation, there should not be grain boundaries aside from twinning (the interchange of the *a* and *b* axes) which cannot result in any phase winding of π or any fraction thereof. A π shift can occur across a twin boundary, but any closed path crossing a twin boundary would have to cross an even number of boundaries, and thus only could acquire phase windings of $2\pi n$.

Two categories of explanations for sub-Φ_0 vortices come out of the above discussion: fluxoid quantization where the current does not go to zero, so $\Phi < \Phi_0$, and non-flux sources of a phase winding other than 2π.

6.2 Partial vortex observations

Partial vortices were observed in four very underdoped $YBa_2Cu_3O_{6+x}$ single crystals, out of at least ten that were imaged. Generally, partial vortices were seen for

$T_c \sim 7$ K and not for $T_c \geq 11$ K.[1] Initial partial vortex observations were made with scanning SQUID microscopy in three crystals, while more detailed studies of partial vortices were done later on a fourth crystal with a scanning Hall probe. This crystal had $x = 0.375$ and its T_c was varied in stages from 5 to 15 K by room temperature annealing. Vortex imaging was also done on Ortho-II ($T_c \approx 60$ K) and near-optimally doped YBCO crystals, neither of which showed partial vortices.

An 8 μm scanning SQUID was used in the first observations of partial vortices in single crystal samples of $YBa_2Cu_3O_{6.354}$ and similar oxygen content. At least six bulk crystals were observed with the SQUID and partial vortices were seen in three of them. The crystals in which partial vortices were *not* seen had T_c between 11 and 13 K. Partial vortices were only seen with the SQUID in crystals with lower transition temperatures obtained by annealing the samples (separately) for about one week at ∼40°C. Two of the three partial vortex SQUID samples had $T_c \approx 7$ K, while the third had an unmeasured[2] T_c between 7 and 12 K. Transition widths were not determined for all the samples, but when measured, the higher T_c samples (11–13 K) had $\Delta T_c < 2$ K while those with lower T_c had widths ∼3 K.

In one of the $T_c \approx 7$ K samples, approximately 16 different partial vortices were observed, as well as roughly equivalent numbers of full vortices. Some vortices were difficult to classify due to the limited spatial resolution of the SQUID. This crystal was also used for vortex pushing and annihilation experiments described in Gardner et al. (2002). Two images of partial vortices in this crystal are shown in Figure 6.1. Image (a) shows a full vortex with a partial vortex neighbor whose peak flux Φ_S through the SQUID is only ∼40% of the peak Φ_S of the full vortex. The bright vortex was determined to be a full vortex from a 1D fit using the monopole model of a vortex field profile (see Appendix A.1). Image (b) shows two neighboring partial vortices of different amplitude. The brighter partial vortex has twice the amplitude of

[1] One exception was the crystal studied at a range of T_c with the Hall probe. Partial vortices were observed above 11 K, but with decreasing percentages as T_c increased to 15 K.

[2] Transition temperatures above 7 K cannot be measured directly with the SQUID due to the Nb SQUID's low operating temperatures. For higher T_c samples studied with the SQUID, the T_c was measured either in a bulk SQUID magnetometer, with a non-scanning Hall probe setup, or deduced approximately from changes to the vortex configuration when the sample was cycled to temperatures above T_c.

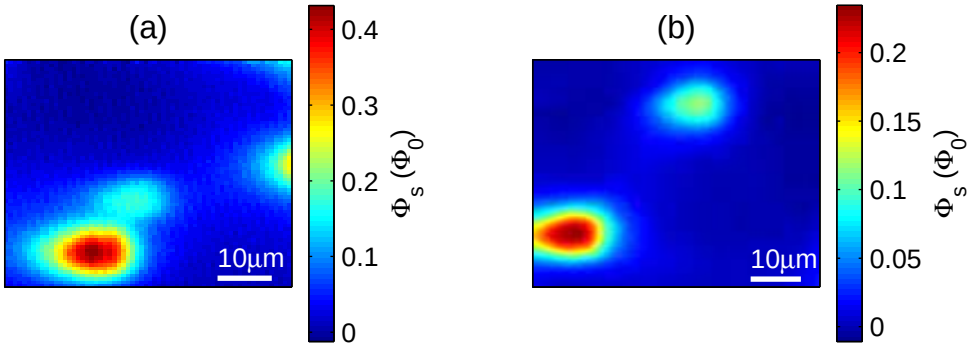

Figure 6.1: SQUID images of partial vortices in a $YBa_2Cu_3O_{6.354}$ crystal with $T_c \approx 7$ K. (a) The red vortex is a full Φ_0, while above it to the right is a smaller bit of flux – a partial vortex. $T = 2.6$ K. (b) Both vortices are only partial ones, since their peaks are significantly smaller than that of the full vortex in (a). $T = 2.1$ K. The sideways teardrop shape of the vortices is due to flux focusing by the leads of the SQUID's 8 μm pickup loop.

the smaller one. Though fits and integration results are not accurate enough to prove it, they are consistent with the suggestion that the flux carried by the two partial vortices in (b) add up to one Φ_0.

The sample of unknown T_c (between 7 and 12 K) was only studied briefly due to difficulties with sample-SQUID alignment and a not-so-great sample surface. Eleven images containing 18 vortices total were obtained, each image was after field cooling through T_c. One of these vortices was clearly a partial vortex, while three others were also likely partial vortices. Figure 6.2 shows SQUID images from this sample. Image (a) shows a full vortex (brightest one), a definite partial vortex, and some additional flux off the top of the image. The alignment and surface problems prevented good fits to the vortices, but I have assumed that the brightest vortex carried a full flux quantum due to the observation of many other identical vortices in this sample. The peak flux for the partial vortex in (a) is about 67% of the full vortex peak. In an effort to further study the partial vortex phenomena, after image (a) I cycled the temperature above T_c and cooled in similar conditions. In nine of these subsequent temperature cycles, only once did a possible partial vortex appear – at the location of the flux at the very top of image (a). After all the other cycles, only full vortices were observed such as those shown in image (b). This indicated that in this sample,

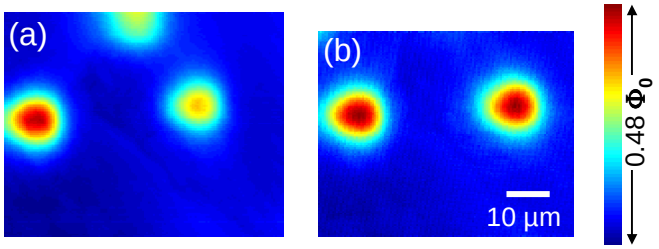

Figure 6.2: Partial and full vortices in very underdoped YBCO (exact T_c unknown) at 3.5 K imaged with the SQUID. (a) A partial vortex is on the right, while other flux is off the top of the image and a full vortex is present on the left side. (b) After thermal cycling above T_c, 8 out of 9 times only full vortices like those shown here appeared.

at least within the observed region, the probability of forming partial vortices was relatively small.

Later I made detailed studies of partial vortices in a newer sample using a scanning Hall probe. The Hall probe's lithographic size was only 0.5 μm, giving much better spatial resolution than the 8 μm SQUID. The flux sensitivity of the Hall probe, while not as good as for the SQUID, was sufficient for imaging most partial vortices. The sample imaged with the Hall probe was an 8 μm thick $YBa_2Cu_3O_{6.375}$ single crystal that had not yet undergone a final room temperature anneal. Annealing the crystal at or near room temperature allows the CuO chain oxygens to form chainlets whose length controls the in-plane doping and T_c. (For more information about this YBCO crystal, see Sections 1.3 and 5.2.1). By imaging the crystal at eight stages during the anneal, I obtained data for a range of T_c from 5 to 15 K on the same crystal. This is the same crystal on which extensive fits were done to assumed full vortices to measure the apparent vortex size (Chapter 5). Several other $YBa_2Cu_3O_{6+x}$ crystals were also imaged with a Hall probe, one with $x \approx 0.35$ and $T_c = 12.7$ K, and two with $x = 0.358$ and $T_c = 17$ K, but none of these showed partial vortices.

Over 100 partial vortices were seen with the Hall probe in the $YBa_2Cu_3O_{6.375}$ crystal. Representative images of these partial vortices are shown in Figure 6.3 for various T_c. The images shown in Figure 6.3 were taken at temperatures $T \ll T_c$ after field cooling the crystal in a perpendicular field $B_z \leq 0.5$ G. The cryostat was inside triple-layer mu-metal magnetic shielding with residual field <25 mG. The cooling rate

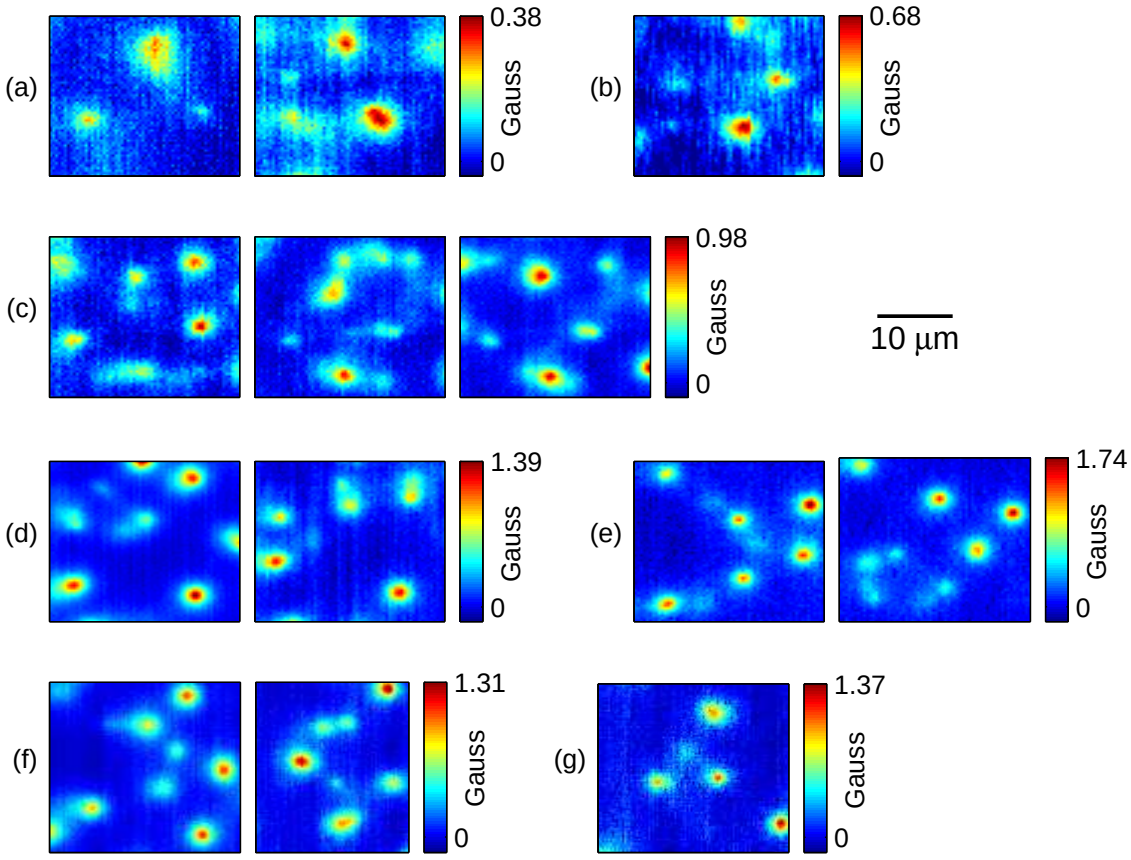

Figure 6.3: Hall probe images containing partial vortices for a range of T_c in the $YBa_2Cu_3O_{6.375}$ crystal. (a) $T_c = 5.1$ K. (b) $T_c = 6.5$ K. (c) $T_c = 8.6$ K. (d) $T_c = 11.5$ K. (e) $T_c = 13.1$ K. (f) $T_c = 14.0$ K. (g) $T_c = 14.4$ K. For (a)-(d), $T \leq 2.4$ K; for (e)-(g), $T \leq 4.2$ K. In most of the images, the brightest (red) vortices are full vortices within experimental error, while those of smaller amplitude are identified as partial vortices.

was typically 3 K/min through the superconducting transition, since that was the rate the sample chamber cooled when the heater was turned off after warming the sample above T_c. Cooling ten times slower did not reduce the number of partial vortices. The images were typically taken after the applied field was turned off. Images before and after turning off the field at low temperature looked identical. As previous experience with these crystals has also showed, there are plenty of pinning sites in these crystals such that for low fields the vortices do not escape when the field is turned off. (It is typical to observe isolated pinned vortices in a field-cooled sample for most type II superconductors.) When the sample was cooled in zero field, no vortices (partial or full) were present. I also took images of partial vortices in other situations such as after cooling in fields with a large horizontal component, and after cycling the temperature to values near but below T_c. These data will be discussed below.

6.2.1 Properties

Many properties of the partial vortices can be deduced from my data. Partial vortices are seen only in crystals with low T_c. Previous imaging of near-optimally doped (T_c = 92 K) and Ortho-II (T_c = 60 K) YBCO crystals showed no partial vortices. They occur frequently for the lowest T_c's and are rare for $T_c \gtrsim 12$ K. The flux carried by the partial vortices is not limited to $\Phi_0/2$ or other small integer fractions, rather it seems to vary continuously. The frequency of occurrence and the flux carried by the partial vortices will be discussed quantitatively in Section 6.2.2.

Another observation is that partial vortices tend to occur in groups. This is an important property, because it is consistent with the idea that the partial vortices occur in a group that as a whole sum to one flux quantum. Partial vortices have been observed up to tens-of-microns away from other partial vortices within a group. Thus in cases where a partial vortex appears isolated, others might be nearby but not within the image area. The partial vortices usually have clear peaks, can have circular symmetry like a full vortex, or sometimes they are elongated or have a faint trail of flux (refer to Figure 6.3 for examples).

Partial vortices show a tendency to prefer certain regions of the crystal, even after

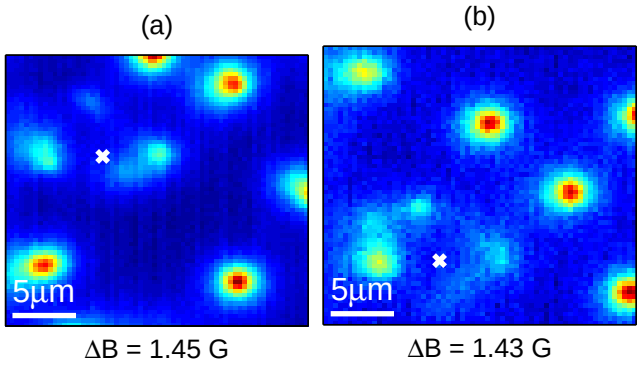

Figure 6.4: Partial vortices prefer certain locations even after annealing the sample at room temperature. (a) $T_c = 11.5$ K and $T = 2.2$ K. After six more days at room temperature, (b) $T_c = 13.1$ K and $T = 4.7$ K. Note the strikingly similar arrangement of partial vortices surrounding the $\times$ in each image. The $\times$'s likely mark the same spot on the sample, since a shift between the sample and probe is expected after room temperature thermal cycling. ΔB is the full scale of the colormap.

a room temperature anneal, as shown in Figure 6.4. This may indicate that partial vortices occur preferentially in regions of the sample with more disorder, more pinning sites, or weaker superconductivity.

Below I will show that partial vortices can be induced in the very underdoped YBCO by cooling in a horizontal field. Then I will discuss the tendency of partial vortices to move or coalesce when cycled to a higher temperature (below T_c) or with stick-slip coarse motion of the sample holder.

Effect of an in-plane field

While taking the partial vortex data in the $YBa_2Cu_3O_{6.375}$ crystal, we began to suspect that the observed partial vortices were segments of a full vortex that were displaced laterally. This idea is elaborated in Section 6.4. The different segments would be joined by an interlayer Josephson vortex. One test of this model is to cool the sample in a field with a strong horizontal component, because this should reduce the energy cost of displacing a vortex segment, making partial vortex formation more favorable.

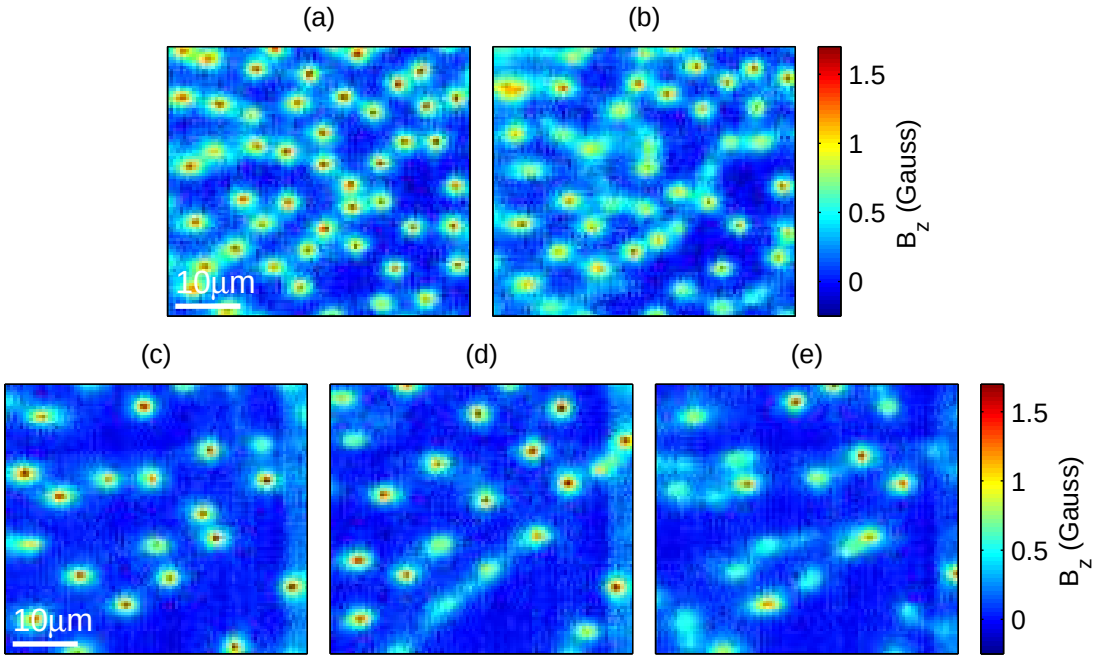

Figure 6.5: Effect of an in-plane field on partial vortex formation in YBCO. $T_c = 14.4$ K and $T = 4$ K for all the images. Field cooled through T_c in $B_z = 0.5$ G and (a) $B_x = 0$, (b) $B_x = 2.34$ G. Field cooled through T_c in $B_z = 0.2$ G and (c) $B_x = 0$, (d) $B_x = 1.17$ G, (e) $B_x = 2.34$ G. (The x-direction is horizontal and z is out of the page.)

With the crystal almost fully annealed at $T_c = 14.4$ K, I cooled the sample through T_c in an applied field with an in-plane component as well as a z component. Images taken after cooling in various B_x and B_z are shown in Figure 6.5. The vortex arrangement did not change if the fields were turned off after cooling. From left to right, the images show increasing amounts of partial vortices. Almost no partial vortices were present after cooling with $B_x = 0$, but increasing B_x by a couple of Gauss resulted in many partial vortices. The magnitude of B_z determined the density of flux observed in the images, as can be seen by comparing the top row of images ($B_z = 0.5$ G) to the bottom row ($B_z = 0.2$ G). Figure 6.5 clearly shows that partial vortex formation is indeed more favorable when the sample is field cooled with an in-plane component. The ratio of B_x to B_z, i.e. the angle between the applied field and the z-axis, may play a role in the probability of partial vortex formation.

Mobility

I found that partial vortices were much more mobile than full conventional vortices in the same samples. This was observed in two ways. One method showed that partial vortices moved around when the temperature was raised to $T < T_c$. Other observations with both the SQUID and Hall probe showed partial vortices which moved or coalesced when subjected to sample coarse motion. Both of these observations suggest that the partial vortices are less strongly pinned than full vortices.

To qualitatively compare the pinning strength of partial and full vortices, I raised the temperature and observed whether the vortices moved. This was done in a controlled manner as follows. The $YBa_2Cu_3O_{6.375}$ sample with $T_c = 14.4$ K was cooled to 3 K in a field $\vec{B} = 2\hat{x} + 0.25\hat{z}$ G. The large x-component was chosen to induce partial vortices. While at 3 K the applied field was turned off and no change in the vortex arrangement was observed. Then the sample was warmed up to $T = 6.6$ K, cooled back to 3 K, and imaged again. This cycle was repeated several times with successively higher maximum temperatures below T_c. After all cycles, the vortices had moved. The images are shown in Figure 6.6(a). Full vortices created by cooling through T_c in $\vec{B} = 0.25\hat{z}$ G did not show any motion after similar thermal cycling (Figure 6.6(b)).

Motion of partial vortices was also observed at times after stick-slip coarse motion of the sample holder in the z direction or the xy plane. Sometimes partial vortices appeared to coalesce. Figure 6.7 shows Hall probe images before and after several ramps of the voltage on the z piezo (to determine sample-probe separation) and slight z coarse motion towards the sample. Two partial vortices of approximately the same peak amplitude (shown circled) in the before image appeared to coalesce into one brighter vortex. The vortices are rather close to the left edge of the image, so it is possible that other flux outside the image area participated in the change and that these images do not show the full story. Nonetheless, the partial vortices definitely moved and probably coalesced due to the z motion.

Figure 6.8 shows SQUID images of a partial vortex that moved with respect to the sample and to stationary larger vortices when the sample was moved in the y direction with stick-slip coarse motion. [Image (a) in this figure is the same as Figure

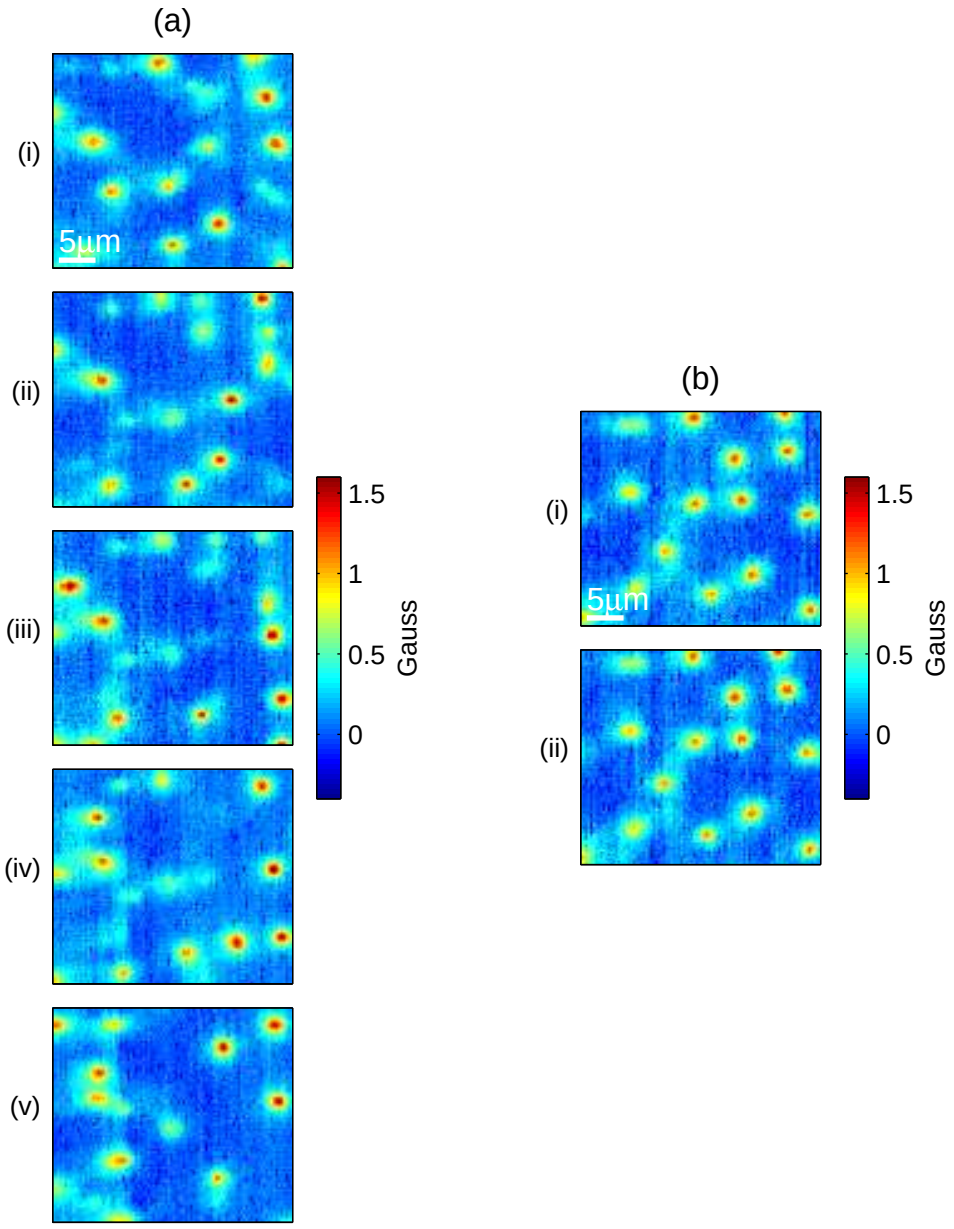

Figure 6.6: Comparison of thermal motion of partial vortices and full vortices. (a) YBCO sample cooled through $T_c = 14.4$ K in $B_x = 2$ G and $B_z = 0.25$ G to $T = 3$ K. Image (i) was taken after the fields were turned off. After thermal cycling sequentially to (ii) 6.6 K, (iii) 8.0 K, (iv) 9.8 K, and (v) 12.2 K. (b) The sample was cooled through T_c in $B_x = 0$ and $B_z = 0.25$ G to $T = 3$ K. Image (i) was taken after the fields were turned off. (ii) After thermal cycling to 11.8 K. All images were taken at $T = 3.0$ K.

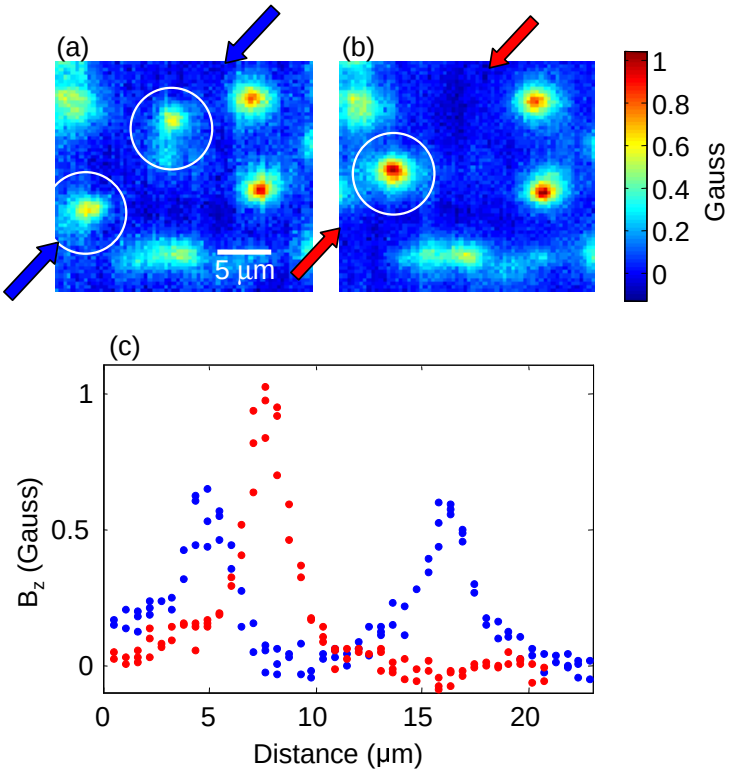

Figure 6.7: Partial vortices coalesced after sample coarse motion. (a) Hall probe image after cooling through $T_c = 8.6$ K in $B_z = 214$ mG applied field. Note the two partial vortices inside the white circles. (b) After several capacitance versus z ramps and slight z coarse motion towards the sample. Comparison of the images suggests that the two partial vortices in (a) collapsed to one full vortex in (b). (c) Cross-sections 2–3 pixels wide through images (a) and (b) as indicated by the arrows.

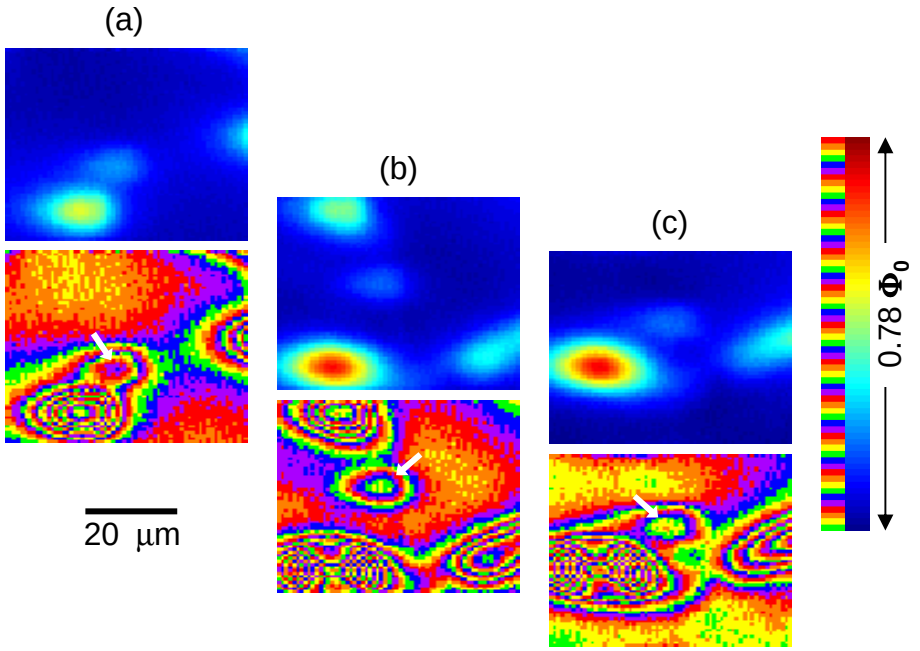

Figure 6.8: Motion of a partial vortex induced by xy coarse motion in a YBCO crystal with $T_c \approx 7$ K at $T = 2.6$ K. The upper and lower images are the same, just displayed with different colormaps to bring out all the features. The partial vortex of interest is indicated by the white arrows. Stick-slip sample coarse motion in the y direction was performed between images (a), (b) and (c), shifting the image area vertically as shown. Intermediate images were also taken but are not shown. The larger vortices remain stationary with respect to the sample while the partial vortex moved around. In (a) the brightest vortex carries flux Φ_0. This same vortex is seen again at the top left of (b). The brightest blob (red) in (b) and (c) are vortices that are too close to be spatially resolved by the 8 μm SQUID.

6.1(a)]. The partial vortex has approximately 40% the peak flux of the full vortex in (a). If this partial vortex is part of a group, it is not clear where the other members of the group are. The other partial flux might be outside the image area, or could be within the unresolved bright flux blob in images (b) and (c).

The motion of partial vortices during coarse motion of the sample holder could be due to stray fields created by the high voltage pulses required to induce the stick-slip motion. The stray fields might interact with the vortex fields creating forces on the vortices that are only large enough to unpin and move the partial vortices. The fact that partial vortices are mobile at temperatures quite below T_c and under the influence of sample coarse motion, while full vortices generally are not, shows that partial vortices are not as strongly pinned as full vortices.

6.2.2 Statistics

In this section I will give some statistics on the frequency of occurrence and magnitude of the partial vortices observed with the Hall probe in the $YBa_2Cu_3O_{6.375}$ crystal with varied T_c. The numbers presented here should be taken as indicators rather than statistically rigorous data for the following reasons: A finite number of images were taken at each T_c, the images covered a small area (maximum of 45×45 μm^2) and were taken over a small fraction of the crystal surface, and it was difficult to identify a very weak partial vortex or to distinguish a nearly full vortex from a full vortex especially at the lowest T_c where apparent vortex size was largest and inhomogeneous (Chapter 5). Nonetheless, two facts will be clear: (1) The percentage of partial vortices falls off, from >50% to just a few %, as T_c increases from 5 to 15 K. (2) The magnitude of the partial vortices varies continuously and does not seem limited to certain fractions.

From images at each T_c for the Hall probe YBCO sample, I counted the numbers of full vortices and partial vortices in unique images which were field cooled in an applied perpendicular field (B_z only). A partial vortex was taken to be any distinct blob of flux with an identifiable peak and a magnitude smaller than nearby full vortices. Vortices that I could not identify as clearly full or partial (a difficulty especially for the $T_c = 5.1$ K data) were left out of the count. Table 6.1 gives the results. Over

Table 6.1: Numbers of partial and full vortices observed in unique images at each T_c of the $YBa_2Cu_3O_{6.375}$ sample, where before each image the sample was field cooled in a perpendicular field ($B = B_z$). Ambiguous vortices and images were omitted.

T_c (K)	# images	# partial vortices	# full vortices	partial vortex %
5.1	7	17	11	61%
6.5	6	15	11	58%
8.6	7	23	10	70%
11.5	4	11	10	52%
13.1	13	18	44	29%
14.0	5	12	81	13%
14.4	6	6	106	5%
14.7	3	2	28	7%

100 partial vortices were observed in this sample. They accounted for more than half of all vortices imaged for $T_c \leq 11.5$ K, but dropped to less than 10% for T_c's above 14 K.

Secondly, I tabulated the fractions of a flux quantum (Φ/Φ_0) that the partial vortices appeared to carry. This was done roughly and with a few assumptions. The field profile of a conventional vortex simply scales with the total flux carried by the vortex:

$$B_z(r,z) = \frac{\Phi}{2\pi\lambda_{ab}^2}\int_0^\infty dq \frac{q\ J_0(qr)\ e^{-qz}}{q^2+\lambda_{ab}^{-2}+q\sqrt{q^2+\lambda_{ab}^{-2}}}, \tag{6.2}$$

where $\Phi = \Phi_0$ for a conventional vortex. Thus the flux fraction carried by a partial vortex can be estimated by simply comparing the peak B_z of a partial vortex to the peak of a nearby full vortex, with a few caveats. This peak comparison method assumes that the in-plane penetration depth (λ_{ab}) is the same at both the partial vortex and the full vortex locations. While this is a reasonable first assumption, perhaps partial vortices preferentially occur at regions with larger λ_{ab} (weaker superconductivity). A second caveat is the assumption that the partial vortices are indeed just miniature versions of a conventional full vortex, in other words that Equation (6.2) correctly describes the field profile of the partial vortices. We know that this cannot be a completely adequate description since some of the partial vortices (see Figure

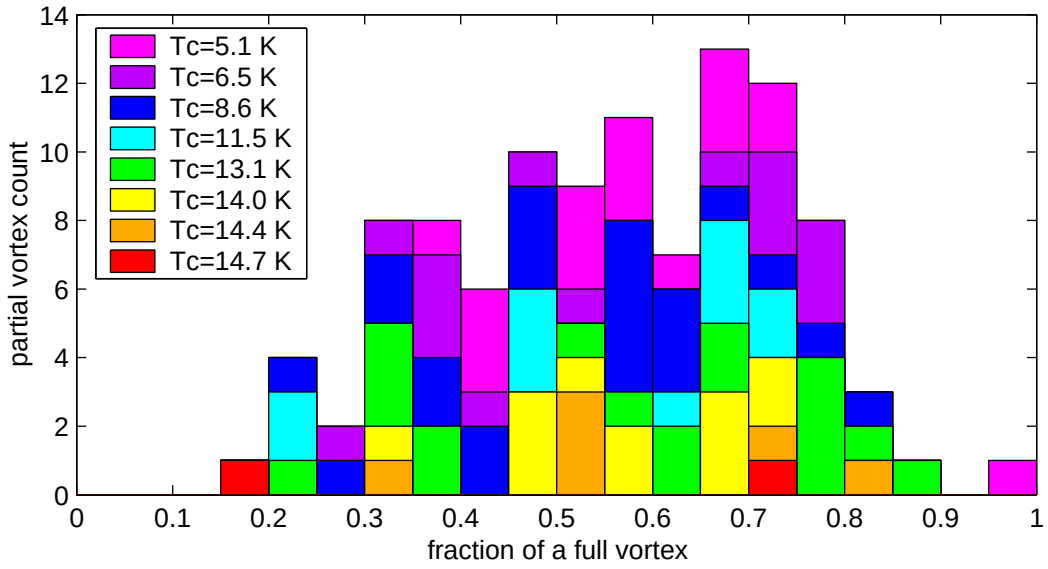

Figure 6.9: Histogram of partial vortex peak field as a fraction of full vortex peak. The total bar heights show the data from all T_c values, while the colors indicate specific T_c data.

6.3) are not circular. More importantly, as will be shown in Section 6.4.2, we believe the partial vortices are not just miniature vortices, instead the field is described by a slightly different equation. However, estimates of the flux fraction obtained by comparing peak heights is sufficient to show that the partial vortices occur for a range of magnitudes and are not quantized by some small-integer fraction. See the histogram in Figure 6.9.

There are also sources of error in measuring the peak height of vortices, and this translates to an error in the partial vortex peak height fractions. The measurement of a peak field is subject to noise in the data and error in background determination (there is a constant offset intrinsic to the Hall probe). The error in background determination and in peak signal for this method is roughly 50 mG each, which translates to a possible error in the peak fraction data of $\sim$5% at the high T_c values, and several times this for the lowest T_c. Counts may also be missing at the ends of the histogram, since a partial vortex with close to 100% of peak flux would likely be mistaken as a full vortex and those with very small peak flux may have been lost in the noise.

6.3 Thoughts and discussion

We considered many ideas in the process of determining what these partial vortices were before settling on the "split stack" scenario to be discussed in detail in Section 6.4. The ideas ranged from high frequency dynamics, to unconventional behavior of very small superfluid density, to grain boundaries, and to vortex termination below the surface.

One of the first ideas considered was that a group of partial vortices was actually just one full Φ_0 vortex that hopped between pinning sites on a time scale much faster than the measurement. The apparent fraction of Φ_0 carried by each partial vortex in a group would be equal to the fraction of time the full vortex spent at that pinning site. The time to take one SQUID image was typically 30–60 sec, with a time per pixel of $\sim$10 ms. No signature of hopping was seen in the images. For a more concrete test, we parked the SQUID over a partial vortex and recorded the flux through the SQUID pickup loop as a function of time. No fluctuations were observed below the 400 Hz roll off of the SQUID electronics. The hopping idea was discarded when the distances were considered. Partial vortices were often tens-of-microns apart, making it improbable that the vortex would only hop between a few pinning sites and never spend time at the many pinning sites in-between. Observations of vortex/anti-vortex pairs annihilating in these crystals (Gardner et al. 2002) showed that a pair, created $\sim$13 μm apart, would linger at intermediate pinning sites and/or rachet towards each other through the pinning landscape. This suggests that a hopping vortex would not spend time only at pinning sites tens-of-microns apart, but would also visit many intermediate sites, which would not result in quasi-isolated partial vortices.

Another idea involves unconventional behavior of the very small superfluid density (n_s/m^*) in these very underdoped samples. The following idea is from discussions with Nazario and Santiago. Flux quantization results from the fluxoid quantization condition in Equation (6.1) with $\mathbf{v}_s = 0$ far from the superconductor. In a well behaved superconductor, the current density $\mathbf{J}_s = 2en_s\mathbf{v}_s$ is zero far from a vortex because $\mathbf{v}_s = 0$ while $n_s > 0$. However, if n_s was zero, $\mathbf{J}_s$ could be zero with a non-zero value of $\mathbf{v}_s$. If the superfluid density vanished or had many fluctuating

zeros along the integration path, the second term (the $\mathbf{v}_s$ integral) in Equation (6.1) could be non-zero even far away from the vortex and the flux Φ could be less than the flux quantum. This idea requires unusual behavior of the superconductor with intermingled or wildly fluctuating "normal" ($n_s = 0$) and superconducting regions. It also does not account for grouping of partial vortices or for the full screening at low temperatures seen in Hall probe susceptibility data. Thus this idea is unlikely in light of other more promising scenarios for partial vortices.

The presence of grain boundaries in certain configurations can result in unquantized flux. This has been seen by Kirtley et al. (1995a) in optimally doped YBCO films that were grown on a patterned substrate such that grain boundaries enclosed hexagonal and triangular regions which had 45° rotations about the c-axis with respect to the rest of the film. The 45° rotation creates boundaries with both 0 and π junctions, since YBCO is a d-wave superconductor. The SQUID images from Kirtley et al. (1995a) show that the total flux through any of the closed grain boundaries defining a triangle or hexagon is an integer multiple of Φ_0, but flux of magnitude much less than Φ_0 is localized at different spots along the boundary. Spontaneous small unquantized flux has also been observed along the grain boundary of a YBCO film with a misalignment angle of 45° by Mannhart et al. (1996). They give a model for this flux stemming from the d-wave character of the order parameter and micro-facetting at the grain boundary plane. A more recent paper by Mints et al. (2002) reports images of *splintered* vortices along such a grain boundary, where several unquantized fluxes sum to Φ_0.

The unquantized flux in grain boundaries discussed above depends on misalignment angles other than 0° or 90° to give an additional π-shift to the phase as a result of d-wave symmetry. This is not an adequate model for our observations of partial vortices in the single crystals of YBCO, because there should not be any angles which result in a winding of π around a closed loop. The four-fold pattern of the d-wave order parameter is locked to the lattice. It could potentially rotate at a grain boundary (if there were one) by only 90°. Any closed loop crossing a 90° boundary would have to cross twice, resulting in a phase winding of 2π, not π. Thus even if our single crystal sample was granular (e. g. due to inhomogeneities in the superfluid density),

non-quantized flux could not arise by the same means as in the above experiments where 45° misalignments were present.

However, Kogan proposed that it could be possible even with no π junctions to have flux distributed over a closed boundary in sub-Φ_0 units. He worked out the flux division between arms of polygon shaped junctions (in particular for triangles) where none of the arms are π junctions. The ground state of the triangle with no π junctions has no magnetic flux. Kogan showed that if the one of the arms of a triangle with only 0 junctions had a different Josephson penetration depth than the other two arms, and if a total flux of Φ_0 was trapped in the triangle, the flux would split into two unequal parts. One part would reside on the arm with the different λ_J, and the other part would be on the other two arms. The magnitude of each part depends on the λ_J's. This could be generalized to a triangle with a different λ_J values for all three arms.

Kogan's idea could be plausibly applied to our single crystals as the mechanism for partial vortices if the samples had granularity resulting in closed junctions with unequal Josephson penetration depths. There is some evidence for inhomogeneity in the very underdoped $YBa_2Cu_3O_{6.375}$ sample. At the lowest measured T_c value of 5.1 K, the superconducting transition width was ∼3 K, more than twice the width at higher T_c. Also, the spread in apparent vortex shapes and sizes (Section 5.2.4) measured from different vortices at the lowest T_c suggests inhomogeneity. Even though there are not crystallographic grains in the single crystal samples, there might be grains of weaker and stronger superconductivity.

Another phenomenon that we considered is subsurface vortex termination. Mints et al. (2000) calculated that in a layered superconductor (like the cuprates) in the limit of no Josephson coupling between the layers, it is possible for a vortex to terminate in a layer below the surface and channel at least part of the flux out parallel to the layers. The energy cost of subsurface termination increases with sample size, but they show that for sample size below $R_c \sim \kappa\lambda_{ab}$ (where $\kappa = \lambda_{ab}/\xi_{ab}$), subsurface termination becomes energetically favorable. The coherence length ξ_{ab} is not known for our very underdoped YBCO crystals, but if we assume the optimally doped value $\kappa \sim 5$, R_c could be about 5 μm. Our samples are of order 1 mm, but Mints et al.

(2000) suggest that if a sample has defects spaced by R_c, subsurface termination could also occur. The flux of a vortex terminated under the surface would not all exit through the surface and could look like a partial vortex. Subsurface termination is the same concept as the split pancake vortex stack that I will introduce in the next section. The split stack extends the subsurface termination idea to naturally explain groups of partial vortices and their increased occurrence when cooled in an in-plane field.

6.4 Partial vortices as split pancake vortex stacks

In this section I will present the idea of split pancake vortex stacks as the explanation for the observed "partial vortices" in very underdoped $YBa_2Cu_3O_{6+x}$. First I review the concept of pancake vortices, introduced by Clem (1991), as the building blocks of a 3D vortex in a layered superconductor. Then I introduce the idea of a split stack. I give mathematical formulas for the magnetic field from a partial stack and show via calculations that a split stack does result in features that look like the partial vortices. I discuss fits of the model to partial vortex data and show that this explanation indeed fits the data. Finally, I give further support for the split pancake vortex stacks in light of the large anisotropy of the crystals and qualitative agreement with the observed properties of the partial vortices.

6.4.1 Introduction to pancake vortices

Clem (1991) introduced the idea of 2D pancake vortices as the basic building blocks of 3D vortices in layered superconductors in the limit of zero Josephson coupling between the layers. This is an appropriate limit for the very underdoped $YBa_2Cu_3O_{6+x}$ ($x \approx 0.35 - 0.375$) studied here because $\lambda_c \gg \lambda_{ab}$, indicating that the maximum Josephson supercurrent density between the layers is very small. The in-plane penetration depth, λ_{ab}, is the exponential decay length scale of supercurrent flowing in the plane, while λ_c is the decay length for supercurrent flowing perpendicular to the planes. In Chapter 5 I made measurements of the apparent vortex size "s_{ab}" in

$YBa_2Cu_3O_{6.375}$ which gives an upper bound on λ_{ab}. The results showed $s_{ab}(T \ll T_c)$ ranging from roughly 0.5 to several microns for T_c ranging from 5–15 K, where the vortex size decreased with increasing T_c. In contrast, measurements of λ_c in similar samples by Hosseini et al. (2003) gave much larger values: $\lambda_c(0) \approx 100$ μm for $T_c \approx 6$ K, and $\lambda_c(0) \approx 40$ μm for $T_c \approx 15$ K. Thus the anisotropy parameter λ_c/λ_{ab} in our very underdoped YBCO is large, with lower bound in the range 40–80, so the approximation of zero Josephson coupling ($\lambda_c \to \infty$) is appropriate for this system.

Clem (1991) begins his discussion by first reviewing the field and current density from one pancake vortex (carrying flux Φ_0) in an isolated superconducting layer with thickness $d \ll \lambda_{\rm bulk}$. The vector potential is

$$a_\phi(r,z) = \frac{\Phi_0}{2\pi} \int_0^\infty dq \frac{J_1(qr)\, e^{-q|z|}}{1+q\Lambda}. \tag{6.3}$$

Here r is the radial distance from the pancake center, z is the distance from the layer plane, J_1 is the first-order Bessel function, and $\Lambda = 2\lambda_{\rm bulk}^2/d$ is the 2D screening length in the layer. The magnetic field can be found simply from $\mathbf{B} = \nabla \times \mathbf{a}$.

If other superconducting layers are present, they act to screen the magnetic field from the single pancake. Clem (1991) calculated the field from a pancake in a single layer at $z = 0$ which is surrounded by an infinite number of other layers above and below with layer spacing s (which would be the c-axis unit cell dimension in YBCO). In situations where r and z are much larger than s, the discreteness of the layers can be ignored and (in the zero Josephson coupling limit) the vector potential is

$$a_\phi(r,z) = \frac{\Phi_0 \lambda_{ab}}{2\pi\Lambda r} \left(e^{-|z|/\lambda_{ab}} - e^{-\sqrt{r^2+z^2}/\lambda_{ab}} \right). \tag{6.4}$$

From this the magnetic field can be calculated. The field is channelled away from the pancake parallel to the layers and decays on the length scale λ_{ab} perpendicular to the layers. Since $\lambda_{ab} \gg s$, the field does extend across many layers but is completely screened out beyond a few λ_{ab} in the z-direction. The field is such that two pancakes in the same layer experience a repulsive interaction which is logarithmic for all distances, but two pancake vortices in different layers experience a weak magnetic attraction

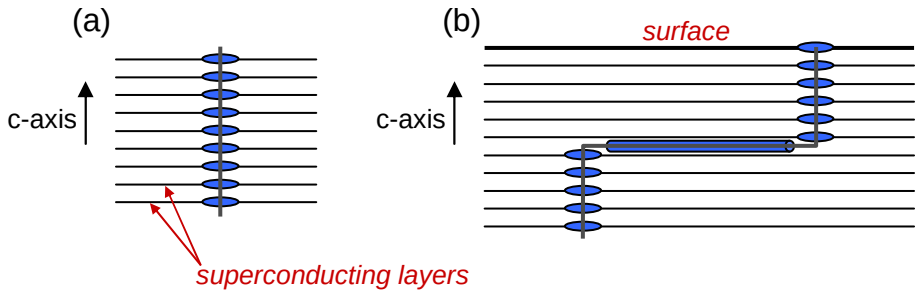

Figure 6.10: (a) Illustration of a vortex built from 2D pancake vortices. A pancake resides in each layer which are spaced a distance s. (b) Schematic of a split pancake vortex stack. Observed from above, the partial stacks would look like isolated "partial vortices". The horizontal component joining the two partial stacks is an interlayer Josephson vortex.

which favors alignment in z (a pancake stack, as illustrated in Figure 6.10(a)). A non-zero Josephson coupling would add an additional attractive force.

The total field from many pancake vortices in a system of infinite superconducting layers can be found from the superposition of Clem's general vector potential for one vortex in a system of infinite layers (which I've shown in Equation (6.4) only for the particular limit of small s). Clem shows that a straight stack of 2D pancake vortices, as shown in Figure 6.10(a), gives the same result as the anisotropic London model for a 3D vortex. He also calculates the energy of a tilted stack and the thermal energy required to distort a stack (Clem 1991).

6.4.2 Split pancake stacks

We propose that our observed partial vortices are the top view of partial stacks of pancake vortices resulting from a split stack. Instead of a stack of 2D pancake vortices aligned along a single axis in the z-direction, as is favored by pure magnetic interactions and also by weak Josephson coupling, we propose that other energy considerations such as pinning make it favorable (as least as local energy minima) to have the stack split one or more times into partial stacks separated laterally. The partial stacks would be joined by an interlayer Josephson vortex (where the Josephson coupling is weak). This picture is schematically shown in Figure 6.10(b). In a top

view of the magnetic field, each partial stack that is within a few λ_{ab} of the surface would appear as an isolated partial vortex with apparent flux less than Φ_0. Whether or not the stack is split, the 3D vortex would always come all the way through the sample having one pancake per layer. This explains why the partial vortices always appear in groups.

The split stack or "kinked structure" was first proposed by Benkraouda and Clem (1996) as an alternative to a tilted stack. They calculated and compared the energy of a tilted pancake vortex stack to that of a split stack in the limit of zero Josephson coupling ($\lambda_c \to 0$), with the very top and bottom pancakes pinned. Their calculations showed that the line tension of a tilted stack is negative for a tilt angle greater than 52° measured from the z-axis, and thus the tilted stack is unstable for large angles. Even for angles less than 52°, they showed that the split stack has lower energy than a tilted stack for angles greater than ∼5° for stacks containing many pancakes.

An observation of a split pancake vortex stack has been reported by Grigorenko et al. (2002) in $Bi_2Sr_2CaCu_2O_{8+\delta}$ with $T_c = 90$ K. The split stack in this case was formed under dynamic conditions and was a rare observation. The primary focus of their paper was to discuss observations of interacting lattices of pancake vortex stacks and Josephson (interlayer) vortices. Their observed split (or "fractional") pancake stack formed from an aligned stack after the in-plane applied field was suddenly reduced from 36 Oe to zero. They fit their Hall probe image and obtained ∼0.48 μm as the depth of the splitting. The stack split a lateral distance of 2.3 μm. Raising the in-plane field to 11 Oe "healed" the split stack back to a straight stack.

Our partial vortex observations differ from that of Grigorenko et al. (2002) in BSSCO, in that partial vortices were quite prevalent in the very underdoped YBCO, especially for very low T_c. Special dynamic situations were not required to produce partial vortices in the YBCO. They were created simply by field cooling, even in nominally zero in-plane field. To our knowledge, our partial vortex observations are the first observation of stable frequently occurring split pancake vortex stacks. The work by Grigorenko et al. (2002) was performed on optimally doped BSSCO, so it is quite plausible that imaging studies of BSSCO with lower doping might reveal similar vortex behavior as in the very underdoped YBCO. This would require improvements

in the growth of underdoped BSSCO.

Below I will give a mathematical description of the field from partial pancake vortex stacks, based largely on Clem (1991) and further calculations by Bluhm. I will also show that the split stack model does produce features consistent with the partial vortex observations and in Section 6.4.3 I will present a fit to a partial vortex image.

Mathematical description

Expressions can be found for the magnetic field of a partial stack of pancake vortices (Clem 1994). Since these expressions are desired here for modelling the Hall probe images of partial vortices, I consider the situation where a layered superconductor fills a half-space $z < 0$ with vacuum for $z > 0$. I will consider the results in the limits $\lambda_{ab} \gg s$ and $z \gg s$ since the formulas simplify nicely in that case and these experiment were done strongly in that limit. In YBCO $s = 11.7$ Å, our vortex fits suggest λ_{ab} may be greater than 0.5 μm in these YBCO samples, and the field measured by the Hall probe was always at $z \geq 0.4$ μm due to constraints of the sample-probe alignment.

For a single 2D pancake vortex in the layer at z_n in a superconductor occupying all space, Clem (1991) gave the vector potential

$$a_\phi(r,z) = \int_0^\infty dq A(q) J_1(qr) Z(q,z) \tag{6.5}$$

with

$$A(q) = \frac{\phi_0}{2\pi} \frac{1}{\sqrt{1 + 2q\Lambda \coth qs + (q\Lambda)^2}} \quad \xrightarrow{s\to 0} \quad A(q) \approx \frac{\phi_0}{2\pi\Lambda} \frac{1}{\sqrt{q^2 + \lambda_{ab}^{-2}}} \tag{6.6}$$

and $Z(q,z)$ is given in full form in Clem (1991), and in the limit of $s \to 0$, a good approximation is $Z(q,z) = \exp\left[-Q|z - z_n|\right]$ with $Q = \sqrt{q^2 + \lambda_{ab}^{-2}}$. The above equations were all in the case of an infinite superconductor.

Now I will summarize the case of a superconducting half-space as done by Bluhm.

In vacuum ($z > 0$), the vector potential is

$$a_\phi(r,z) = \int_0^\infty dq \tilde{A}(q) J_1(qr) e^{-qz}. \tag{6.7}$$

By considering the boundary conditions at the $z = 0$ superconductor/vacuum interface, Bluhm found an expression for $Z(z,q)$ to be inserted into Equation (6.5) which gives the vector potential for both inside and outside the superconductor:

$$Z(z,q) = \begin{cases} \frac{2Q}{Q+q} e^{Qz_n} e^{-qz} & (z > 0) \\ e^{-Q|z-z_n|} + \frac{q-Q}{Q+q} e^{Qz_n} e^{Qz} & (z < 0) \end{cases} \tag{6.8}$$

where Q is give by the expression (Clem 1991)

$$\cosh Qs = \cosh qs + (q\Lambda)^{-1} \sinh qs \quad \xrightarrow{s\to 0} \quad Q = \sqrt{q^2 + \lambda_{ab}^{-2}}. \tag{6.9}$$

By summing the contributions of all pancake vortices within a finite stack, the vector potential of a partial stack can be found. For a partial straight stack extending from $z_n = -ns$ to $z_m = -ms$, the vector potential for $z > 0$ is (Bluhm):

$$\begin{aligned} a_\phi(r,z) &= \int_0^\infty dq A(q) J_1(qr) \frac{2Q}{Q+q} e^{-qz} \sum_{j=n}^{m} e^{-Qjs} && (6.10) \\ &= \frac{1}{s} \int_0^\infty dq A(q) J_1(qr) \frac{2}{Q+q} e^{-qz} \left(e^{-Qns} - e^{-Qms} \right) && (6.11) \\ &\approx \frac{\Phi_0}{2\pi\lambda_{ab}^2} \int_0^\infty dq \frac{e^{-qz} J_1(qr)}{q\sqrt{q^2 + \lambda_{ab}^{-2}} + q^2 + \lambda_{ab}^{-2}} \left(e^{Qz_n} - e^{Qz_m} \right) && (6.12) \end{aligned}$$

where the sum is replaced by an integral in the first step, and in the last step substitutions are made for $A(q)$ and Q in the $s \to 0$ limit (Equations 6.6 and 6.9). The equality $\lambda_{ab}^2 = s\Lambda/2$ was also used.

The magnetic field can easily be found from $\mathbf{B} = \nabla \times \mathbf{a}$, giving the z-component $B_z = \frac{1}{r}\frac{\partial}{\partial r}(r a_\phi)$:

$$B_z(r,z) = \frac{\Phi_0}{2\pi\lambda_{ab}^2} \int_0^\infty dq \frac{q\ e^{-qz}\ J_0(qr)}{Q(Q+q)} \left(e^{Qz_n} - e^{Qz_m} \right), \tag{6.13}$$

where $Q = \sqrt{q^2 + \lambda_{ab}^{-2}}$ if conventional units are used in the integral, or alternatively $Q = \sqrt{q^2 + 1}$ if r, the z's, and q are in units of λ_{ab} (inverse λ_{ab} for q) in the integrand. The partial stack begins at a depth z_m in the superconductor and terminates at z_n. Since the stack begins and ends within the superconductor, $-\infty \leq z_m < z_n \leq 0$. Note that if the partial stack extends from $z_m = -\infty$ to $z_n = 0$, Equation (6.13) becomes simply that of a conventional 3D vortex described by Equation (6.2) with $\Phi = \Phi_0$.

The total flux through the top of the crystal resulting from a partial stack can also be calculated. Clem (1994) gives expressions for the total flux through the top and bottom of a finite crystal from a single pancake vortex. By integrating over all pancake vortices in a partial stack, we obtain for the total flux through the $z = 0$ surface of a superconducting half space for a partial vortex extending from z_m to z_n $(z_m < z_n \leq 0)$

$$\Phi = \Phi_0 \left(e^{z_n/\lambda_{ab}} - e^{z_m/\lambda_{ab}} \right). \tag{6.14}$$

It is easily see that if a straight complete vortex stack ($-\infty$ to 0) splits once at a depth $z = -d$, the total flux through the surface from the lower partial stack is $\Phi_{\text{lower}} = \Phi_0 e^{-d/\lambda_{ab}}$ while the flux from the upper partial stack is $\Phi_{\text{upper}} = \Phi_0 \left(1 - e^{-d/\lambda_{ab}}\right) = \Phi_0 - \Phi_{\text{lower}}$. The sum of the flux from each segment of the stack is Φ_0 as expected. Notice that if d is greater than several penetration depths, a negligible amount of flux from the lower partial stack will be observed and the upper partial stack looks just like a full pancake vortex stack with a full flux quantum.

In this split stack proposal for the partial vortices, it should be emphasized that these features are "partial" vortices only in the sense that a full flux quantum does not exit through the surface from one lone partial vortex, even though each 2D pancake vortex in a layer carries Φ_0. Thus there is not some topological funny business going on creating a "fractional" vortex and violating flux quantization. The unique feature observed here is a lateral displacement of part of a vortex, best described in the 2D pancake vortex formulation, and only possible in highly anisotropic crystals.

Model split stacks

To get a sense of what a split stack looks like, I generated B_z images from Equation (6.13) in the case of a straight full stack which splits once at $z = -d$ for several different $d > 0$ depth values. For these calculations I set the height above the sample to be $z = 0.8\lambda_{ab}$, which if $\lambda_{ab} \approx 1$, is a reasonable value for the sample-probe height. Figure 6.11 shows the calculated images for a split pancake vortex stack for several values of split depth d. Cross sections through the field profiles of split vortices as a function of d are shown in Figure 6.12. If d is a few or more times the penetration depth λ_{ab}, only the upper partial stack is seen and its field profile looks like that of a full vortex. This is because the field from pancakes deep in the sample are completely screened. A group of N partial vortices could be modelled simply by letting the pancake vortex stack split $N - 1$ times at varying depths.

One thing that is easily seen from Equation (6.13) is that if the magnetic field from all the partial vortices of one group is superimposed, the sum of the fields is identical to the field profile of a full vortex, assuming the penetration depth λ_{ab} is the same at the location of each partial stack. A simplified version of this statement is that the peak amplitudes of partial vortex stacks within one group should equal the peak amplitude of a full vortex. This is a quick way to identify a partial vortex group in the Hall probe images. Another feature worthy of mention is that, at least for a stack with one split, the B_z from the lower partial stack is more spread out (has a larger normalized FWHM) than from the upper stack, when compared at constant $z > 0$. This can be seen in Figure 6.12 where the partial vortex on the left side is the lower one. These two features – the sum of the partial vortex fields add to a full vortex, and the lower partial vortex is more spread out – are helpful in analyzing the partial vortex data.

6.4.3 Fitting the data

Now I will discuss a fit to a pair of partial vortices to show that the split pancake stack model is quite consistent with the data.

The image in Figure 6.13(a) shows three uniform full vortices (brightest) and

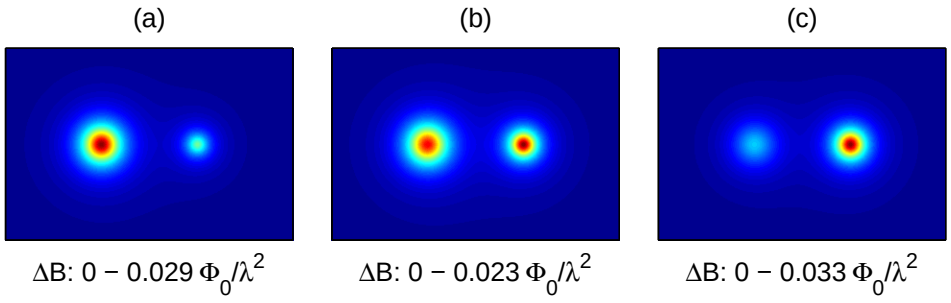

Figure 6.11: Calculated $B_z(x, y)$ from a split pancake vortex stack separated by a distance $10\lambda_{ab}$ in the x-direction. The left stack extends in z from $-\infty$ to d and the right one from d to the surface ($z = 0$). (a) $d = \lambda_{ab}/4$ and the flux through the surface from the left (the lower) stack is $\Phi_L = 0.78\ \Phi_0$. (b) $d = \lambda_{ab}/2$ and $\Phi_L = 0.61\ \Phi_0$. (c) $d = \lambda_{ab}$ and $\Phi_L = 0.37\ \Phi_0$. For these calculations, B_z was computed with $z = 0.8\lambda_{ab}$.

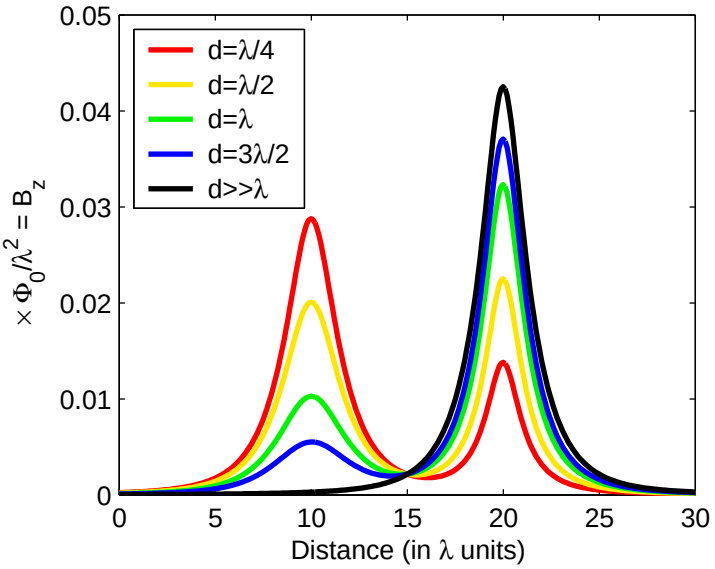

Figure 6.12: Cross sections through the centers of calculated split vortices shown in Figure 6.11 and also other values of split depth d. The left peak is from lower section of the split stack extending in z from $-\infty$ to d and the right one from the upper section from d to 0.

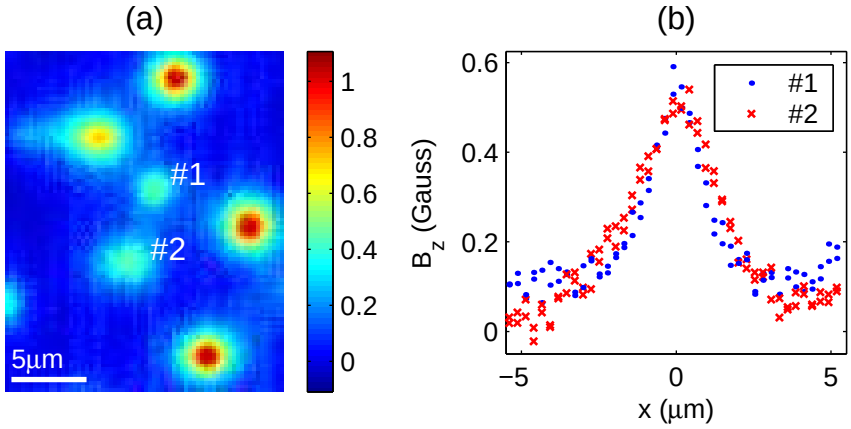

Figure 6.13: A partial vortex pair in $YBa_2Cu_3O_{6.375}$ with $T_c = 14.0$ K and $T = 4$ K. (a) Hall probe image containing a split pancake vortex stack that appears as two partial vortices labelled #1 and #2. The three brightest vortices in the image are full (unsplit) vortices. A constant background determined from fits to the full vortices has been subtracted. (b) Horizontal cross sections through the two partial vortices. Partial vortex #1 has both a higher peak and a smaller width than #2, indicating that #1 is the upper partial stack and #2 is the lower.

three clearly defined partial vortices. This image was taken with the scanning Hall probe in the single crystal $YBa_2Cu_3O_{6.375}$ with $T_c = 14.0$ K at low temperature. The sample had been cooled in an applied field $B_z = 0.2$ G. At this T_c partial vortices are rare ($< 15\%$ of all vortices observed). These partial vortices occurred at a site that produced partial vortices, of various arrangement, after several cycles through T_c.

As discussed above, the sum of B_z from each partial vortex within a single group should add to a full vortex. A quick comparison of peak height shows that the partial vortices labelled #1 and #2 are likely one group – that is they result from one pancake vortex stack with one split. The third brighter partial vortex in the upper left could not be in a group with #1 or #2 because its peak height is too large. Notice that this third partial vortex appears elongated to the left, suggesting that there are several splittings which result in a small amount of flux through the top surface in addition to the main peak.

Figure 6.13(b) shows horizontal cross sections through the centers of partial vortices #1 and #2. Partial #1 has a higher peak *and* a narrower width than #2. Thus

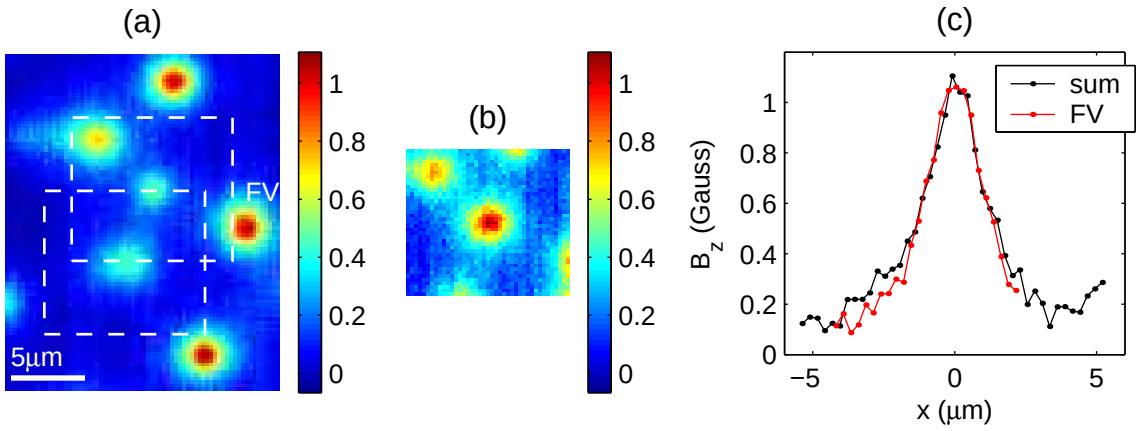

Figure 6.14: Partial vortices sum to a full vortex. (a) Image with partial and full vortices. A constant background determined from a fit to the full vortex labelled "FV" has been subtracted from the image. (b) Sum of the image areas inside the two boxes in (a). This sum of the two partial vortices looks similar to the full vortex field profiles in (a). Note: The partial vortices are only 5 microns apart, so there is some field contributions from each at the site of the other, offsetting the effective background in (b). (c) Horizontal cross sections through the sum of partials shown in (b) and the full vortex (FV) in image (a).

without even normalizing the peak heights to compare the FWHM, it is clear that #2 is the lower partial stack (from $z = -\infty$ to $-d$) and #1 is the upper (from $z = -d$ to 0). The goal in analyzing and fitting this pair of partial vortices is to show that the split stack model describes the data well and to determine the depth d of the split.

Another test to check that partials vortices #1 and #2 are likely from one split pancake vortex stack is to add the field profiles together to create a superimposed image. This is shown in Figure 6.14. In (a), the zero has been set by subtracting a constant background field determined from a fit to the full vortex labelled "FV". The image area within the boxes centered on each partial vortex were summed pixel by pixel and the sum is shown in (b). Note that sum of the partials looks similar to the full vortices as expected. This can also be seen in (c) where cross-sections through the summed vortex and a full vortex are compared. One thing to mention is that because the partial vortices are close to each other and to other vortices, there is some field contribution from other vortices. Thus the summed vortex shown in (b)

could have an effective background different from the true background in (a), due to flux from nearby features.

To fit the partial vortex group of #1 and #2, we need to use Equation (6.13). Integration over the Hall probe area ($< 0.5 \times 0.5\ \mu\mathrm{m}^2$) is ignored, since this complicates the calculations and was shown in fits in Chapter 5 to make little difference. For the upper and lower vortices Equation (6.13) becomes

$$B_z^{\mathrm{upper}}(r_1, z) = \frac{\Phi_0}{2\pi\lambda_{ab}^2} \int_0^\infty dq \frac{q\ e^{-qz}\ J_0(qr_1)}{q^2 + \lambda_{ab}^2 + q\sqrt{q^2+\lambda_{ab}^2}} \left(1 - e^{-d\sqrt{q^2+\lambda_{ab}^2}}\right) \quad (6.15)$$

$$B_z^{\mathrm{lower}}(r_2, z) = \frac{\Phi_0}{2\pi\lambda_{ab}^2} \int_0^\infty dq \frac{q\ e^{-qz}\ J_0(qr_2)}{q^2 + \lambda_{ab}^2 + q\sqrt{q^2+\lambda_{ab}^2}} \left(e^{-d\sqrt{q^2+\lambda_{ab}^2}}\right) \quad (6.16)$$

where d is the depth of the split and r_1 and r_2 are the distances from the axes of the upper and lower partial vortex stacks respectively. Ideally we would fit the partial vortices using fit parameters z, λ_{ab}, d, the center xy locations, and a constant background. However, as was discussed in Chapter 5, z and λ_{ab} are highly correlated in these field profile equations and cannot reliably be fit simultaneously. Also, Equations (6.15) and (6.16) cannot be solved analytically. The numerical approach I used for fitting for the penetration depth of full vortices detailed in Appendix A would be quite time intensive with both λ_{ab} and d as free parameters. So instead I first determined λ_{ab} and then did the full fit to find d.

In Chapter 5 I performed extensive fitting of the vortices in an attempt to measure the in-plane penetration depth. Because we could not tell if the pancake vortices making up the full vortices where aligned, or instead staggered by pinning, we were conservative and said that we measured the apparent vortex size which would equal λ_{ab} if the pancake stack was fully aligned, but would be larger than λ_{ab} if the pancakes were staggered. In this chapter, when I refer to fitting λ_{ab}, it can instead be interpreted as fitting the apparent vortex size. This distinction should not affect the fitting of the partial vortices if the degree broadening of the apparent vortex size is similar for all vortices.

I used the same fitting method as in Chapter 5 (including integration over the Hall probe area) to fit the full vortices in Figure 6.14(a) and the sum of the partials

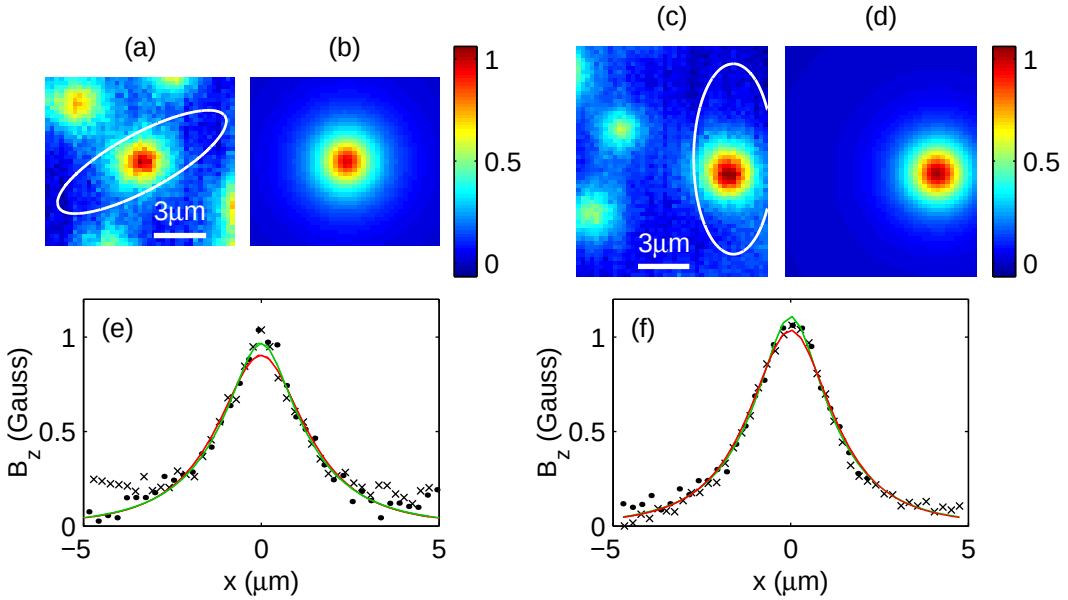

Figure 6.15: Penetration depth fits. (a) Sum of the partial vortices (same data as Figure 6.14(b)). A constant background determined from a fit to *this* vortex has been subtracted. (b) Fit to data within the ellipse in (a) with z fixed at 0.6 μm and best fit $\lambda_{ab} = 1.11$ μm. (c) Image of a full vortex to the right of the partial vortices. (d) Fit to the full vortex within the ellipse in (c) with z fixed at 1.0 μm and best fit $\lambda_{ab} = 0.65$ μm. (e) and (f) Horizontal (•) and vertical (×) cross sections through the data and fits for the sum of partials and the full vortex respectively. Green line are the fits with $z = 0.6$ μm, in (e) best fit $\lambda_{ab} = 1.11$ μm, in (f) best fit $\lambda_{ab} = 0.99$ μm. Red lines are the fits with $z = 1.0$ μm, in (e) best fit $\lambda_{ab} = 0.76$ μm, in (f) best fit $\lambda_{ab} = 0.65$ μm.

in Figure 6.14(b). The height $z = z_0 + \Delta z$ above the sample is difficult to determine because z_0, the minimum sample-probe distance, depends sensitively on the alignment. For this image $\Delta z \approx 0.21$ μm. I did several penetration depth fits to the sum of partials shown in Figure 6.15(a) and the full vortex shown in (c) of the same figure. A typical value for z_0 based on past measurements of samples with known penetration depth is $z_0 \lesssim 0.8$ μm. Geometric constraints impose a lower bound of $z_0 \geq 0.4$ μm. I did three fits to the vortices in (a) and (c): with $z = 1.0$ μm, with z as a free fit parameter, and with $z = 0.6$ μm. Free parameters were the in-plane penetration depth, the vortex center, and a constant background. For the sum of partials these three fits gave $\lambda_{ab} = 0.76$ μm for $z = 1.0$ μm, $\lambda_{ab} = 1.20$ μm and $z = 0.51$ μm for

the free z fit, and $\lambda_{ab} = 1.11$ μm for the $z = 0.6$ μm fit. For the full vortex in (c) the results were $\lambda_{ab} = 0.65$ μm, $\lambda_{ab} = 0.95$ μm and $z = 0.65$ μm, and $\lambda_{ab} = 0.99$ μm. Fits to the other two full vortices gave similar results as the fits to this full vortex. The fits with free z and λ_{ab} should not be trusted, as the correlation between z and λ_{ab}^{-1} was greater than 0.97, and fits to other vortices at other T_c did not produce consistent z_0 values, even though z_0 is expected to have been the same for all measurements on this crystal. Nevertheless, the free z fits encouraged me to do the fits with z at the minimum possible value of $z = 0.6$ μm.

Results of the lambda fits are shown in Figure 6.15. Image (b) is the fit to (a) with $z = 0.6$ μm, and (d) is the fit to (c) with $z = 1.0$ μm. Cross sections of the data and fits are shown in (e) and (f) with both the $z = 0.6$ μm fit and $z = 1.0$ μm fit. The fit with $z = 0.6$ μm appears to fit the peak of the summed vortex best, while $z = 1.0$ μm is perhaps the better fit to the peak for the full vortex. For fixed z, the fitted penetration depth is larger by ≈ 0.12 μm for the summed vortex than for the full vortex. This could indicate that the partial vortices formed at a location of weaker superconductivity (smaller superfluid density $n_s \propto \lambda^{-2}$). Or that there are some systematic effects skewing the fitted value for the summed vortex. The partial vortices were summed pixel by pixel, so the centers could not be aligned perfectly. Fitted centers of the partial vortices #1 and #2 show that for the sum the centers were misaligned by ≤ 0.04 μm, which could contribute to a slightly larger penetration depth fit. Also, the background could contribute to an error in λ_{ab}, for aside from z, the background constant is the free parameter most correlated with λ_{ab}. For the summed vortex the correlation between λ_{ab}^{-1} and the background constant was between -0.53 and -0.57, and for the full vortex between -0.39 and -0.46. So the penetration depth and the background were not completely independent parameters. The nearby flux for the summed vortex could have skewed the fit into choosing a somewhat larger λ_{ab}. In any case, this is all to say that for a chosen z we could either assume that the penetration depth for the partial vortex stacks is that of the fit to the summed partials, or is that of the full vortex. I will present a partial vortex fit done both ways.

I fit the partial vortices #1 and #2 from Figure 6.13(a) simultaneously to Equations (6.15) and (6.16). Fixed parameters in the fit were z and λ_{ab}, while free fit parameters were the splitting depth d, the center locations of both partial vortices, and a constant background. The fitting method is similar to that described in Appendix A.2. I performed the fit twice. Once with $z = 0.6$ μm and $\lambda_{ab} = 1.11$ μm, which are the values for the better-looking penetration depth fit to the summed vortex in Figure 6.15. The fit with these input parameters gave splitting depth $d = 0.53$ μm $= 0.48\lambda_{ab}$. The second fit was with $z = 1.0$ μm and $\lambda_{ab} = 0.64$ μm, where are approximately the best looking fit values for the full vortex. This fit to the partials gave $d = 0.36$ μm $= 0.56\lambda_{ab}$. The fitting results are shown in Figure 6.16. Both fits do a good job of modelling the data. Further trials over an array of z and λ_{ab} might produce even better fits. However, the goal here of showing that the partial vortices are indeed described by a split stack has been accomplished, and an approximate split depth of $0.5\lambda_{ab}$ for this partial vortex group has been determined. It is clear from the fitting that the partial vortices can be modelled very well as split stacks of pancake vortices.

This partial vortex pair was ideal for fitting because there were only two of them and they were well defined. In many of the other images shown earlier in this chapter, split stack modelling would be more complicated. Modelling becomes more difficult when there are several splits of a single stack and when several groups of partial vortices are nearby making it difficult to determine which partial belongs to which group. Some partials appear elongated or have tails which could be the result of many nearby splits that are unresolved by the Hall probe, or possibly tilts of a pancake stack.

6.4.4 Discussion

The explanation of the partial vortices as split stacks (with one or more splits) is logical for these very underdoped $YBa_2Cu_3O_{6+x}$ crystals because the anisotropy factor is very large ($\gamma = \lambda_c/\lambda_{ab} > 40$). High anisotropy means that the Josephson coupling between the layers is very weak so the coupling of pancake vortices is almost only due to magnetic coupling, making it easier to separate them laterally. With no

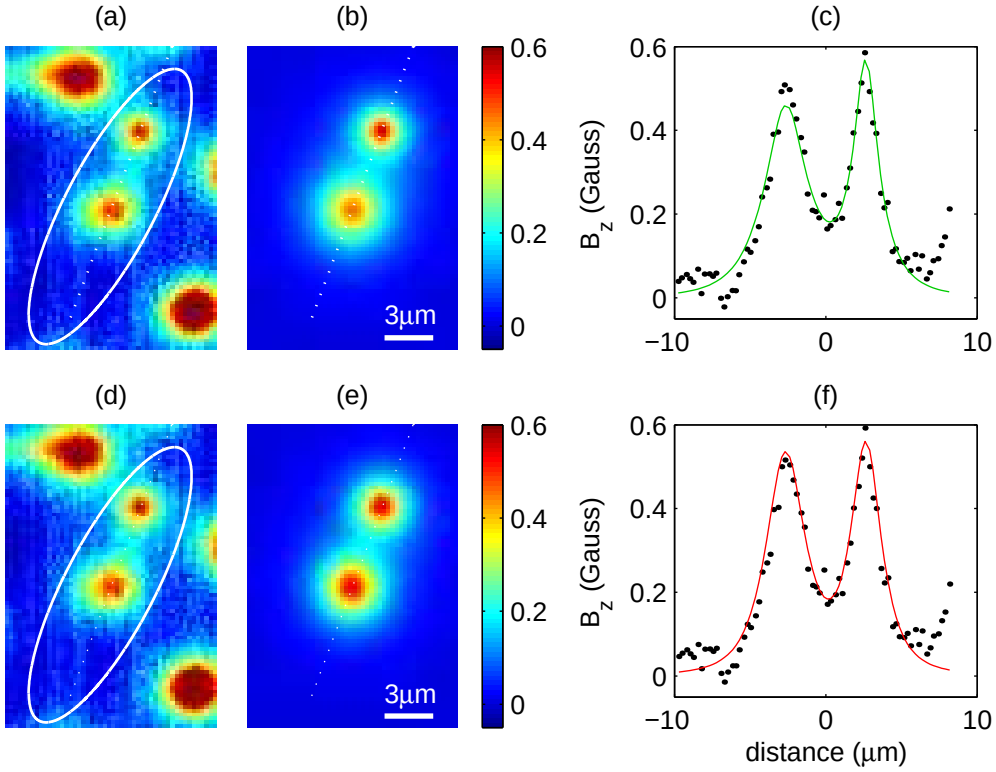

Figure 6.16: Fits of a split pancake vortex stack. (a) Image of partial vortices. The chosen color-scale saturates the larger nearby vortices in order to show the detail of the partial vortices. (b) Fit to the data in the ellipse in (a) with fixed parameters $z = 0.6$ μm and $\lambda_{ab} = 1.11$ μm, and best fit parameter $d = 0.53$ μm. Images (a) and (b) are displayed with a constant background subtracted as determined by the fit in (b). (c) Cross section along the line through the center of the partial vortices (white dotted line in the images). Points are from the data in (a) while the solid line is from the fit in (b). (d), (e) and (f) Same as for (a), (b) and (c) except the fit had fixed parameters $z = 1.0$ μm and $\lambda_{ab} = 0.64$ μm, and best fit parameter $d = 0.36$ μm.

pinning, the magnetic coupling would align the pancake vortices in a straight stack, as shown in Clem (1991). However, we know that there are pinning sites in the crystal, since at the low flux densities we study the vortices remain in the sample after the field is turned off at $T < T_c$.

From the energy calculations of Benkraouda and Clem (1996) mentioned earlier for a tilted versus a kinked structure, it seems logical that given an appropriate pinning landscape, split stack vortices would form in our crystals especially for the lowest T_c's in which the anisotropy should be largest. Thus pinning sites in the crystal are important in the formation of partial vortices. It cannot be determined from our images what the pinning sites are. They could be regions of oxygen inhomogeneity, twinning boundaries, lattice imperfections or something else. Future studies of the pinning landscape in these crystals and in other cuprates is desirable.

Above in Section 6.4.3 I showed that the model of a split pancake vortex stack fits very well to the data. The split stack (with $\geq$1 splits) is also consistent with and can explain the many properties of the partial vortices discussed earlier in Section 6.2.1. I will now review these properties in light of the split stack explanation.

Partial vortices were more prevalent for the lowest T_c values. Anisotropy increases as doping decreases, so the energy cost of the interlayer Josephson vortex in the split is smaller for lower T_c, making a split stack more favorable. It might also be that more pinning sites are present for low carrier doping. Another feature of the partial vortices was that they carried a continuous range of flux, not just small fractions of Φ_0. This makes sense with the split stack since the flux through the top surface due to a partial stack can have any value from 0 to Φ_0 depending only on the depth of the splitting as shown by Equation (6.14).[3]

Four other properties can also be explained in light of the split stack scenario. Partial vortices were observed in groups that together carried a total flux of Φ_0 within a (relatively large) experimental error. This observation agrees beautifully with the split pancake stack idea, because at each split a new partial stack begins. The sum of the flux from all the partial stacks must be Φ_0 for a group of pancake vortices

[3]Actually, the allowed splitting depths are discrete on the scale of the layer spacing $s = 11.7$ Å, but since $s \ll \lambda_{ab}$ the depth and the flux are continuous for all practical purposes.

extending through the whole thickness of the sample with one pancake vortex per layer. Partial vortices were observed to prefer certain regions of the sample, even after a room temperature anneal. This could be explained if those regions had more pinning sites (of whatever sort) that were favorable for partial vortices. It was also observed that for $T_c \sim 14$ K, where partial vortices were scarce, they could be created by cooling the sample in a predominantly in-plane applied field. This is explained nicely by the split stack model because if the flux lines are tilted during field cooling, particularly above the angle determined by the calculations of Benkraouda and Clem (1996), pancake vortices are much more likely to get pinned at an angle with respect to others in the stack. Lastly, the partial vortices were observed to be more mobile than full vortices. This makes sense due to the restoring forces on a split stack that favor a straight unsplit stack: the attractive magnetic coupling between pancakes in different layers, and the energy cost of the Josephson vortex linking the pancakes at a split (weak for large anisotropy). A full vortex straight stack does not experience these forces competing with pinning.

6.5 Summary

In this chapter I presented scanning SQUID and scanning Hall probe images of features which looked like vortices with sub-Φ_0 magnetic flux. This was surprising, since flux should be quantized in a superconductor. The samples were single crystals of very underdoped $YBa_2Cu_3O_{6+x}$. Partial vortices were seen only in samples with very low T_c and the probability of occurrence decreased with increasing T_c.

I showed that the observed partial vortices are the result of pancake vortex stacks which split at one or more depths below the sample surface. Fluxoid quantization is not violated. Modelling and fits show that a split stack does describe the data quite well, and qualitatively all the properties of the partial vortices can be explained by this model. For example the features appear in groups, can be formed by cooling in a horizontal applied field, and are more mobile than full vortices. Split stacks of pancake vortices can only occur in quasi-2D superconductors with large anisotropy because the Josephson coupling between the superconducting layers must be small. It

is not clear from these data if the large anisotropy alone is enough favor the split stack, or if the observation of these features depends on inhomogeneities in the sample. To our knowledge, these are the first observations of naturally occurring prevalent split pancake vortices.

Chapter 7

Conclusions

For this dissertation, I successfully implemented a cryogenic to room temperature scanning magnetic microscope in an Oxford Instruments SXM system. I used both Hall probes and Superconducting QUantum Interference Devices (SQUIDs) as the scanning magnetic sensor, though my focus was on scanning Hall probe microscopy (SHPM) due to its better spatial resolution and broad operating temperature range. The microscope had a specially made piezoelectric scanner in an "S-bender" design (Siegel et al. 1995) which allowed areas as large as 60×60 μm^2 to be imaged at 4 K. I measured the lowest resonant frequency of this large area scanner to be $\sim$40 Hz (at room temperature) which is safely above the scan frequency chosen to optimize the Hall probe imaging ($\lesssim$1 Hz). Along with the SXM, we also purchased scanning electronics and software from Oxford, though I ended up implementing my own separate data acquisition scheme with my own MABLAB® code to circumvent some grounding issues when the Hall probe was hooked up to the original hardware.

I spent part of my time fabricating and studying noise characteristics of submicron scanning Hall probes. Hall probes are appealing magnetic sensors for scanning microscopy because they have good sensitivity to magnetic field and flux, can be fabricated down to at least the 100 nm length scale for submicron – and ultimately nanoscale – spatial resolution, operate over a wide temperature and field range, and their output is directly related to the magnetic field in the active area which makes SHPM images relatively easy to interpret. Currently the best known materials for scanning Hall probes at low temperature are GaAs/AlGaAs heterostructures which

have a two-dimensional electron gas (2DEG) below the surface. The GaAs/AlGaAs 2DEG can be made with very low carrier densities and very high mobilities, making it a good material for low noise Hall probes. I fabricated Hall probes from a GaAs/AlGaAs structure with a 140 nm deep 2DEG (grown by David Kisker at IBM), with probe dimensions from 0.5 μm to 2 μm. I included an extra process step to put a thin metal gate over the active area to screen out electric fields from stray charges which had previously been disturbing our magnetic imaging. The grounded gate proved to be very helpful in improving the image quality.

The dominant noise in the smaller Hall probes was telegraph noise from one or more "switching" states, which may be due to motion of remote dopants or impurities. Higher spatial resolution Hall probes are desirable for imaging many magnetic systems, but if better spatial resolution comes with a loss of sensitivity, a compromise would need to be made. We wanted to see how the sensitivity of a Hall probe scaled with probe size, so we studied probes ranging in size from 130 nm to 10 μm, from my fabricated probes and a later generation of probes made by Clifford Hicks on a 2DEG structure grown by Hadas Shtrikman. Frequency spectra of the noise density in these probes showed that field sensitivity worsened as probe size got smaller, but the flux sensitivity improved with decreasing Hall probe size. For imaging small magnetic features, flux sensitivity is the more relevant concern, so these studies showed that probes down to the 100 nm scale can be made without sacrificing sensitivity. Our best demonstrated flux sensitivity was for the 130 nm probe which had 16 $\mu\Phi_0/\sqrt{\text{Hz}}$ for >1 kHz and 1 m$\Phi_0/\sqrt{\text{Hz}}$ for 0.1 Hz. The high frequency flux noise density is only a factor of 10 larger than the flux sensitivity of scanning SQUIDs, and arises mainly from the white noise of the room temperature preamplifier. The low frequency noise is dominated by resistive noise which shows up as telegraph noise in the time domain.

I primarily used the SHPM to image magnetic vortices in superconductors, in particular c-axis vortices in very underdoped crystals of $YBa_2Cu_3O_{6+x}$. Observable vortex properties, such as flux quantization and the extent of the vortex magnetic field (determined by the penetration depth of the superconductor), give information on the superconducting properties. This is especially useful in the cuprate superconductors where the mechanism of superconductivity is not yet understood. The very

underdoped regime is of particular importance because the superfluid density is very low and strong theoretical predictions have been made.

The vortex imaging experiments in this dissertation were made possible in part by the recent developments in $YBa_2Cu_3O_{6+x}$ (YBCO) crystal growth and preparation (Liang et al. 1998, 2002) extending to the very underdoped region with $x \approx 0.35$ and T_c in the range 4–20 K. After growth and a high temperature anneal, the degree of oxygen ordering in the CuO chains increases with room temperature annealing, taking the crystal from non-superconducting up to a saturation T_c after several weeks at room temperature. This T_c change with room temperature annealing was exploited in Chapters 5 and 6 of this dissertation to study vortex properties for a range of T_c values (5–15 K) on the *same* sample. The very underdoped samples can have narrow transition widths (typically $\Delta T_c < 2$ K) as measured with magnetic susceptibility, which can be interpreted to mean the samples are highly homogeneous. However, my images at the lowest T_c values ($\lesssim 10$ K) show inhomogeneity of the vortex field profiles which may imply doping inhomogeneities for these lowest T_c samples.

My first magnetic imaging experiments in the very underdoped YBCO were done to test a scenario of spin-charge separation (SCS) proposed as the mechanism for cuprate superconductivity. In SCS, the electron fractionalizes into a spin-1/2, charge zero, *spinon* and a spin-0, charge e, *chargon*. The chargons could, in principle, condense directly to the superconducting state without needing to form Cooper pairs. Senthil and Fisher (2000) formulated a microscopic SCS theory for the cuprates which included an excitation – or topological defect in a Z_2 gauge field – called a *vison*. We tested this promising theory for cuprate superconductivity by looking for experimental signatures of the vison. The Senthil-Fisher scenario allows flux to be quantized as $hc/2e$ because any $hc/2e$ vortices would be accompanied by a vison which provides the additional π phase winding required to keep the superconducting wave function of the chargon condensate single-valued. For very low T_c, it is predicted that hc/e vortices would be energetically preferred (Senthil and Fisher 2001a). With the scanning microscope we imaged vortices in four crystals of very underdoped YBCO, but never saw hc/e vortices. This set an upper bound on the vison energy of $E_{\rm vison}/k_B < 60$ K, which is much below the predicted energy $E_{\rm vison} \approx k_B T^*$ (Senthil and Fisher 2001a).

We also performed a more stringent test for visons by looking for a "vortex memory" effect in small rings fabricated from the YBCO crystals. In this experiment an odd or even number of $hc/2e$ flux quanta are trapped in the hole of the ring. If the temperature of the ring is warmed in zero field just above T_c, the flux will escape, but if the original state of the ring contained an odd number of flux quanta, a vison will be in the hole. If the sample is recooled below T_c before the vison can escape, an $hc/2e$ flux quantum of either sign must appear in the hole. We performed the vortex memory experiment on four samples and never saw signatures of the vison. This experiment addressed the dynamical properties of the vison and set an upper bound of $E_{\rm vison}/k_B < 190\ K \ll T^*$. Together these experiments rule out scenarios of SCS in the cuprates which require visons.

In another set of experiments, I attempted to measure the in-plane penetration depth in a very underdoped $YBa_2Cu_3O_{6.375}$ crystal as a function of T_c (which increased with room temperature annealing). The extent of the vortex flux in the bulk of the superconductor is given by λ_{ab} and determines the shape of the field profile imaged at the sample surface with the Hall probe. A difficulty with this method of determining the penetration depth is the uncertainty about other possible contributions to the vortex size. These very underdoped samples have large anisotropy, and thus it cannot be ruled out that the 2D pancake vortices which compose the observed 3D vortices are not pinned in a staggered fashion from layer to layer, which would increase the apparent extent s_{ab} of the vortex. By fitting the observed vortex field profiles I was able to measure s_{ab} which is an upper limit on λ_{ab}. If s_{ab} is the same as λ_{ab}, then my results give penetration depths (related to the superfluid density n_s/m^*) which are larger than predicted by the universal Uemura relation (Uemura et al. 1989) $T_c \propto \lambda(0)^{-2} \propto n_s(0)/m^*$. The Uemura relation was found for underdoped samples, but had not been tested in the extremely underdoped regime. Emery and Kivelson (1995a) explained the Uemura relation as thermal phase fluctuations destroying the superconductivity and setting T_c for underdoped samples. If my measurements are reflective of the true λ_{ab}, then modification of the theory will be needed to explain these results.

Finally, in the very low T_c YBCO crystals, I observed what appeared to be partial

vortices (i.e. flux bundles smaller than $hc/2e$). I studied the properties of these features and found they are more mobile than "full" vortices, tend to occur in groups, and their frequency of occurrence could be increased by field cooling the sample in a field with a large horizontal component. All these properties suggest that the partial vortices are the result of a full vortex that was partially displaced laterally. This can occur in highly anisotropic layered superconductors where a vortex is appropriately modelled as a stack of 2D pancake vortices (Clem 1991; Benkraouda and Clem 1996). The observed partial vortices are interpreted to be the field from partial stacks of pancake vortices displaced by some horizontal distance. My data show displacements as large as tens-of-microns. I computed the fields for a stack with one split, and fit this model to an observed pair of partial vortices with the depth of the stack splitting as a free parameter. The model fit the data quite well. A continuum of split depths and a varying total number of splits (per full vortex) were observed in the data. To my knowledge, these are the first observations of naturally occurring prevalent split pancake vortices. (A split stack was observed once by Grigorenko et al. (2002). It was created by an abrupt change in the external field, and was atypical.) The data qualitatively give information about the crystal anisotropy and pinning landscapes, though it is not yet clear what role, if any, inhomogeneities in the sample play in forming the partial vortices.

In summary, scanning Hall probe microscopy is a useful tool for studying magnetic samples. SHPM has submicron spatial resolution and the probes can be made as small as $\sim$100 nm without compromising flux sensitivity. I fabricated submicron probes and used them in a variable temperature scanning probe microscope to study vortices in newly available very underdoped $YBa_2Cu_3O_{6+x}$ single crystals. These studies refuted a promising theory for cuprate superconductivity, measured the apparent extent of the vortex field in these crystals, and revealed a prevalent phenomena of split vortices. Further studies of these and other cuprate superconductors with scanning magnetic microscopy and other techniques will hopefully help determine the elusive mechanism of high-temperature superconductivity.

Appendix A

Details of the model for vortex fitting

Fits to individual magnetic vortices in a superconductor were performed at many stages of this dissertation, most particularly for the penetration depth measurements discussed in Chapter 5. In all cases the $YBa_2Cu_3O_{6+x}$ samples had the ab-plane parallel to the surface and the imaged vortices were along the c-axis. Obviously a model is required if we want to fit the vortices. Parameters such as the in-plane penetration depth (λ_{ab}) and/or the total flux carried by the vortex (Φ, which in this Appendix will be treated as a fixed parameter $\Phi = \Phi_0$) can be obtained from fits. Here I review the model for the magnetic field profile of a vortex and give details on integrating over the Hall probe area. The fitting was done with the non-linear regression routine in Mathematica®, so the model had to be put in a differentiable form.

Take a c-axis vortex in a crystal with axial symmetry ($\lambda_a = \lambda_b$) where the sample surface is parallel to the ab and xy planes. The magnetic field profile of the vortex can be found from London's equations and Maxwell's equations (Pearl 1966; Kogan et al. 1993; Kirtley et al. 1999a). The z component of the magnetic field above an infinite plane superconductor due to a c-axis vortex is

$$B_z(\mathbf{r}, z) = \frac{\Phi_0}{(2\pi\lambda_{ab})^2} \int d^2\mathbf{q}\; e^{i\mathbf{q}\cdot\mathbf{r}} \frac{e^{-qz}}{Q[Q + q\,\coth(Qd/2)]}, \tag{A.1}$$

where d is the thickness of the superconductor, $\mathbf{r} = (x, y)$ is the radial distance from the vortex center, $\mathbf{q} = (q_x, q_y)$, $Q = \sqrt{q^2 + \lambda_{ab}^{-2}}$, and z is the distance above the

superconductor surface (Kirtley et al. 1999c).

For samples much thicker than λ_{ab}, as was the case for my samples, the equation simplifies to the thick crystal limit with $d \to \infty$ (e.g. a superconducting half-space occupying $z < 0$):

$$B_z(\mathbf{r}, z) = \frac{\Phi_0}{(2\pi\lambda_{ab})^2} \int d^2\mathbf{q}\; e^{i\mathbf{q}\cdot\mathbf{r}} \frac{e^{-qz}}{q^2 + \lambda_{ab}^{-2} + q\sqrt{q^2 + \lambda_{ab}^{-2}}}, \tag{A.2}$$

or after doing the angular integral

$$B_z(r, z) = \frac{\Phi_0}{2\pi\lambda_{ab}^2} \int_0^\infty dq \frac{q\; J_0(qr)\; e^{-qz}}{q^2 + \lambda_{ab}^{-2} + q\sqrt{q^2 + \lambda_{ab}^{-2}}}. \tag{A.3}$$

I used the thick crystal model in two cases. The first was in the limit $\sqrt{r^2 + z^2} \gg \lambda_{ab}$ where the model simplifies to that of a magnetic monopole. This simpler monopole model can be solved analytically. Outside that limit, the full model of Equation (A.3) was used, which does not have an analytical solution. In each case the model was averaged over an area representative of the Hall probe active area to account for convolution of the field over the probe. Details are given below for the monopole model (Section A.1) and the full model (Section A.2).

A.1 The monopole model

In the limit $\sqrt{r^2 + z^2} \gg \lambda_{ab}$, the vortex field profile above the thick superconductor (Equation A.3) simplifies to

$$B_z(r, z) = \frac{\Phi_0}{2\pi} \frac{z + \lambda_{ab}}{[r^2 + (z + \lambda_{ab})^2]^{3/2}}, \tag{A.4}$$

which is the equation of a monopole of strength $2\Phi_0$ located λ_{ab} below the surface. See Carneiro and Brandt (2000) for a derivation.

For fitting vortex images, it is first desirable to integrate Equation (A.4) over the Hall probe area to obtain an accurate model for a Hall probe vortex image. The

true shape of the Hall probe active area cannot be controlled due to 2DEG depletion, non-ideal current paths, and rounding of the lithographic corners. Ideally the active area would be square, but in reality it is rounded out. Therefore, either a square or a circle can be taken as a rough approximation to the active area geometry. Integration of Equation (A.4) over a square area yields an analytic result, while a circular area does not. Therefore I chose a square Hall probe area for the monopole model. In my later imaging studies (Chapters 5 and 6), the Hall probe had lithographic size $s = 0.5$ μm which was small compared to the vortex field spreading in the very underdoped $YBa_2Cu_3O_{6+x}$, and the assumed Hall probe shape and size did not affect the results significantly.

The equation of the field as seen by the Hall probe is obtained by integrating Equation (A.4) over a square active area of sides s and dividing by the area s^2:

$$B_{HP}(x,y,z) = \frac{\Phi_0}{2\pi s^2}\int_{y-\frac{s}{2}}^{y+\frac{s}{2}} dy \int_{x-\frac{s}{2}}^{x+\frac{s}{2}} dx \frac{h}{[x^2+y^2+h^2]^{3/2}}, \tag{A.5}$$

where $h = z + \lambda_{ab}$ for simplicity.

The indefinite version of the x integral above yields

$$\frac{xh}{(y^2+h^2)\sqrt{x^2+y^2+h^2}}. \tag{A.6}$$

The subsequent indefinite y integral performed with Mathematica® gives an expression of complex logarithms, which after manipulation and simplification is

$$\frac{1}{2}\arctan\left(\frac{2xyh\sqrt{x^2+y^2+h^2}}{h^2(x^2+y^2+h^2)-x^2y^2}\right). \tag{A.7}$$

However, Expression (A.7) has discontinuous jumps of magnitude $\pi/2$ when the denominator crosses zero, as shown in Figure A.1.

To fit vortex images with the non-linear regression package in Mathematica®, the model must be a differentiable function. To eliminate the $\pi/2$ jumps and make Expression (A.7) continuous, I added a differentiable step function. Define the function $\mathrm{Sign}(x) = x/\sqrt{x^2}$, which gives $+1$ when $x > 0$ and -1 when $x < 0$. Mathematica®

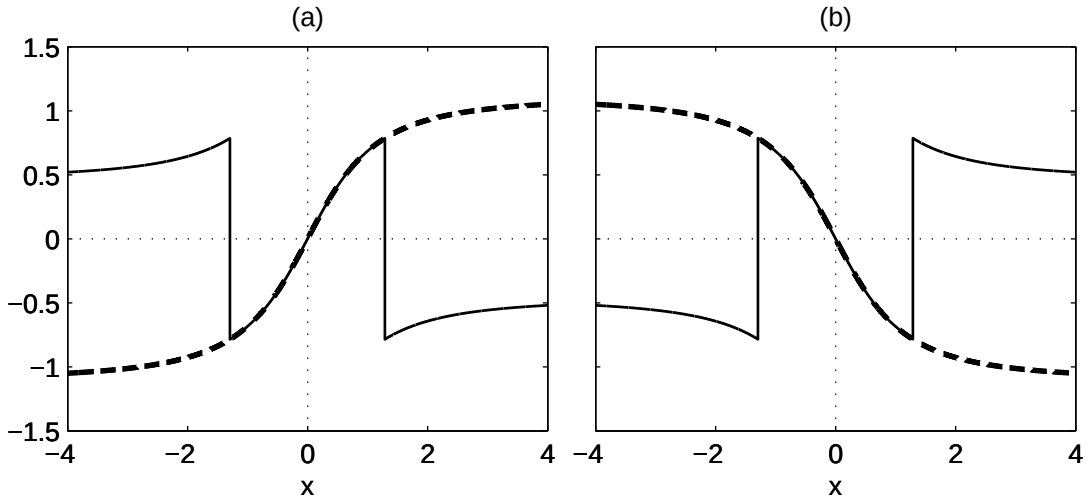

Figure A.1: Jumps in the integrated monopole model solution. Comparison of Expression (A.7) (thin solid curve) to the improved expression (thick dashed curve) which is the sum of Expressions (A.7) and (A.8). Note the $\pi/2$ jumps in the original expression. In (a) $y = 2$ and $h = 1$, in (b) $y = -2$ and $h = 1$.

does not have a problem differentiating $\mathrm{Sign}(x)$. I define the following function to add to Expression (A.7) to correct for the $\pm\pi/2$ jumps:

$$\mathrm{Fix}(x, y, h) = \frac{\pi}{2}\,\mathrm{Sign}(xy)\,\frac{1}{2}\left[1 - \mathrm{Sign}\big(h^2(x^2 + y^2 + h^2) - x^2y^2\big)\right]. \tag{A.8}$$

Thus the final differentiable fitting function for the monopole model convolved over a square Hall probe area of size s is

$$B_{HP}(x, y, z) = \frac{\Phi_0}{2\pi s^2}\left[\left[\frac{1}{2}\arctan\left(\frac{2xyh\sqrt{x^2 + y^2 + h^2}}{h^2(x^2 + y^2 + h^2) - x^2y^2}\right) + \mathrm{Fix}(x, y, h)\right]_{x-\frac{s}{2}}^{x+\frac{s}{2}}\right]_{y-\frac{s}{2}}^{y+\frac{s}{2}}. \tag{A.9}$$

Additional terms can be added to the model to include a constant or planar background. Typically I fit the vortices with free parameters $h = z + \lambda_{ab}$, the vortex center (x_0, y_0), and coefficients of a constant or sloped background. The flux, which here is $\Phi = \Phi_0$, can also be taken as a free parameter.

A.2 The full model

When the penetration depth λ_{ab} is not small compared to the distance from the vortex, the full model given in Equation (A.3) must be used. This integral cannot be solved analytically. Instead we integrate it numerically in Mathematica® and then create an interpolated function. The interpolated function can either be used directly in fitting the vortex image if the Hall probe size is small compared to the feature size, or it can first be numerically integrated over an area representing the Hall probe.[1]

Equation (A.3) for the vortex field can also be written as

$$B_z(r,z) = \frac{\Phi_0}{2\pi\lambda_{ab}^2}\int_0^\infty d\tilde{q}\frac{\tilde{q}\ J_0(\tilde{q}\tilde{r})\ e^{-\tilde{q}\tilde{z}}}{\tilde{q}^2+1+\tilde{q}\sqrt{\tilde{q}^2+1}}. \tag{A.10}$$

where $\tilde{r} = r/\lambda_{ab}$, $\tilde{z} = z/\lambda_{ab}$, and $\tilde{q} = q\lambda_{ab}$ are dimensionless. In this way the integral is now only a function of two unknowns, $\tilde{r}$ and $\tilde{z}$, since explicit reference to λ_{ab} has been eliminated. This integral was numerically integrated for a grid of 11,799 values of $(\tilde{r},\ \tilde{z})$ ranging from 0–65 for $\tilde{r}$ and 0.03–20.03 for $\tilde{z}$. Step size ranged from 0.1–1.0 for $\Delta\tilde{r}$ and from 0.1–0.5 for $\Delta\tilde{z}$, with increasing step sizes as $\tilde{r}$ and $\tilde{z}$ increased, respectively. Integrating with the full 0 to ∞ limits worked for some values of $\tilde{r}$ and $\tilde{z}$ by invoking the Mathematica® "oscillatory" method, while for other values it was necessary to truncate the integration with an upper limit of $\tilde{q} = 20/\tilde{z}$. Due to the exponential $e^{-\tilde{q}\tilde{z}}$ term in the integrand, this is completely sufficient. Finally, the 11,799 numerical integrations were converted to an interpolated function in Mathematica® which I will denote by $\mathrm{Interp}(r/\lambda_{ab}, z/\lambda_{ab})$ such that $B_z(r,z) = (\Phi_0/2\pi\lambda_{ab}^2)\,\mathrm{Interp}(r/\lambda_{ab}, z/\lambda_{ab})$. The vortex images can be fit to this B_z when convolution of the field over the Hall probe is not of concern.

For a further accurate model, I averaged $B_z(r,z)$ over the area of the Hall probe. In order to preserve the radial symmetry, a circular geometry with radius ρ was chosen for the Hall probe area. As mentioned earlier, the actual Hall probe geometry is probably between that of a square and a circle. Since the probe was small ($\rho \lesssim 0.25\ \mu$m) for

[1]The full model numerical computations and data fitting discussed here were initially implemented by Hendrik Bluhm.

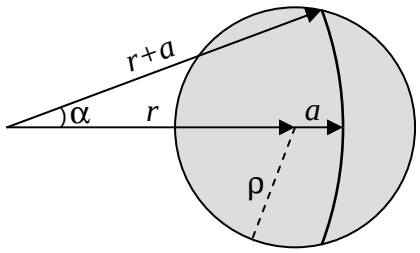

Figure A.2: Geometry for integrating over a circular Hall probe of radius ρ, centered a distance r from a vortex. See details in the text.

the imaging in which this full model was used (Chapters 5 and 6), the exact shape and size do not significantly affect the fits.

See Figure A.2 for the integration geometry. The field is integrated over the Hall probe area of radius ρ shown in gray when it is centered at a distance $r = (x, y)$ from the origin (i.e. the vortex center). Due to radial symmetry, B_z is constant along the arc shown. The arc length is $2\alpha(r + a)$, where

$$\alpha = \begin{cases} \arccos\left[1 - \frac{\rho^2 - a^2}{2r(r+a)}\right] & (a \geq \rho - 2r) \\ \pi & (a \leq \rho - 2r) \end{cases} . \tag{A.11}$$

The Hall probe signal is then

$$B_{HP}(r,z) = \frac{1}{\pi\rho^2} \int_{-\min(r,\rho)}^{\rho} da\ 2\alpha(r+a)\, B_z(r,z) \tag{A.12}$$

$$= \frac{\Phi_0}{(\pi\rho\lambda_{ab})^2} \int_{-\min(r,\rho)}^{\rho} da\ \alpha(r+a)\, \mathrm{Interp}(r/\lambda_{ab}, z/\lambda_{ab}). \tag{A.13}$$

This integration was done numerically with $\rho = 0.25$ μm and using the previously calculated $\mathrm{Interp}(r/\lambda_{ab}, z/\lambda_{ab})$ function. I calculated $B_{HP}(r,z)$ for a 3D grid of 121,440 values of $(\tilde{r} = r/\lambda_{ab}, \tilde{z} = z/\lambda_{ab}, \lambda_{ab})$. λ_{ab} ranged from 0.1–10 μm with increasing step sizes $\Delta\lambda_{ab} = 0.03$–$0.61$ μm for 32 values. $\tilde{r}$ ranged from 0–61 and $\tilde{z}$ from 0.03–18 with increasing step sizes $\Delta\tilde{r} = 0.06$–1.86 and $\Delta\tilde{z} = 0.08$–1.63 for 115 and 33 values, respectively. The real part of the numerical integral was taken, because numerical limitations of the integration sometimes gave complex results with an extremely

small imaginary component. Finally the 121,440 values were interpolated to give the function InterpHP($r/\lambda_{ab}, z/\lambda_{ab}, \lambda_{ab}$) which was specifically for $\rho = 0.25$ μm. This interpolated solution for $B_{HP}(r, z)$ was then used as the fitting model for vortex images with non-linear regression. Terms for a constant background and a planar slope (optional) were added to the model. Free parameters in the fit were λ_{ab}, the vortex center (x_0, y_0), and coefficients of a constant or sloped background. z was typically chosen prior to the fit, because z and λ_{ab} are highly correlated in the model and do not give realistic results if both are fit independently (e.g. some attempts to fit data with z and λ_{ab} independently gave unphysical $\lambda_{ab} < 0$ or $z < 0.4$ μm results).

List of References

H. Alloul, T. Ohno, and P. Mendels. ^{89}Y NMR evidence for a Fermi-liquid behavior in $YBa_2Cu_3O_{6+x}$. *Physical Review Letters* **63**, 1700–3 (1989).

P.W. Anderson. The resonating valence bond state in La_2CuO_4 and superconductivity. *Science* **235**, 1196–8 (1987).

D.N. Basov, R. Liang, D.A. Bonn, W.N. Hardy, B. Dabrowski, M. Quijada, D.B. Tanner, J.P. Rice, D.M. Ginsberg, and T. Timusk. In-plane anisotropy of the penetration depth in $YBa_2Cu_3O_{7-x}$ and $YBa_2Cu_4O_8$ superconductors. *Physical Review Letters* **74**, 598–601 (1995).

M.R. Beasley, R. Labusch, and W.W. Webb. Flux creep in type-II superconductors. *Physical Review* **181**, 682–700 (1969).

J.G. Bednorz and K.A. Müller. Possible high T_c superconductivity in the Ba-La-Cu-O system. *Zeitschrift fur Physik B* **64**, 189–93 (1986).

S.J. Bending. Local magnetic probes of superconductors. *Advances in Physics* **48**, 449–535 (1999).

S.J. Bending and A. Oral. Hall effect in a highly inhomogeneous magnetic field distribution. *Journal of Applied Physics* **81**, 3721–5 (1997).

M. Benkraouda and J.R. Clem. Instability of a tilted vortex line in magnetically coupled layered superconductors. *Physical Review B* **53**, 438–42 (1996).

J. Hendrik Bluhm. Private communication.

D.A. Bonn, S. Kamal, A. Bonakdarpour, Ruixing Liang, W.N. Hardy, C.C. Homes, D.N. Basov, and T. Timusk. Surface impedance studies of YBCO. *Czechoslovak Journal of Physics* **46**, S6, 3195–202 (1996).

D.A. Bonn, J.C. Wynn, B.W. Gardner, Yu-Ju Lin, R. Liang, W.N. Hardy, J.R. Kirtley, and K.A. Moler. A limit on spin-charge separation in high-T_c superconductors from the absence of a vortex-memory effect. *Nature* **414**, 887–9 (2001).

G. Carneiro and E.H. Brandt. Vortex lines in films: Fields and interactions. *Physical Review B* **61**, 6370–6 (2000).

A. Carrington, R.W. Giannetta, J.T. Kim, and J. Giapintzakis. Absence of nonlinear Meissner effect in $YBa_2Cu_3O_{6.95}$. *Physical Review B* **59**, R14173–6 (1999).

A.R. Champagne, A.J. Couture, F. Kuemmeth, and D.C. Ralph. Nanometer-scale scanning sensors fabricated using stencil lithography. *Applied Physics Letters* **82**, 1111–3 (2003).

A.M. Chang, H.D. Hallen, L. Harriott, H.F. Hess, H.L. Kao, J. Kwo, R.E. Miller, R. Wolfe, J. van der Ziel, and T.Y. Chang. Scanning Hall probe microscopy. *Applied Physics Letters* **61**, 1974–6 (1992).

B.K. Chong, H. Zhou, G. Mills, L. Donaldson, and J.M.R. Weaver. Scanning Hall probe microscopy on an atomic force microscope tip. *Journal of Vacuum Science & Technology A* **19**, 1769–72 (2001).

C.-H. Chung, K. Voelker, and Y.B. Kim. Statistics of spinons in the spin-liquid phase of Cs_2CuCl_4. *Physical Review B* **68**, 94412/1–4 (2003).

J.R. Clem. Two-dimensional vortices in a stack of thin superconducting films: A model for high-temperature superconducting multilayers. *Physical Review B* **43**, 7837–46 (1991).

J.R. Clem. 2D pancake vortices in a finite stack of superconducting layers. *Physica C* **235–240**, 2607–8 (1994).

R. Coldea, D.A. Tennant, A.M. Tsvelik, and Z. Tylczynski. Experimental realization of a 2D fractional quantum spin liquid. *Physical Review Letters* **86**, 1335–8 (2001).

D. Davidović, S. Kumar, D.H. Reich, J. Siegel, S.B. Field, R.C. Tiberio, R. Hey, and K. Ploog. Correlations and disorder in arrays of magnetically coupled superconducting rings. *Physical Review Letters* **76**, 815–18 (1996).

Jr. Deaver, B.S. and W.M. Fairbank. Experimental evidence for quantized flux in superconducting cylinders. *Physical Review Letters* **7**, 43–6 (1961).

G.C. DeSalvo, W.F. Tseng, and J. Comas. Etch rates and selectivities of citric acid/hydrogen peroxide on GaAs, $Al_{0.3}Ga_{0.7}As$, $In_{0.2}Ga_{0.8}As$, $In_{0.53}Ga_{0.47}As$, $In_{0.52}Al_{0.48}As$, and InP. *Journal of the Electrochemical Society* **139**, 831–5 (1992).

V.J. Emery and S.A. Kivelson. Importance of phase fluctuations in superconductors with small superfluid density. *Nature* **374**, 434–7 (1995a).

V.J. Emery and S.A. Kivelson. Superconductivity in Bad Metals. *Physical Review Letters* **74**, 3253–6 (1995b).

A.T. Fiory, A.F. Hebard, P.M. Mankiewich, and R.E. Howard. Penetration depths of high T_c films measured by two-coil mutual inductances. *Applied Physics Letters* **52**, 2165–7 (1988).

C.J.B. Ford, S. Washburn, M. Buttiker, C.M. Knoedler, and J.M. Hong. Influence of geometry on the Hall effect in ballistic wires. *Physical Review Letters* **62**, 2724–7 (1989).

M. Franz and Z. Tešanović. Flux tubes, visons, and vortices in spin-charge separated superconductors. *Physica C* **357–60**, 49–52 (2001).

T. Fukumura, H. Sugawara, K. Kitazawa, T. Hasegawa, Y. Nagamune, T. Noda, and H. Sakaki. Development of a scanning Hall probe microscope for simultaneous magnetic and topographic imaging. *Micron* **30**, 575–8 (1999).

B.W. Gardner, J.C. Wynn, P.G. Björnsson, E.W.J. Straver, K.A. Moler, J.R. Kirtley, and M.B. Ketchen. Scanning superconducting quantum interference device susceptometry. *Review of Scientific Instruments* **72**, 2361–4 (2001).

B.W. Gardner, J.C. Wynn, D.A. Bonn, Ruixing Liang, W.N. Hardy, J.R. Kirtley, V.G. Kogan, and K.A. Moler. Manipulation of single vortices in $YBa_2Cu_3O_{6.354}$ with a locally applied magnetic field. *Applied Physics Letters* **80**, 1010–2 (2002).

D. Goldhaber-Gordon, H. Shtrikman, D. Mahalu, D. Abusch-Magder, U. Meirav, and M.A. Kastner. Kondo effect in a single-electron transistor. *Nature* **391**, 156–9 (1998).

C.E. Gough, M.S. Colclough, E.M. Forgan, R.G. Jordan, M. Keene, C.M. Muirhead, A.I.M. Rae, N. Thomas, J.S. Abell, and S. Sutton. Flux quantization in a high-T_c superconductor. *Nature* **326**, 855 (1987).

A.N. Grigorenko, S.J. Bending, J.K. Gregory, and R.G. Humphreys. Scanning Hall probe microscopy of flux penetration into a superconducting $YBa_2Cu_3O_{7-\delta}$ thin film strip. *Applied Physics Letters* **78**, 1586–8 (2001).

A.N. Grigorenko, S.J. Bending, A.E. Koshelev, J.R. Clem, T. Tamegai, and S. Ooi. Visualization of interacting crossing vortex lattices in the presence of quenched disorder. *Physical Review Letters* **89**, 217003/1–4 (2002).

V. Gusiatnikov, F. Altomare, J.C. Chen, A.M. Chang, A. Lichtenberger, and J. Woodall. Nanoscale Scanning Hall Probe Microscopy. *Bulletin of the American Physical Society* **46**, 917 (2001).

E.H. Hall. On a new action of the magnet on electric currents. *American Journal of Mathematices* **2**, 287–92 (1879).

W.N. Hardy, D.A. Bonn, D.C. Morgan, Ruixing Liang, and Kuan Zhang. Precision measurements of the temperature dependence of lambda in $YBa_2Cu_3O_{6.95}$: strong evidence for nodes in the gap function. *Physical Review Letters* **70**, 3999–4002 (1993).

K. Hasselbach, C. Veauvy, and D. Mailly. MicroSQUID magnetometry and magnetic imaging. *Physica C* **332**, 140–7 (2000).

Paul Horowitz and Winfield Hill. *The Art of Electronics.* Cambridge University Press, 2nd ed. (1989).

A. Hosseini, D.M. Broun, D.E. Sheehy, T.P. Davis, M. Franz, W.N. Hardy, Ruixing Liang, and D.A. Bonn. Survival of the d-wave superconducting state near the edge of antiferromagnetism in the cuprate phase diagram. `xxx.lanl.gov` cond-mat/0312542 (2003).

H.J. Hug, A. Moser, I. Parashikov, B. Stiefel, O. Fritz, H.-J. Gintherodt, and H. Thomas. Observation and manipulation of vortices in $YBa_2Cu_3O_7$ thin film with a low temperature magnetic force microscope. *Physica C* **235-240**, 2695–6 (1994).

J.R. Kirtley. SQUID microscopy for fundamental studies. *Physica C* **368**, 55–65 (2002).

J.R. Kirtley, P. Chaudhari, M.B. Ketchen, N. Khare, Shawn-Yu Lin, and T. Shaw. Distribution of magnetic flux in high-T_c grain-boundary junctions enclosing hexagonal and triangular areas. *Physical Review B* **51**, 12057–60 (1995a).

J.R. Kirtley, M.B. Ketchen, K.G. Stawiasz, J.Z. Sun, W.J. Gallagher, S.H. Blanton, and S.J. Wind. High-resolution scanning SQUID microscope. *Applied Physics Letters* **66**, 1138–40 (1995b).

J.R. Kirtley, V.G. Kogan, J.R. Clem, and K.A. Moler. Magnetic field of an in-plane vortex outside a layered superconductor. *Physical Review B* **59**, 4343–8 (1999a).

J.R. Kirtley, C.C. Tsuei, V.G. Kogan, J.R. Clem, H. Raffy, and Z.Z. Li. Fluxoid dynamics in superconducting thin film rings. *Physical Review B* **68**, 214505/1–8 (2003).

J.R. Kirtley, C.C. Tsuei, and K.A. Moler. Temperature dependence of the half-integer magnetic flux quantum. *Science* **285**, 1373–5 (1999b).

J.R. Kirtley, C.C. Tsuei, K.A. Moler, V.G. Kogan, J.R. Clem, and A.J. Turberfield. Variable sample temperature scanning superconducting quantum interference device microscope. *Applied Physics Letters* **74**, 4011–3 (1999c).

J.R. Kirtley, C.C. Tsuei, H. Raffy, Z.Z. Li, V.G. Kogan, J.R. Clem, and K.A. Moler. Direct measurement of single fluxoid dynamics in superconducting rings. `xxx.lanl.gov` cond-mat/0103474 (2001).

J.R. Kirtley, C.C. Tsuei, M. Rupp, J.Z. Sun, L.S. Yu-Jahnes, A. Gupta, M.B. Ketchen, K.A. Moler, and M. Bhushan. Direct imaging of integer and half-integer Josephson vortices in high-T_c grain boundaries. *Physical Review Letters* **76**, 1336–9 (1996).

S.A. Kivelson. Personal communication.

S.A. Kivelson, D.S. Rokhsar, and J.P. Sethna. Topology of the resonating valence-bond state: solitons and high-T_c superconductivity. *Physical Review B* **35**, 8865–8 (1987).

S.A. Kivelson, D.S. Rokhsar, and J.P. Sethna. 2e or not 2e: flux quantization in the resonating valence bond state. *Europhysics Letters* **6**, 353–8 (1988).

V.G. Kogan. Unpublished.

V.G. Kogan, A.Yu. Simonov, and M. Ledvij. Magnetic field of vortices crossing a superconductor surface. *Physical Review B* **48**, 392–7 (1993).

L. Krusin-Elbaum, R.L. Greene, F. Holtzberg, A.P. Malozemoff, and Y. Yeshurun. Direct measurement of the temperature-dependent magnetic penetration depth in Y-Ba-Cu-O crystals. *Physical Review Letters* **62**, 217–20 (1989).

C. Kurdak, C.-J. Chen, D.C. Tsui, S. Parihar, S. Lyon, and G.W. Weimann. Resistance fluctuations in GaAs/Al_xGa_{1-x}As quantum point contact and Hall bar structures. *Physical Review B* **56**, 9813–8 (1997).

Ju Young Lee, K.M. Paget, T.R. Lemberger, S.R. Foltyn, and Xindi Wu. Crossover in temperature dependence of penetration depth lambda (T) in superconducting $YBa_2Cu_3O_{7-\delta}$. *Physical Review B* **50**, 3337–41 (1994).

R. Liang, D.A. Bonn, and W.N. Hardy. Growth of high quality YBCO single crystals using $BaZrO_3$ crucibles. *Physica C* **304**, 105–11 (1998).

R. Liang, D.A. Bonn, W.N. Hardy, J.C. Wynn, K.A. Moler, L. Lu, S. Larochelle, L. Zhou, M. Greven, L. Lurio, and S.G.J. Mochrie. Preparation and characterization of homogeneous YBCO single crystals with doping level near the SC-AFM boundary. *Physica C* **383**, 1–7 (2002).

C. Lin and C.P. Lee. Comparison of Au/Ni/Ge Au/Pd/Ge and Au/Pt/Ge Ohmic contacts to n-type GaAs. *Journal of Applied Physics* **67**, 260–3 (1990).

J. Mannhart, H. Hilgenkamp, B. Mayer, C. Gerber, J.R. Kirtley, K.A. Moler, and M. Sigrist. Generation of magnetic flux by single grain boundaries of $YBa_2Cu_3O_{7-x}$. *Physical Review Letters* **77**, 2782–5 (1996).

R.G. Mints, V.G. Kogan, and J.R. Clem. Vortices in magnetically coupled superconducting layered systems. *Physical Review B* **61**, 1623–9 (2000).

R.G. Mints, I. Papiashvili, J.R. Kirtley, H. Hilgenkamp, G. Hammerl, and J. Mannhart. Observation of splintered Josephson vortices at grain boundaries in $YBa_2Cu_3O_{7-\delta}$. *Physical Review Letters* **89**, 067004/1–4 (2002).

R. Moessner, S.L. Sondhi, and E. Fradkin. Short-ranged resonating valence bond physics quantum dimer models and Ising gauge theories. *Physical Review B* **65**, 024504/1–16 (2002).

N. Nagaosa. e vs. 2e quantization in the spin gap phase of high-T_c superconductors. *Journal of the Physical Society of Japan* **63**, 2835–6 (1994).

N. Nagaosa and P.A. Lee. Ginzburg-Landau theory of the spin-charge-separated system. *Physical Review B* **45**, 966–70 (1992).

Zaira Nazario and David I. Santiago. Personal communication.

A. Oral, J.C. Barnard, S.J. Bending, I.I. Kaya, S. Ooi, T. Tamegai, and M. Henini. Direct observation of melting of the vortex solid in $Bi_2Sr_2CaCu_2O_{8+\delta}$ single crystals. *Physical Review Letters* **80**, 3610–3 (1998).

A. Oral, S.J. Bending, and M. Henini. Real-time scanning Hall probe microscopy. *Applied Physics Letters* **69**, 1324–6 (1996a).

A. Oral, S.J. Bending, and M. Henini. Scanning Hall probe microscopy of superconductors and magnetic materials. *Journal of Vacuum Science & Technology B* **14**, 1202–5 (1996b).

A. Oral, A. Kaval, M. Dede, H. Masuda, A. Okamoto, I. Shibasaki, and A. Sandhu. Room-temperature scanning Hall probe microscope (RT-SHPM) imaging of garnet films using new high-performance InSb sensors. *IEEE Transactions on Magnetics* **38**, 2438–40 (2002).

A. Paramekanti, L. Balents, and M.P.A. Fisher. Ring exchange, the exciton Bose liquid, and bosonization in two dimensions. *Physical Review B* **66**, 054526/1–27 (2002).

A. Paramekanti, M. Randeria, and N. Trivedi. Fractionalization in spin liquid Mott insulators: vison wavefunctions and gaps. `xxx.lanl.gov` cond-mat/0303360 (2003).

J. Pearl. Structure of superconductive vortices near a metal-air interface. *Journal of Applied Physics* **37**, 4139–41 (1966).

F.M. Peeters and X.Q. Li. Hall magnetometer in the ballistic regime. *Applied Physics Letters* **72**, 572–4 (1998).

T. Pereg-Barnea, P.J. Turner, R. Harris, G.K. Mullins, J.S. Bobowski, M. Raudsepp, Ruixing Liang, D.A. Bonn, and W.N. Hardy. Absolute values of the London penetration depth in $YBa_2Cu_3O_{6+y}$ measured by zero field ESR spectroscopy on Gd doped single crystals. `xxx.lanl.gov` cond-mat/0311555 (2003).

G.N. Phillips, M. Siekman, L. Abelmann, and J.C. Lodder. High resolution magnetic force microscopy using focused ion beam modified tips. *Applied Physics Letters* **81**, 865–7 (2002).

T.C. Ribeiro and X.-G. Wen. Possible Z_2 phase and spin-charge separation in electron-doped cuprate superconductors. *Physical Review B* **68**, 24501/1–6 (2003).

S. Sachdev. Stable hc/e vortices in a gauge theory of superconductivity in strongly correlated systems. *Physical Review B* **45**, 389–99 (1992).

A. Sandhu, H. Masuda, K. Kurosawa, A. Oral, and S.J. Bending. Bismuth nano-Hall probes fabricated by focused ion beam milling for direct magnetic imaging by room temperature scanning Hall probe microscopy. *Electronics Letters* **37**, 1335–6 (2001a).

A. Sandhu, H. Masuda, A. Oral, and S.J. Bending. Room temperature magnetic imaging of magnetic storage media and garnet epilayers in the presence of external magnetic fields using a sub-micron GaAs SHPM. *Journal of Crystal Growth* **227–228**, 899–905 (2001b).

R.D. Sedgewick, D.J. Scalapino, and R.L. Sugar. Fractionalized phase in an XY-Z_2 gauge model. *Physical Review B* **65**, 054508/1–6 (2002).

Karlheinz Seeger. *Semiconductor Physics: An Introduction.* Springer (New York), 6th ed. (1997).

T. Senthil and M.P.A. Fisher. Quantum confinement transition and cuprate criticality. `xxx.lanl.gov` cond-mat/9912380 (1999).

T. Senthil and M.P.A. Fisher. Z_2 gauge theory of electron fractionalization in strongly correlated systems. *Physical Review B* **62**, 7850–81 (2000).

T. Senthil and M.P.A. Fisher. Detecting fractions of electrons in the high-T_c cuprates. *Physical Review B* **64**, 214511/1–6 (2001a).

T. Senthil and M.P.A. Fisher. Fractionalization in the cuprates: detecting the topological order. *Physical Review Letters* **86**, 292–5 (2001b).

T. Senthil and O. Motrunich. Microscopic models for fractionalized phases in strongly correlated systems. *Physical Review B* **66**, 205104/1–9 (2002).

J. Siegel, J. Witt, N. Venturi, and S. Field. Compact large-range cryogenic scanner. *Review of Scientific Instruments* **66**, 2520–3 (1995).

G.D. Skidmore and E.D. Dahlberg. Improved spatial resolution in magnetic force microscopy. *Applied Physics Letters* **71**, 3293–5 (1997).

J.E. Sonier, J.H. Brewer, and R.F. Kiefl. μSR studies of the vortex state in type-II superconductors. *Reviews of Modern Physics* **72**, 769–811 (2000).

J.E. Sonier, J.H. Brewer, R.F. Kiefl, D.A. Bonn, S.R. Dunsiger, W.N. Hardy, Ruixing Liang, W.A. MacFarlane, R.I. Miller, T.M. Riseman, D.R. Noakes, C.E. Stronach, and Jr White, M.F. Measurement of the fundamental length scales in the vortex state of $YBa_2Cu_3O_{6.60}$. *Physical Review Letters* **79**, 2875–8 (1997).

K.G. Stawiasz, M.B. Ketchen, and L.R. Narasimhan. White noise performance of integrated DC SQUID susceptometers in high magnetic fields. *IEEE Transactions on Applied Superconductivity* **5**, 3230–2 (1995).

V.V. Talanov, L.V. Mercaldo, S.M. Anlage, and J.H. Claassen. Measurement of the absolute penetration depth and surface resistance of superconductors and normal metals with the variable spacing parallel plate resonator. *Review of Scientific Instruments* **71**, 2136–46 (2000).

J.L. Tallon and J.W. Loram. The doping dependence of T^* – what is the real high-T_c phase diagram?. *Physica C* **349**, 53–68 (2001).

J.L. Tallon, J.W. Loram, J.R. Cooper, C. Panagopoulos, and C. Bernhard. Superfluid density in cuprate high-T_c superconductors: a new paradigm. *Physical Review B* **68**, 180501/1–4 (2003).

A. Thiaville, L. Belliard, D. Majer, E. Zeldov, and J. Miltat. Measurement of the stray field emanating from magnetic force microscope tips by Hall effect microsensors. *Journal of Applied Physics* **82**, 3182–91 (1997).

Michael Tinkham. *Introduction to Superconductivity.* McGraw Hill (New York), 2nd ed. (1996).

Y.J. Uemura, L.P. Le, G.M. Luke, B.J. Sternlieb, W.D. Wu, J.H. Brewer, T.M. Riseman, C.L. Seaman, M.B. Maple, M. Ishikawa, D.G. Hinks, J.D. Jorgensen, G. Saito, and H. Yamochi. Basic similarities among cuprate bismuthate organic Chevrel-phase and heavy-fermion superconductors shown by penetration-depth measurements. *Physical Review Letters* **66**, 2665–8 (1991).

Y.J. Uemura, G.M. Luke, B.J. Sternlieb, J.H. Brewer, J.F. Carolan, W.N. Hardy, R. Kadono, J.R. Kempton, R.F. Kiefl, S.R. Kreitzman, P. Mulhern, T.M. Riseman, D.L. Williams, B.X. Yang, S. Uchida, H. Takagi, J. Gopalakrishnan, A.W. Sleight, M.A. Subramanian, C.L. Chien, M.Z. Cieplak, Gang Xiao, V.Y. Lee, B.W. Statt, C.E. Stronach, W.J. Kossler, and X.H. Yu. Universal correlations between T_c and n_s/m^* (carrier density over effective mass) in high-T_c cuprate superconductors. *Physical Review Letters* **62**, 2317–20 (1989).

B.W. Veal, H. You, A.P. Paulikas, H. Shi, Y. Fang, and J.W. Downey. Time-dependent superconducting behavior of oxygen-deficient $YBa_2Cu_3O_x$: possible annealing of oxygen vacancies at 300 K. *Physical Review B* **42**, 4770–3 (1990).

L.N. Vu, M.S. Wistrom, and D.J. Van Harlingen. Imaging of magnetic vortices in superconducting networks and clusters by scanning SQUID microscopy. *Applied Physics Letters* **63**, 1693–5 (1993).

F.C. Wellstood, Y. Gim, A. Amar, R.C. Black, and A. Mathai. Magnetic microscopy using SQUIDs. *IEEE Transactions on Applied Superconductivity* **7**, 3134–8 (1997).

Ralph Williams. *Modern GaAs Processing Methods.* Artech House (Boston), 1st ed. (1990).

J.C. Wynn, D.A. Bonn, B.W. Gardner, Yu-Ju Lin, Ruixing Liang, W.N. Hardy, J.R. Kirtley, and K.A. Moler. Limits on spin-charge separation from h/2e fluxoids in very underdoped $YBa_2Cu_3O_{6+x}$. *Physical Review Letters* **87**, 197002/1–4 (2001).